Università degli Studi di Ferrara

DOTTORATO DI RICERCA IN
FISICA

CICLO XXII

COORDINATORE Prof. Filippo Frontera

Satellite analysis of cloud characteristics at different temporal and spatial scales using visible and infrared wavelengths

Settore Scientifico Disciplinare FIS/06

Dottorando
Dott. Roberto Nicoletta

Tutore
Prof. Porcù Federico

Anni 2007/2009

Alla mia famiglia

Contents

Introduction

Clouds play a key role in determining the status of the atmosphere and the whole earth system over a wide range of spatial and temporal scales. The results of the Intergovernmental Panel on Climate Change (IPCC) fourth Assessment Report (2007) highlight the dominant role of water in several aspects of the Earth's climate system. Understanding the full hydrological cycle, where clouds play a relevant role, is one of the highest scientific priorities to assess, monitor and predict climate change. Furthermore, clouds interact with radiation, acting as regulators of several cooling and warming mechanisms. The effects of this complex cloud role on climate change remains a dominant uncertainty, although now clouds are better understood than at the time of the third assessment report (2001) due to improved in-situ, satellite and ground-based measurements and more comprehensive modelling.

Moreover, the everyday human activities are affected by clouds which directly impact the weather conditions and are responsible for a large number of locally significant phenomena such as precipitation (solid and liquid), lightning, strong winds, low visibility among others.

Although there has been a strong progress in physical contents of numerical models at all scales (from local area to climatological), the description of cloud processes remain a dominant source of uncertainty, because of the large variety of physical and chemical mechanisms involved in cloud formation and and interactions with radiation.

A large numbers of sources of cloud measurements are available in order to study the different cloud properties. Ground-based measurements of cloud cover have been traditionally made from visual observation for over hundred years, and a classification based on cloud height and shape has been introduced, while in the last decades instrumental measurements support or sometimes replace human observation.

Cloud structure and microphysical properties have been mainly studied by meteorological radar (ground-based or air-borne) since the early '70s. Radar is able to probe the cloud structure with spatial and temporal resolution suitable for detailed observation of most relevant cloud processes.

The turning point in cloud studies has been reached after the launch of the meteorological satellites which sensors since the early '60s have provided a further observational tool for cloud studies from the space point of view. Passive sensor over broad wavelength spectrum (from visible to microwave) are used to retrieve cloud characteristics from space, regardless if other instruments at the ground are available. Several climatology studies have taken advantages from satellites data since '80s, and the International Satellite Cloud Climatology Project (ISSCP) is completely devoted to collect, filter, correct and disseminate data from the main worldwide available sensors since 1983, also producing useful cloud products at global scale. More recently, the improvements of sensor multispectral capabilities have been used to estimate different cloud microphysical properties from geostationary orbit, allowing the continuous monitoring of the temporal and spatial variability of the cloud system properties.

The aim of this work is analysing clouds characteristics using satellite data at different scales (from meteorological to climatological one) presenting new retrieval algorithms and methodologies of analysis to contribute to cloud studies in European and Mediterranean areas. In order to analyse cloud systems at different scale cloud parameters such as cloud cover, cloud optical thickness and cloud top temperature are considered at high and low temporal and spatial resolution.

The high resolution (i.e. 3x3km^2 and 15 minutes) cloud parameters (including cloud particles effective radius) are estimated from Spinning Enhanced Visible and Infrared Imager (SEVIRI) data while clouds parameters at low resolution (i.e. 30x30km^2 and 3 hours) are extracted from the ISCCP database. Two retrieval algorithms are proposed to estimate high resolution parameter using SEVIRI data from visible to infrared spectral bands. One is a temporal statistical cloud mask algorithm that takes advantage from the high temporal resolution of the instrument. A dynamical statistical threshold applied on the brightness temperature difference (between two successive images) at 10.8 μm discriminates the cloudy from clear pixels. This cloud mask is tested comparing to the MODerate resolution Imaging Spectroradiometer (MODIS) operational product. The other algorithm uses a bispectral (visible and near infrared bands) retrieval scheme to estimate cloud optical thickness and cloud particles effective radius matching the SEVIRI reflectances with a series of look-up tables obtained by radiative transfer simulations. One application of these high resolution cloud parameters are the analysis of the temporal development of convective systems.

The cloud cover, cloud optical thickness and cloud top temperature at low resolution are analysed to describe the main characteristics of the cloud shields associated to Cut-off Low (COL) systems which play a crucial role in driving the meteorological conditions over the whole Mediterranean and European areas. Ten years of data from ISCCP and ERA-40 (by European Centre of Medium-range Weather Forecast re-analysis) databases are considered respectively to detect COL events in Mediterranean and European areas and to analyse cloud products. Finally, the influence of the climatology index North Atlantic Oscillation (NAO) on COL systems and their cloud cover associated to is shown.

The present work is structured as follows. Chapter 1 highlights the relevance of clouds in climate and in meteorological forecasts, and presents the principal performances of the instruments available for clouds measurements. Chapter 2 deals with the signatures that atmospheric constituents leaves on radiation at visible and infrared wavelengths. Chapter 3 and 4 present the algorithms to retrieve high resolution parameters and some applications: the cloud mask (Chapter 3), the optical and effective radius (chapter 4). In chapter 5 the main characteristics of the clouds pattern associated to COLs are described using cloud parameters at low resolution. The conclusions and the perspectives of my work are drawn in last chapter.

Chapter 1

Clouds in climatology and meteorology

The aim of this chapter is to outline the role of clouds in the earth system, and to introduce the main operational tools available for cloud studies from both meteorological and climatological point of view. The climate is strongly influenced by cloud processes, in fact they are the most important regulator of the radiation budget of the earth-atmosphere systems. Clouds are important in meteorology because of their link to precipitation and because of synoptic structure can be tracked observing clouds motion. Cloud studies are carried on at different scales in order to achieve different goals: at the climatological scale we are primarily interested in knowing the global coverage and distribution of clouds, on the other hand at the meteorological scale the fine structure and the processes involved in cloud lifetime (formation, development and dissipation) are the principal topics.

Several kind of data are available in order to study clouds: ground-based observations by human observers and automatic systems, ground-based radar measurements, and satellite observations. These data give the chance of studying clouds from different point of view and retrieving several characteristics at different level.

Several studies and project are devoted to cloud analysis, above all the International Satellite Cloud Climatology Project (ISCCP) and CloudSat the first satellite mission dedicated to clouds.

1.1 The role of clouds

One of the most stunning features of the images of earth from space are the clouds that move around our planet in quasi-organized large-scale systems (Rossow and Cairns, 1995). The characteristic and movement of these coherent cloud features are primarily governed by the large-scale atmospheric circulation and, as such, are an essential manifestation of weather systems. Motions of synoptic-scale cloud masses, in turn, trace the circulation patterns of the atmosphere. By tracking movements of individual cloud elements we can also estimate the wind fields (Menzel, 2001).

These large cloud systems are not mere passive tracers of wide-scale movement of air. They exert an enormous influence on our weather and climate. Two main roles of clouds are:

- they are a fundamental stage of the cycle of water in the atmosphere: condensing water vapour and forming precipitation;
- they affect the radiative budget of the planet.

By modulating the distribution of heating within the atmosphere and on the surface, clouds influence the circulations of the atmosphere and oceans. The importance of clouds to the resultant redistribution of heating is highlight in the study of Gleckler and Coauthors (1995). They showed how poorly resolved clouds, through their effects on the surface radiation budget produce a discrepancy in the implied oceanic transport of heat poleward as simulated by a large number of climate models.

In this section the roles of clouds in the radiative budget are described and quantified using the results of Earth Radiation Budget Experiment (ERBE). The description of clouds in meteorological and climatological models are also reported.

1.1.1 Clouds in the earth radiative balance

The concept of cloud radiative forcing has been used extensively to study the impact of clouds on climate (Hartmann, 1994). The net cloud radiative forcing (CRF) at the top of the atmosphere is the sum of two contributions: cloud radiative forcing at short wave (CRFSW) and cloud radiative forcing at long wave (CRFLW), and it is defined as the difference between the radiative fluxes with and without clouds, in formulas:

$$CRF = CRFSW + CRFLW;$$

where

$$CRFLW = CRFLW_{cloudy} - CRFLW_{clear};$$
$$CRFSW = S(\alpha_{clear} - \alpha);$$

where S is the monthly incoming solar flux at the top of the atmosphere and α is the total sky albedo of the earth-atmosphere system. Here α_{clear} is the clear-sky albedo of the earth atmosphere system. CRFSW is usually negative.

Two roles of clouds in radiative budget are identified:

- *cooling effect* : the radiation at short wave is reflected by clouds therefore a part of it (depending on the cloud type) does not reach the atmosphere level below the cloud and the surface;
- *heating effect* : the long wave radiation emitted by earth is absorbed and re-emitted (a portion of the energy to outer space and a fraction

back toward the surface) by clouds, therefore clouds contribute to increase the greenhouse effect.

The observations from the ERBE provided the first accurate estimate of the modulation of longwave and shortwave radiative fluxes at the top of the atmosphere by clouds (Ramanathan et al., 1989). Using the ERBE data, Harrison et al. (1990) have examined the seasonal variation of cloud radiative forcing: clouds significantly reduce the seasonal changes in the net radiative heating of the planet. This reduction is particularly strong over the mid- and high-latitude oceans, where they reduce the summer and spring solar heating by as much as $100 - 150\,Wm^{-2}$. A number of studies (Ramanathan et al., 1989; Harrison et al., 1990;Stephens and Greenwald, 1991; Hartmann and Doelling, 1991) have estimated that the global average SWCRF and LWCRF are approximately -50 Wm^{-2} and 30 Wm^{-2}, respectively. The magnitude of the net cloud radiative forcing, is generally larger in higher latitudes of the summer hemisphere. Hartmann and Doelling, 1991 examined the net radiative effectiveness of clouds in terms of a cloud factor angle defined in coordinates of reflected solar radiation versus outgoing longwave radiation (OLR). Their study suggested that ratio of the solar to the longwave effect of cloud is about 1.85 based on the regression method and 1.55 based on the comparison of clear sky and total sky fluxes.

The effect of cloud type on Earth's Energy considering a global average is investigate in different works (Hartmann and Doelling, 1991; Chen et al., 1999). The main results are: *low clouds* make the largest contribution to the net energy balance of the earth, because they cover such a large area and because their albedo effect dominates their effect on emitted thermal radiation. *High, optically thick* clouds can also give a negative contribution to the energy balance, because their very high albedo overcome their low emission temperature.

Bony et al. (1997) examined the influence of sea surface temperature and large-scale circulation on cloud radiative forcing using National Centres for Environmental Prediction-National Centre for Atmospheric Research (NCEP-NCAR) 40 yr reanalysis and ERBE datasets.

1.1.2 Clouds in climatology models

An accurate global cloud climatology is essential to develop physically based climate models: it can serve both as a source of input data and as mean of validation.

In the field of global climatology a cloudiness map covering all the globe is required to improve the understanding of the variations in the global radiative and hydrological budget. The spatial resolution in this case can be of the order of 100 km, with 10 vertical levels not equally spaced in height and pressure. In contrast, regional climatological studies need cloudiness maps with smaller spatial coverage, but with higher spatial resolution, say up to 25 km Hartmann (1994). At least three important effect in a climate model are

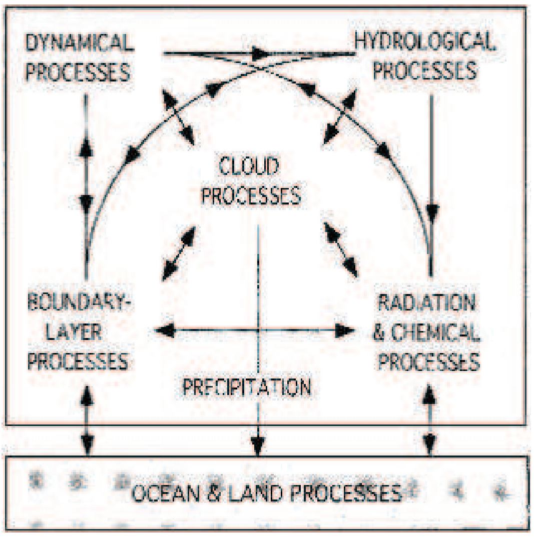

Figure 1.1: Interactions between various processes in the climate system.

associated with the formation of clouds: (1) the condensation of water vapour and the associated release of latent heat and rain; (2) vertical transport of heat, moisture, and momentum by the motions associated with the cloud; (3) the interaction of the cloud particles with radiation (Arakawa, 1975). A cloud parametrization in a climate model should treat each of these effects consistently, but this has not been the case with every climate model. Most climate models include at least two types of clouds; convective clouds and large-scale supersaturation clouds. The main cloud processes that interact with the climate systems are summarized in figure 1.1.

Among convective clouds, cumulus convection are one of the most important type of clouds considered in climatology model, because they play a central role in most of the interaction shown in figure 1.1, thus Arakawa (2004) dedicated a review to them. He made a review on the cumulus parametrization in which the major problems existing at present, and possible approaches for future climate models are described. Cloud-resolving convective parametrization or superparameterization is a promising new approach that can develop into a Multiscale Modelling Framework (MMF). It is emphasized that the use of such a framework can unify our currently diversified modelling efforts and make verification of climate models against observations much more constructive than it is now. For instance the many individual cumulus clouds which occur in a large-scale atmospheric disturbance have a time and space scales much smaller than the disturbance itself. Because of this scale separation, it may be possible to predict the time change of the large-scale disturbance by describing not each of the may individual clouds, but only their collective influence.

1.1.3 Clouds in meteorological models

The meteorological models need cloud information in order to improve cloud parametrization (through the knowledge of cloud processes) and to provide good description of the initial state (collecting data from different resources).

The representation of clouds in numerical weather prediction models remains very difficult, because of the necessity of incorporating processes with different scales. For instance, if we considers mesoscale models with continental coverage and horizontal spatial resolution of few kilometres, we have to solve complex problems of cloud microphysics. In general the parametrization of cloud processes must be kept very simple, since the numerical integrations must be carried out in a reasonable time. The parametrization of non convective clouds in weather prediction models has been applied in a much more straightforward manner, in particular two simple parametrization schemes are used in numerical models. In the first scheme, only condensation of water vapour is considered while clouds are not parametrized. In the second scheme, the cloud water is predicted and the release of precipitation is parametrized in a simple way (Sundquist, 1977). These two schemes do not considers convective clouds, although convective processes are fundamental at mesoscale resolution. In these classical method of parametrization of cloudiness the major limitation is the lack of a representation of the mesoscale organization of precipitation systems.

The increase in resolution of NWP has made even more complicate the problem of the parametrization of cloudiness (Straniforth and Mailhot, 1988). For instance, the current mesoscale models employed for routine regional forecasting use a combination of the convective and the stratiform condensation schemes (Straniforth and Mailhot, 1988). It is evident that the flow resolved on the mesh of these models does not represent the movement of air on scales important for generation of convective elements. Therefore the parametrization of convective cloudiness is still necessary in order to produce a realistic simulation. The most obvious improvement is the modification of the treatment of stratiform cloudiness by introducing a predictive equation for cloud-water content (Sundquist and Schlesinger, 1988).

The importance of the predictive cloud-water field resides in the fact that the growth of small cloud particles to the size of precipitating particles could take for stratiform clouds several hours. Therefore, the introduction of a partition between precipitating water and cloud water should improve prediction of the onset of precipitation. Additionally, the cloud water could be advected by the horizontal wind and interact with the hydrological cycle of the model. The representation of this interaction in a weather prediction model is also essential to link different physical processes, including vertical turbulent mixing and radiative properties of the atmosphere (Pudykiewicz et al., 1991).

In various NWP models the Kain-Fritsch (KF) (Kain and Fritsch, 1993) convective parametrization scheme is used for predicting convective rain, which cannot be directly resolved by the model. It has been improved in specific convective environments using feedback from forecasters. Convective updrafts in the KF scheme are represented using a steady-state one dimensional entraining/detraining plume model, where equivalent potential temperature and water vapour are both entrained and detrained. Most of the condensate produced in the updraft is converted to precipitation and a portion of this precipitation drives the downdraft through evaporative cooling effects. The remaining precipitation arrives at the surface. A cumulus parametrization scheme was proposed by Emanuel (1991). The heart of the scheme is the representation of moist convective transport within clouds (subcloud-scale drafts) using a buoyancy sorting technique, which determines the level of ascending or descending air parcels by finding the level where the liquid water potential temperature of the parcels equals that of the environment. In order to improve cloud parametrization in NWP models different research models are analysed. The microphysical cloud structure has been studied using a research time-independent three-dimensional non-hydrostatic model by Wang (2007). 5 classes of hydrometeors have been considered in thunderstorm structure: cloud water, cloud ice, rain snow, graupel/hail.

1.2 Main resources for cloud studies

Observations of cloud amount and type are an important tool in weather forecasting and climatology studies. Before the age of satellite, cloud amounts and cloud types were observed and recorded routinely at ground-based observatories. With the coming of operational satellites, clouds may now be observed from both ground and satellite platform.

In this section the principal sources available to build a climatology of cloud cover are introduced. The data, obtained from ground-based or satellite, have different spatial and temporal resolution,and also cloud properties inferred by ground-based or satellite data have different characteristics.

The ground-based measurements of cloud cover are traditionally made from visual observation, and the classification is based on height and shape of clouds. In the last decades also instrumental measurements (i.e. ceilometers, visible and infrared sky cameras, meteorological radar) are placed side by side to human observation: they integrate cloud cover measurements giving more information about height, temperature, hydrometeors of cloud lower levels. Moreover by using satellite besides cloud cover other cloud parameters, linked to radiative proprieties, can be inferred: cloud optical thickness, effective cloud radius of cloud particles, cloud top temperature and pressure.

1.2.1 Synoptic surface observation

Synoptic observations are a set of different meteorological parameters measured from ground stations. Each national or regional meteorological service is in charge of the station net into its territory.

Measurements and observations are made at fixed hours (typically every 3 hours). The cloud cover and other cloud parameters as height and type of clouds are obtained by visual observation: cloud cover is recorded as sky eighth of cloudiness (okta code). Although the Word Meteorological Organization (WMO) has defined standard methodologies to offer high quality and homogeneous data, the visual observation datasets are influenced by subjective interpretation and personal experience. The synoptic observations have problems to obtain high quality data in daily cycle due to low resolution measurements during nighttime. The availability of data is also a problem, for example getting a continuous dataset at sea surface. In spite of these, synoptic observations are the unique tool available to build a climatology over 50 years. The focus of cloudiness climatology studies is to get an accurate long time set of data for regional area rather than having time discontinuous dataset for global coverage. Using synoptic observations several cloudiness climatology studies (Henderson-Sellers, 1992; Karl and Streurer, 1998; Sun and Groisman, 2000) are realised for long period, over hundred years. They showed a tendency toward an increase in cloudiness in most areas. Positive trends have been reported for Europe, the United States, the former U.S.S.R., Canada and Australia. There are some indications that the increase in cloudiness is the cause of the observed reduction in the diurnal range of surface temperature (Karl et al., 1993). Besides the areas with positive trends in cloudiness, there are, however, others, such as China, that mainly have the opposite behaviour (Kaiser, 1998; Kaiser, 2000). Moreover Maugeri et Al. 2001 have shown that there is a highly significant negative trend in total cloud amount all over Italy. It is evident in all seasons and is particularly steep in winter where both in Northern and Southern Italy the decrease exceeds 1 okta in 50 years.

Recently many meteorological services are getting automatic observations in order to increase the accuracy of data and reduce costs. In the United

States ASOS (Automated Surface Observing System) systems have been used for over ten years. These systems provide, besides traditional meteorological parameters, cloud amount and height. The main instrument is laser beam celoimeter, it routinely sends laser pulse in vertical path and it measures backscattered radiation. Although the cloud data are related only to the portion of sky above the instrument, the measurements are representative because of their time sampling (every 30 seconds). In United Kingdom MetOffice has been using a net of automatic stations where the cloud cover has been measured by sky camera with fish-eyes lens. Sky camera images are provided at infrared and visible frequencies.

1.2.2 Ground-based radar

The radar ground-based at different wavelengths is able to probe the cloud structure with spatial and temporal resolution proper for detailed observation of most cloud processes. Radar meteorology, during his halfcentury history, allowed the recognition of typical cloud structures and their classification, especially for convective systems, and, given the great operational capabilities, is one of the pillars of any weather monitoring system (Atlas, 1990).

The radar is an active instrument that emits radiation at a known frequency and intensity, and measures the part of the same radiation that is backscattered by the target. The typical radar frequencies are Microwave: MW radiation is able to penetrate cloud envelop and rain layers. A wide range of e.m. wavelengths (λ) are used for meteorological application as is shown in table 1.1. In particular the S-band radar, long-range precipitation radar is broadly used in USA and in tropical regions where the precipitations are heavy. The C-band radar, largely used for precipitation in Europe is the best compromise between engineering problems and meteorological performance. The X-band radar with a smaller λ allows to reduce the validation

Frequency(GHz)	Wavelength (cm)	Band	Meteorological application
2-4	15.00-7.50	S	long-range precipitation (USA-tropical)
4-8	7.50-3.75	C	precipitation (Europe-Mediterranean)
8-12	3.75-2.40	X	precipitation (mountain regions)
27-40	1.13-0.75	K_a	cloud droplet
40-75	0.75-0.40	V	cloud droplet
75-110	0.40-0.27	W	cloud droplet

Table 1.1: Frequency bands of radar.

errors due to non-meteorological phenomena, for instance it is used to detect precipitation in mountains regions where the relieves obstruct and damage the signal. Finally the cloud radar as the K_a, V and W band radar (with λ less than 1 cm) allow the detection of cloud droplets, but are affected by strong attenuation phenomenon

The main goal of a weather radar is to retrieve information from the cloud precipitation layers. In most national meteorological services the radar network is the primary source of precipitation information. Although most of meteorological radar applications are dedicated to precipitation, cloud structure and proprieties are also observed. Radar observation makes possible not only the detection of typical structures of convective clouds like vortices, hooks, mesoscale organization (see Atlas, 1990 and Doviak and Zrnic, 1993 among others), but also the classification of hydrometeor types. Ground-based cloud radars are used to estimate the vertical profile of cloud microphysical characteristics, deriving cloud properties (as liquid water content or effective radius) from a single measurement of radar reflectivity (e. g. see

Fox and Illingworth, 1997 for stratocumulus and Brown et al., 1995 for cirrus clouds). A supercell storm was observed in Colorado by Marwitz (1972) using a radar in S-bands. These observations clarified and refined the descriptive model of super cell storms by Browing (1965). Clothiaux et al. (1995) have demonstrated that a ground based 94 GHz radar can be used to investigate parameters such as cloud layering, depth, and boundaries. Further radar data allowed to infer insights of tornado structures (e.g. Wurman and Gill, 2000, and Dowell et al., 2004).

Special features of convective storms using radar reflectivity and microphysical analysis were studied also in Europe from 1970s. The presence in the Po Valley of hailstorms with peculiar characteristics was evidenced by Prodi (1974) using radar and conventional data: motion characteristics and hail pattern were classified and related to wind shear conditions, while microphysical and chemical analysis were carried out on hail samples collected in different positions of the storm and at different life stages and compared with reflectivity by Prodi and Wirth (1973). P.F. et al. (1991) carried on a study on the meso- and micro-scale structure of the kinematics and precipitation formation of a squall line which occurred in Southern Germany and initiated as part of the synoptic-scale frontal zone, using polarimetric and Doppler radar measurements. S-band doppler Radar observations of precipitation cloud structure on the Mediterranean side of the Alps were made by Houze et al. (2001) during Mesoscale Alpine Programs (MAP).

Radar is also placed on board satellite. For the first time, in 1997, in order to detect precipitation, Precipitation Radar (PR) was launched on board TRMM (Tropical Rainfall Measuring Mission, staff, 2007) and in 2006 in order to detect clouds, Cloud Profiling Radar (CPR) was launched on board CloudSat (these mission will be more extensively described in section 1.3.2).

1.2.3 Space-borne passive sensors

The satellite history goes back to 1960 when the US polar-orbit satellite TIROS-1 was launched, this satellite was the first to be fully dedicated to meteorology. The image-making instrument on TIROS-1 was a vidicon camera, then it has been replaced with multispectral radiometer. The most recent are geostationary satellite, GOES was launched by USA in 1975, and in 1977 METEOSAT by Europe. Thus over 30 years of data are available in order to join ground-based observations, and to integrate the ground based observing systems.

Cloud cover retrieval from satellites can help to deal with some deficiencies of the other observing systems, spatial coverage above all. However the price to pay is the degradation for spatial and temporal resolution and the lower reliability of the cloud parameter estimation. Most satellite sensors are passive instruments, as they merely collect radiation emitted from the Earth-atmosphere system. Nearly all present meteorological satellites are in one of two type orbits, sunsynchronous also called, Low Earth Orbit (LEO) and geosynchronous and also geostationary (GEO). In this section we will describe the main instruments on board satellite in GEO and LEO orbits.

A LEO satellite travels on a near-circular orbit around the globe. The orbit can be located between 400 and 1500 km height from the Earth's surface, and the most of them scan the same Earth portions two times per day. This orbit allows to scan also polar region. A GEO spacecraft orbits at 36.000 km, at the same angular velocity of the Earth rotation, thus remaining in a fixed nominal position with respect to the Earth's surface, the sensor scans the disk every 15-30 minutes depending on the system. Until now only sensors in VISible (VIS) and InfraRed (IR) can operate on board geostationary satellite. The advantages of estimate cloudiness and clouds parameters by GEO data are the wide coverage and the good spatial (around 3x3 km^2at the sub-satellite point) and temporal resolution. On the other hand LEO satellite has an higher spatial resolution than GEO allowing the detection of more details of clouds and their proprieties, to the detriment of low temporal resolution.

The characteristics of the satellites used for cloud studies are reported in table 1.2.

Sensor	*EMS bands*	*Platform*	*Orbit*	*Agency*
SEVIRI	VIS-NIR-IR	Meteosat 8-9	GEO	EUMETSAT
VAS	VIS-NIR-IR	GOES 11-12	GEO	NOAA
VHRR	VIS-NIR-IR	INSAT	GEO	ISRO
		MT-SAT 1R-2	GEO	JMA
IVSSR	VIS-NIR-IR	FY 2C-2D	GEO	CMA
MODIS	VIS-NIR-IR	EOS-Aqua and Terra	LEO	NASA
MERIS	VIS-NIR-IR	ENVISAT	LEO	ESA
POLDER 1-2	VIS-NIR(polarized)	ADEOS 1-2	LEO	CNES/JMA
AHVRR	VIS-NIR-IR	N 17-18	LEO	NOAA
		METop	LEO	EUMETSAT
IASI	IR-hyperspectral	METop	LEO	EUMETSAT
		FY-1-3	LEO	CMA
HIRS	IR-sounders	N 17-18	LEO	NOAA
VIRR and VHSR	VIS-NIR-IR	FY-1-3	LEO	CMA
MISR	VIS	EOS-Terra	LEO	NASA

Table 1.2: Main satellites description (orbit, sensor and range frequencies of sensor) employed to study cloud. Acronyms are listed in Acronym section.

The International Commission on Illumination (CIE) defines visible and infrared part of electromagnetic spectrum into these regions:

- VIS: VISible, [0.38,0.75] μm;
- SWIR: Short wave InfraRed, [0.75,1.40] μm;
- MWIR: MidWave InfraRed, [3.00,8.00] μm;

- LWIR: LongWave InfraRed, [8.00,15.00] μm;
- FIR: Far InfraRed, [15.00,1000.00] μm;

but most sensors have a bandwidth that covers wavelength in more CIE regions. Thus we re-arranged the classification to a more practical use within this range:

- VIS: VISible, [0.4,1] μm;
- NIR: Near InfraRed, [1,3] μm;
- IR: InfraRed, [3,15] μm;
- MW: MicroWave, [0.1,100] cm;

1.2.4 Space-borne observation's state of art

Space-borne sensors collecting data in the VIS, IR and MW part of the spectrum allow analysis of cloud features and cloud structure. One of the early satellite-based cloud studies was probably the introduction of a classification of Mesoscale Convective Systems and Complexes, based on cloud area properties using IR data from geostationary sensors (Maddox, 1980): for this study the broad view provided by geostationary sensor made the observation of the mesoscale organisation of convection possible. Along this line, Morel and Senesi (2002) used similar approach to perform a climatological study on organized convection in the European area, taking advantage of long lasting time series of Meteosat observation. Other pioneering work, more oriented to operational use of satellite data. proposed techniques to use satellite data in a nowcasting environment (Purdom, 1982) and to better define conceptual models of meteorological systems (Browning and Hill, 1984). More detailed analysis of cloud top was made by Chang and Li (2002) that proposed a cloud microphysics retrieval technique applied to the MODIS data to estimate the vertical profile of cloud particle effective radius (Re) for stratiform water clouds using multispectral near-infrared (NIR) measurements. Rosenfeld and Gutman (1994) using a multispectral (5 channels from VIS to IR) analysis retrieved the effective radius.

Using low orbit sensors, the thermal structure of convective cloud top has been analysed describing structures such as U- and V-shapes, and warm cores (Negri, 1982; Heymsfield and Blackmer, 1988). Different work reported the technique to construct the cloud structure using ground-based data combined to satellite. For example Celano (2007) analysed the vertical cloud structure combined ground-based meteorological radar in C-band to data from SEVIRI and MODIS in VIS and NIR bands. The classification and retrieval algorithms are applied and the cloud volume is reconstructed in terms of hydrometeor type distribution, cloud top temperature, cloud particles effective radius, cloud optical depth, cloud top particles phase and rainrate at the ground. Ackerman and Cox (1998) estimate the cloud cover from ground-based sky-camera and satellite data during GARP Atlantic Tropical Experiment (GATE). They presented a method which enables to construct a three-dimensional representation of cloud structure. The ground-based measurements are also employed to evaluate some cloud characteristics retrieved by satellite. Wolters et al. (2007) evaluate the cloud-phase retrieval method for SEVIRI, MODIS and ISCCP (International Satellite Cloud Climatology Project) using ground-based lidar and cloud radar data.

The Microwave spectrum is also investigated to analyse cloud feature and structure. As the case of visible and infrared techniques, microwave techniques can benefit by the use of a cloud model, Mugnai and Smith (1984) were the first to couple two-dimensional, time-dependent cloud model with a microwave radiative transfer model to produce estimates of microwave brightness temperature at satellite altitude from convective clouds. These studies continued (Mugnai and Smith, 1988a, Mugnai and Smith, 1988b, Adler et al., 1991) and had revealed the importance of cloud water, ice, crystal, and vertical microphysical structure of the cloud on the upwelling microwave radiation. Other works which employed MW radiation to detect cloud structure, are focused on Mesoscale Convective Systems (MCS). The analysis of type, size and intensity of convective systems estimated from 85 GHz gave a contribution to tropical rainfall (Mohr et al., 1998). The cloud clusters were grouped into four classes of basic system types, based on size and minimum enclosed 85-GHz brightness temperature to indicate the presence or absence of large areas of active, deep convection.

Different techniques have also been proposed to classify cloud systems with multispectral imagery. Several cloud detection tests were used in the cloud mask algorithm, discriminating clear sky from clouds, which considered 14 of the 36 MODIS bands from VIS to IR (Ackerman et al., 1998), and provided a near real time product. Five channels AVHRR images have been used by Saunders and Kriebel (1987), coupled with radiative transfer calculation to infer cloud cover and cloud type, for climatological studies, while (Karlsson, 1989) developed an operational scheme for Scandinavian region, where the low orbit satellites ensures good coverage. Other approaches, based on clustering techniques (Desbois et al., 1982; Porcú and Levizzani, 1992), neural networks Bankert (1994), apply on both low orbit or geostationary satellite data. Others techniques of cloud mask and cloud classification will be presented in section 3.1.1.

A particular emphasis has been devoted, since early days of satellite meteorology, to the rainfall estimation from satellite, trying to relate precipitation at the ground with cloud top structures following statistical or physical approaches. A comprehensive review of techniques and relevant issues can be found in Barrett and Martin (1981), while more recent developments are treated in Levizzani (2003).

The spectrally detailed VIS-NIR-IR cloud analysis, now available on geosynchronous platforms, makes rain delineation algorithms physically based on the retrieval of cloud particles effective radius (Re) possible (Rosenfeld and Lensky, 1998; Capacci et al., 2004).

1.3 International cloud projects

During last decades, since the satellite data era was born, several satellites (see table 1.2) which some sensor's channels have been employed in cloud detection were launched. But only one mission has been dedicated to cloud (CLoudSat). In addition ISCCP project collects data to produce global cloud climatology. In this section CloudSat mission and ISCCP project are described.

Moreover there are many other mission not exclusively dedicated to clouds but that includes clouds studies and products. Some of these missions are sketched out in this section.

1.3.1 ISCCP

The International Satellite Climatology Project (ISCCP) is the first project of the World Climate Research Programmer (WCRP) (Schiffer and Rossow, 1983). Its goal is to collect and analyse satellite radiance measurements to infer the global distribution of clouds, their properties, and their diurnal, seasonal, and interannual variations (Rossow and Shiffer, 1999). Data collection began in July 1983 and is currently planned to continue through 30 June 2010. The resulting datasets and analysis products are used to improve the understanding and the modelling of the role of clouds in climate. Its primary focus is the elucidation of the effects of clouds on the radiation balance. These data can also used to support many other cloud studies, including understanding of the hydrological cycle.

	DX *(pixel level)*	*D1* *(gridded)*	*D2* *(Climatological)*
spatial Res.	30km mapped-pixels	280km equal-area grid	280km equal-area grid
temporal Res.	3 hr	3hr	monthly
coverage	individual satellites	global	global
contents	Calibrated radiances, cloud and surface prop. properties from radiative analysis.	Spatial averages of DX quantities including including properties of cloud types.	Monthly average of D1 quantities mean including diurnal cycle.

Table 1.3: 3 levels of ISCCP cloud product.

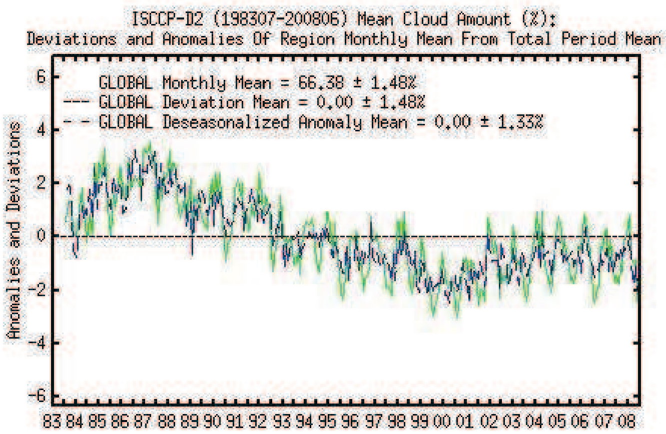

Figure 1.2: The anomalies to the percentage of mean cloud amount from 1983 to 2008 by the D2-ISCCP product.

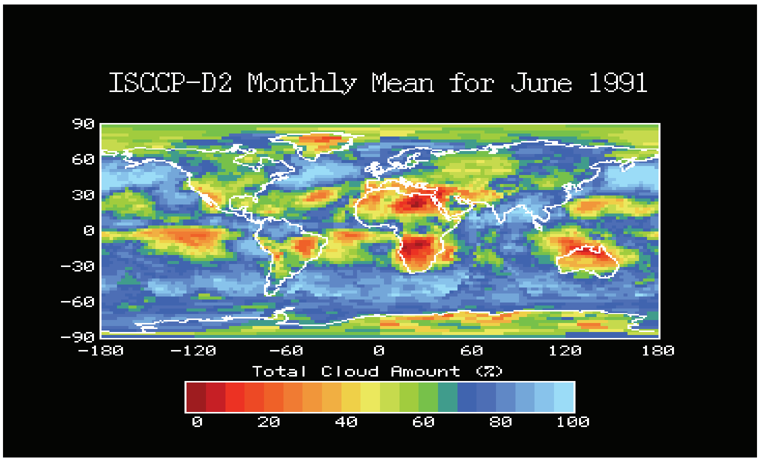

Figure 1.3: The Percentage of cloud cover by D2 product.

Data are collected from the suite of weather satellites operated by several nations and processed by several groups in government agencies, laboratories, and universities.

The global coverage is obtained by using combined 5 geostationary satellites (GOES-E, GOES-W, METEOSAT, GMS(MTsat), INSAT) and one or more polar (mainly NOAA). The data from polar are necessary to cover polar regions, where geostationary data are degraded because of the view satellite angle.

*1.6 The cloud products are provided at different spatial and temporal resolution and with different contents. The DX, D1, D2 products are described in table 1.3. The DX is the product at highest resolution: temporal is 3 hours and the nominal spatial resolution is 30km, its coverage is individual satellite. The D1 and D2 have 280km of spatial resolution at equal-area grid and a global coverage but D2 is provided every 3 hours, while D2 monthly. An example of the percentage of coverage of D2 products is shown in figure 1.3 and the the anomalies to the mean cloud amounts from the 1983 to 2008 calculated by D2 products are plotted in figure 1.2

1.3.2 CloudSat

CloudSat is a NASA Earth Sciences Systems Pathfinder (ESSP) mission. ESSP missions are relatively low cost missions that require that the mission be built, tested and launched in a short time interval (normally within 3 years).

The purpose of the experimental CloudSat mission is to measure the vertical structure of clouds from space and, for the first time, simultaneously observe clouds and precipitation. CloudSat seeks to help solving some deficient knowledge of cloud and stimulate improvements in both forecasting and climate prediction. The primary CloudSat instrument is a 94-GHz, nadir pointing, Cloud Profiling Radar (CPR) which measures the power backscattered by clouds as a function of distance from radar. The CPR Pulse Repetition Frequency (PRF) is 4300 pulse/sec, the footprint for a single profile is approximately 1.3 km (across-track) by 1.7 Km (along-track). CPR profile is generated every 1.1 Km along track and each one has 125 vertical ”bins” thicken 24 m. (Stephens et al., 2002). A millimetre-wave radar operated in a vertically pointing mode, as CPR, is an attractive solution for the observation of low-altitude low-reflectivity clouds such as fair weather cumuli (Lhermitte, 1988).

A unique aspect of this mission is the fact that CloudSat is flying in formation with other Earth Sciences missions. CloudSat is a part of a constellation of satellites (the A-Train) that currently include NASA’s EOS Aqua and Aura satellites as well as a NASA-CNES lidar satellite (CALIPSO) and CNES satellite carrying polarimeter (PARASOL). A unique feature that CloudSat brings to the constellation is the ability to fly a precise orbit enabling the fields of view of the CloudSat radar to be overlapped with the lidar footprint and the other measurements of the constellation. The precision of this overlap creates a unique multi-satellite observing system for studying the atmosphere processes of the hydrological cycle.

Figure 1.4: A-train instruments.

1.3.3 Other missions and projects

Medium-spectral Resolution Imaging Spectrometer (MERIS) mission has been launched by ESA in March 2002. MERIS primary scope is observing ocean colour. While secondary objectives of the MERIS mission are directed to the understanding of atmospheric parameters associated with clouds, water vapour and aerosols in addition to land surface parameters. The large influence of the atmosphere on the diversity of target reflectances to be observed by MERIS necessitates a rather complex radiometric correction scheme. In order to verify the corrections of the data sets various validation procedures have and are being developed using not only different radiative transfer procedures, but also different atmospheric components as input to complex simulation taking advantage of a MERIS system and data simulator (Albert et al., 2001). However, atmospheric constituents are not only being treated as noise and removed by the MERIS atmospheric correction scheme, but also there is a considerable range of ”by-products” leading to valuable geophysical variables such as: cloud top height, cloud albedo, water vapour column abundance.

Another mission dedicate to clouds and atmospheric parameters observations is Polarization and Directionality of the Earth's Reflectances (POLDER). This instrument is designed to accurate observations of the polarized and directional solar radiation reflected by Earth-atmosphere system. The first (POLDER-1) was launched in 1996 aboard the Japanese ADEOS-1 (ADvanced Earth Observing Satellite) platform, and the second (POLDER-2) in 2002 on board ADEOS-2. The sensor's unique features, compared to the current instrument, include its ability to: 1) measure polarized reflectance in the visible and near infrared spectral regions; 2) observe Earth target reflectance from 12 directions during a single satellite pass; 3) operate in two dynamic modes in order to achieve both high signal to noise ratio and wide dynamic range (Deschamps et al., 1994). For cloud analysis POLDER measurements are processed to produce cloud product such as cloud optical and physical parameters (more details in Buriez and Coauthors, 1997), this processing includes cloud detection (Breon and S., 1998).

Statistics on clouds have been compiled from the High-resolution Infrared Radiation Sounder (HIRS) sensors on the NOAA satellites since June 1989 by Wisconsin University. The HIRS channels with partial CO_2 absorption from 13-15 μm, provides the detecting semi-transparent clouds. The method has also been referred to as "$\mathrm{CO_2}$ Slicing." (Wylie et al., 1994; Wylie and Menzel, 1999). These cloud statistics were compiled as a complement to the ISCCP. The ISCCP currently does not use the HIRS data for cloud detection and height determination. The Wisconsin HIRS Cloud Climatology reports more clouds in the upper troposphere than the ISCCP. A comparison of the two data sets can be found in Jin et al., 1996.

New types of information for scientists studying Earth's climate are provided by Multi-angle Imaging SpectroRadiometer (MISR). Viewing the sunlit Earth simultaneously at nine widely spaced angles, MISR provides ongoing global coverage with high spatial detail. Its imagery is carefully calibrated to provide accurate measures of the brightness, contrast, and colour of reflected sunlight. MISR has four spectral bands centred at 446 nm, 558 nm, 672 nm, and 866 nm. It views the earth with its nine pushbroom cameras-four forward, one nadir, and four backward looking. Relative to the earth surface, the viewing angles are 0 26.1, 45.6, 60.0, and 70.5. The time interval for a scene to be viewed by all cameras is 7 min, and the swath width is about 400 km. The spatial resolution ranges from 275 m to 1100 m, depending on spectral channel and camera (Diner et al., 1998). MISR instrument is flying onboard the polar platform EOS-Terra. Due to its unique nine-angles configuration, MISR can retrieve cloud parameters such as cloud-motion vectors ans cloud-top heights using a purely geometrical technique that involves locating the same cloud features at different viewing angles (Moroney et al., 2002). These clouds parameters are products available by MISR mission.

There are also different climatology international project not directly interested on clouds, but focus on climate change, energetic budget and hydrological cycle in which clouds play an important role. These projects often use the results of specific clouds project. For example the ISCCP results and data are into The Global Energy and Water Cycle Experiment (GEWEX)(more details in: *http : //www.gewex.org/gewex_overview.html*) and in the the World Climate Research Programme (WCRP)(more detail: *http : //wcrp.wmo.int/wcrp − index.html*).

Chapter 2

Cloud remote sensing at VIS,NIR,IR wavelenghts

Energy transfer from one place to another essentially is accomplished by three processes. *Conduction* is the transfer of kinetic energy of atoms or molecules by contact among molecules travelling at varying speeds. *Convection* is the physical displacement of matter in gases or liquids. *Radiation* is the process whereby energy is transferred across space without the necessity of transfer medium. This chapter illustrates the main interactions between radiation and atmosphere.

The observation of a target by a device separated by some distance is the act of remote sensing: space borne sensor remote sensing for meteorological purposes have been largely confined to passive detection of radiation emanating from the earth/atmosphere system.

The basic principle associated with remote sensing of the atmospheric components (gases, aerosols and cloud particles) involves the interpretation of radiometric measurements of electromagnetic radiation in specific spectral intervals which are sensitive to some physical aspects of the medium.

The interaction of electromagnetic radiation with matter modifies the

incident wave producing a “signature” in the amplitude, phase or spectral composition each depends on composition and structure of the medium.
The medium *scatters*, *absorbs* and *emits* electromagnetic fields in different ways depending on the wavelength considered. This means that radiation at different wavelength can bring to the sensor different information (this is the main reason for using multispectral remote sensing).

After an introduction to fundamental radiometric quantities, in this chapter the basic theory of VIS-NIR-IR radiative transfer in the atmosphere is outlined. Finally some cloud parameters are presented. Reference texts for this chapter are Liou (2002), Stephens (1994) and Kidder and Vonder-Haar (1995).

2.1 Radiometric quantities

Many of the units used to quantify the electromagnetic (e.m.) radiation are based on energy. The rate of energy ($\mathcal{E}$) transfer by e.m. radiation is called the *radiant flux*, which has units of energy per unit time. It is denoted by:

$$F = d\mathcal{E}/dt \tag{2.1}$$

and it is expresses in watt ($W = J/s$). The radiant flux density is the radiant flux crossing a unit area, measured in W/m^2, and it is called *irradiance* (E). All energy-based quantities denoted by the words *monochromatic* or *spectra*l indicate the wavelength dependence of the radiation. A subscript λ or ν is used to indicate whether wavelength or frequency is being considered.

In general, the irradiance upon an element of surface area may consist of contributions that come from all directions. It is sometimes necessary to identify the part of the irradiance that is coming from directions within some specified infinitesimal arc of solid angle $d\Omega$ (as is shown in figure 2.1). The irradiance per unit solid angle is called *radiance*,

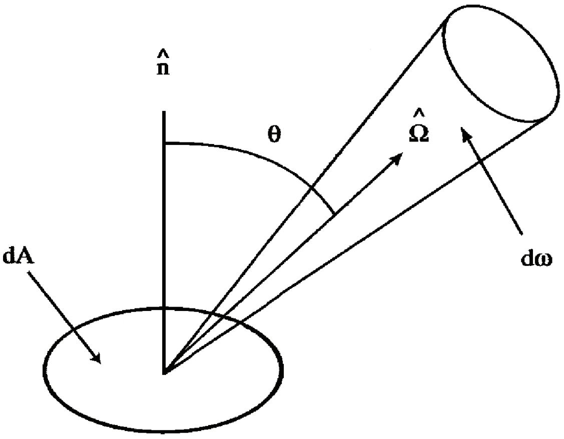

Figure 2.1: Radiant energy toward the $\hat{\boldsymbol{\Omega}}$ direction and across the surface dA.

$$I_\lambda = \frac{d\mathcal{E}}{dt\, dA\, d\lambda\, d\Omega} \tag{2.2}$$

it is measured in $W/m^2 \mu m\ sr$. With the monochromatic radiance (also called spectral radiance L_λ) definition, radiance is readily seen to be the integral over all wavelength of frequencies:

$$I = \int_0^\infty I_\lambda \, d\lambda = \int_0^\infty I_\nu \, d\nu \tag{2.3}$$

so that:

$$I_\lambda = -\frac{\nu}{d\lambda} I_\lambda = \frac{\nu^2}{c} I_\lambda \tag{2.4}$$

where c is the speed of light.

In order to express quantitatively the relationship between irradiance and radiance , it is necessary to define the zenith angle (θ) as the angle between the direction of the radiation and the normal to the surface (see figure 2.1). The component of the radiance normal to the surface is given by $I_\lambda\ cos\theta$. The irradiance represents the combined effects of the normal component of the radiation coming from the whole hemisphere; that is

$$E_\lambda = \int_\Omega I_\lambda(\vec{s}, \hat{\Omega})\ cos\theta\ d\Omega \tag{2.5}$$

where in spherical coordinates $d\Omega = sin\theta \, d\theta \, d\varphi$.

A radiation field is said to be *isotropic* if $I_\lambda(\vec{s}, \hat{\Omega})$ does not depend on $\hat{\Omega}$, so that $E_\lambda = \pi \, I_\lambda(\vec{s})$, and homogeneous if $I_\lambda(\vec{s}, \hat{\Omega})$ does not depend on $\vec{s}$.

Radiance or specific intensity has the useful property of being, in free space, independent of distance from an object, as the viewing angle is not changed. In fact, both the irradiance and the surface subtended solid angle will inversely decrease with the square of the distance, so that in the radiance (the ratio between these two quantities) the distance dependence will cancel out.

2.2 Interactions between radiation and matter

One basic type of interaction between radiation and matter can be summarized by a photon transferring all of its energy to an atom or a molecule and thus being removed from the radiation field. The energy of the photon raises an electron to a higher energy level or a molecule to higher rotational or vibrational states. This increase in energy of the receiving atom or molecule can be released in several different ways.

Radiation interacts with atmospheric components with three different mechanisms:

- *absorption*: is the way by which the energy of a photon is taken up by matter, typically the electrons of an atom or molecules. The activated molecule (or atom) collides with another molecule, and drops back into a lower energy state; the energy freed becomes kinetic energy of the molecules and corresponds to warming the gas. In this case the photon is permanently lost and the radiation field attenuated.
- *emission*: involves the conversion of molecular kinetic energy (ther-

mal energy) into electromagnetic energy (photons). This occurs when molecules are activated by collisions with each other and the activation energy is emitted as photons. Furthermore, it is a process by which the energy of a photon is released by another entity, for example, by an atom whose electrons make a transition between two electronic energy levels.

- *scattering*: a photon is absorbed by the molecule and its energy increase. When this energy is released a photon identical to the absorbed one except for its direction of propagation is emitted. Thus, a spontaneous transition drops back the molecule into its original state. The photon remains part of the radiation field but the beam is reradiated in all directions.

2.2.1 Concepts of scattering

Blue sky, white clouds, rainbows and halos are all optical phenomena produced by scattering. Scattering is a fundamental physical process associated with light and its interaction with matter. It occurs at all wavelengths throughout the entire electromagnetic spectrum.

The particles, that scatters energy along the path of electromagnetic wave, may be thought of as a point of source of the scattered energy. In the atmosphere, the particles responsible for scattering cover the sizes from gas molecules ($\sim 10^{-4}\mu m$) to aerosols ($\sim 1\mu m$), water droplets ($\sim 10\mu m$), ice crystals ($\sim 100\mu m$), and large raindrops and hail particles ($\sim 1cm$).

A small anisotropic particle tends to scatter electromagnetic wave equally into the forward and backward directions. When the particle becomes larger, the scattered energy is increasingly concentrated in the forward directions. Distribution of the scattered energy involving spherical and certain symmetrical particles may be quantitatively determined by means of the electromagnetic wave theory (how can be expressed in next section).

In a scattering volume, which contains many particles, each particle is exposed to, and also scatters, the electromagnetic wave that as already been scattered by other particles. This phenomena is known as multiple scattering.

The effect of particle size on scattering is inferred by the physical term *size parameter*. For spherical particle it is defined as $x = 2\pi a/\lambda$, where a is the particle radius and λ is the incident wavelength. By using x we can find three different scattering regions:

- *Rayleigh scattering*, when $x \ll 1$. This is the case of scattering of visible radiation by atmospheric molecules;
- *Mie scattering*, when $x \gtrsim 1$. In this case particle sizes are comparable to or larger than wavelength, for example scattering of NIR radiation by cloud particle and aerosols. This scattering will be treated in next section;
- *geometric optics*, when $x \gg 1$. In this case the angular distribution of scattered radiation can be described by the principles of geometric optics. For instance rain droplets scatter VIS-NIR radiation.

Mie scattering

Considering a classic physical-based approach, we can express the radiation passing through the atmosphere or matter as a linear combination of monochromatic electromagnetic fields:

$$\vec{\mathbf{E}}_c = \vec{\mathbf{E}}_0 \, e^{i\vec{\mathbf{k}}\cdot\vec{\mathbf{x}} - i\omega\, t} \qquad \vec{\mathbf{H}}_c = \vec{\mathbf{H}}_0 \, e^{i\vec{\mathbf{k}}\cdot\vec{\mathbf{x}} - i\omega\, t} \tag{2.6}$$

with $\vec{\mathbf{E}}_0$ and $\vec{\mathbf{H}}_0$ steady vector.

In general the scattering problem is: *for a given object of known orientation, shape, size and optical property (refraction index), and for an incident* *monochromatic wave, determining the electromagnetic field inside and outside the object.*

The monochromatic electromagnetic field as indicated in the formula 2.6 has to satisfy the Maxwell equations inside and outside the object. This is a very complicated mathematical problem that, in general, can be solved only by numerical computation.

However assuming spherical and homogeneous particles the problem can be solved by Mie theory. The Mie solution in the far-field approximation consists of the explicit form of the diagonal scattering matrix components S_1 and S_2 in the following formula:

$$\begin{pmatrix} E_{\parallel} \\ E_{\perp} \end{pmatrix}_{\lambda,sca} = \frac{e^{ik(s-z)}}{-iks} \begin{pmatrix} S_2 & 0 \\ 0 & S_1 \end{pmatrix} \begin{pmatrix} E_{\parallel} \\ E_{\perp} \end{pmatrix}_{\lambda,i} \tag{2.7}$$

where s is the field propagation path and the incident and scattered fields are expressed according to the two orthogonal vectorial bases showed in figure 2.2. The functions S_1 and S_2 are series of Riccati-Bessel, Bessel and Legendre function linear combinations. We do not explicitly specify them, but it should be emphasised that for a fixed wavelength they depend upon the refraction index m_λ, the scattering angle θ and the size parameter x. The scattering angle is the angle θ in figure 2.2. Thus:

$$S_{\lambda,1} = S_{\lambda,1}\ (r, m_\lambda, \theta)$$
$$S_{\lambda,2} = S_{\lambda,2}\ (r, m_\lambda, \theta)$$

Once the incident field $E_{\lambda,i}$ is given and the scattering field $E_{\lambda,sca}$ determined from 2.7, it is possible to calculate some important quantities useful in describing the interaction of the radiation with an ensemble of atmospheric objects.

The *cross section* is defined as the analogous to the geometrical area of a particle, to denote the amount of energy removed from the original beam by

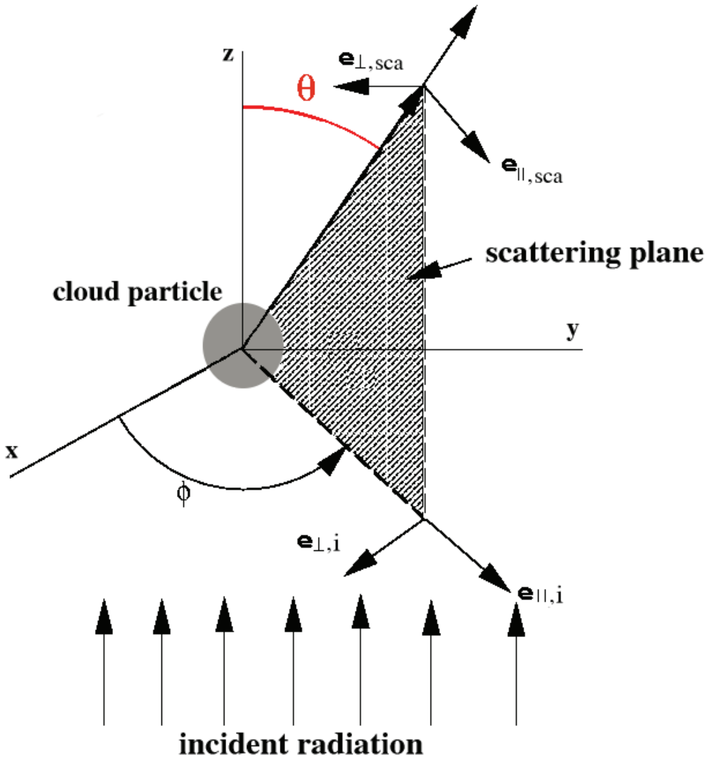

Figure 2.2: Scattering by homogeneous spherical particles

the particle, so its dimension is a surface $[m^2]$. Considering a sphere around the object, where we integrate the energy in time unit absorbed, scattered and extinguished: W_{abs}, W_{sca} and W_{ext}, scattering, absorption and extinction cross sections parameters are defined in this way:

$$\sigma_{\lambda,abs} = \frac{W_a}{I_i} \qquad \sigma_{\lambda,sca} = \frac{W_s}{I_i} \qquad \sigma_{\lambda,ext} = \frac{W_{ext}}{I_i}, \tag{2.8}$$

Also, the extinction cross section, in unit of area, is the sum of scattering and absorption cross sections:

$$\sigma_{\lambda,ext} = \sigma_{\lambda,abs} + \sigma_{\lambda,sca} \tag{2.9}$$

The calculation of the powers W is possible using the functions S_1 and S_2. As the flux of energy is calculated through a sphere around the object, the dependence upon the scattering angle is lost, so the cross sections depend only upon two parameters:

$$\sigma_{\lambda,abs} = f_{\lambda,abs}(r,m) \qquad \sigma_{\lambda,sca} = f_{\lambda,sca}(r,m) \qquad \sigma_{\lambda,ext} = f_{\lambda,ext}(r,m), \tag{2.10}$$

To know the scattering direction, it is necessary to define the phase function:

$$p_\lambda \equiv \frac{1}{\sigma_{\lambda,sca}} \frac{d\sigma_{\lambda,sca}}{d\Omega} = f_{\lambda,p}(r,m,\theta) \tag{2.11}$$

We introduce two other useful parameters: The single particle albedo:

$$\omega_\lambda = \frac{\sigma_{\lambda,sca}}{\sigma_{\lambda,ext}} \tag{2.12}$$

and the asymmetric parameter

$$g_\lambda \equiv \langle\cos\theta\rangle = \int_{4\pi} p_\lambda \, \cos\theta \, d\Omega \tag{2.13}$$

The first tells us how well the particle reflects the radiation. For zero albedo the incident radiation is not scattered at all, and for an albedo value of 1 it is all reflected. The asymmetry parameter g is used to evaluate the main scattering direction. When its value is positive, the main scattering is forward, when negative, backscattering is dominant.

2.2.2 The black body radiation

The laws of blackbody radiation are basic to an understanding of the absorption and emission processes.

According to Planck's radiation law, a blackbody emits unpolarised radiation uniformly in all directions with a spectral brightness or specific intensity:

$$(B_\lambda \equiv I_\lambda)_{black\ body} = \frac{2\,h\,c^2}{\lambda^5}\left(\frac{1}{e^{\frac{hc}{\lambda K_B\,T}} - 1}\right). \tag{2.14}$$

where K_B is Boltzman's constant, h is the Plank, c is the velocity of light and T is the absolute temperature.

For any temperature T, $B_\lambda(T)$ has a single maximum at a wavelength that may be determined by setting the partial derivative of $B_\lambda(T)$ with respect to λ equal zero. The results is known as *Wien's displacement law*:

$$\lambda_{max}T = 2897.8\,\mu m\;K, \tag{2.15}$$

where λ_{max} is the wavelength (expressed in micrometres) of maximum emission for a blackbody at temperature T (expressed in Kelvin). The solid black line in fig. **??** shows this relationship.

The Plank function have two different behaviours: referred to the *Rayleigh-Jeans distribution*:

$$B_\lambda = \frac{2\,c\,K_B\,T}{\lambda^4} \qquad when \quad \frac{2hc}{\lambda K_B T} \ll 1 \tag{2.16}$$

and referred to as the *Wien distribution*:

$$B_\lambda(T) = \frac{2\,h\,c^2}{\lambda^5}\,e^{-h\,c/K_B\lambda T} \qquad when \quad \frac{h\,c}{K_B\lambda T} \gg 1 \tag{2.17}$$

Nonblackbodies

Since real material is not a perfectly blackbody we can be quantify how closely it approximates a blackbody. The *emittance* of a body is defined as:

$$\varepsilon_\lambda = \frac{emitted\;radiation\;at\;\lambda}{B_\lambda} \tag{2.18}$$

Emittance can be a function of temperature and viewing geometry as well as wavelength. For a blackbody $\varepsilon_\lambda = 1$. Three related quantities describe the mechanisms of radiation incident on a body:

$$\alpha_\lambda = \frac{absorbed\, radiation\ at\ \lambda}{incident\ radiation\ at\ \lambda}, \tag{2.19}$$

$$\rho_\lambda = \frac{reflected\, radiation\ at\ \lambda}{incident\ radiation\ at\ \lambda}, \tag{2.20}$$

$$\tau_\lambda = \frac{trasmitted\, radiation\ at\ \lambda}{incident\ radiation\ at\ \lambda}. \tag{2.21}$$

respectively *absorptance*, *reflectance* and *trasmittance*. Because these three processes are the only possibilities for the incident radiation by energy conservation, each quantity must be between zero and one, and

$$\alpha_\lambda + \rho_\lambda + \tau_\lambda \equiv 1. \tag{2.22}$$

Kirchhoff discovered that a body is exactly as good an absorber as it is an emitter. This is summarized in *Kirchhoff 's law*:

$$\alpha_\lambda \equiv \varepsilon_\lambda. \tag{2.23}$$

This law applies only to material that is in *Local Thermodymamic Equilibrium* (LTE), which means that it can be characterized by a single thermodynamic temperature. This is a good assumption below about 100km in the Earth's atmosphere. Above 100km, collisions between molecules are rare enough that different chemical species can have different thermodynamic temperatures. For most satellite meteorology applications, however, the Earth's atmosphere can be considered to be in local thermodynamic equilibrium.

The atmosphere trasmittance depends on the absorption proprieties of its components at different wavelengths. Figure 2.3 shows the atmosphere trasmittance function depending on wavelengths. Where the trasmittance is close to 1, the atmosphere can be considered as a blackbody and these spectrum regions are called windows bands. H_2O, CO_2 and O_2 are the main gases that absorb radiation at VIS-NIR wavelengths. The spectrum bands of some satellite sensor are also shown in fig. 2.3. Most of these bands are placed in window regions but some other are also placed in absorption regions in order to sound the gas responsible of the absorption.

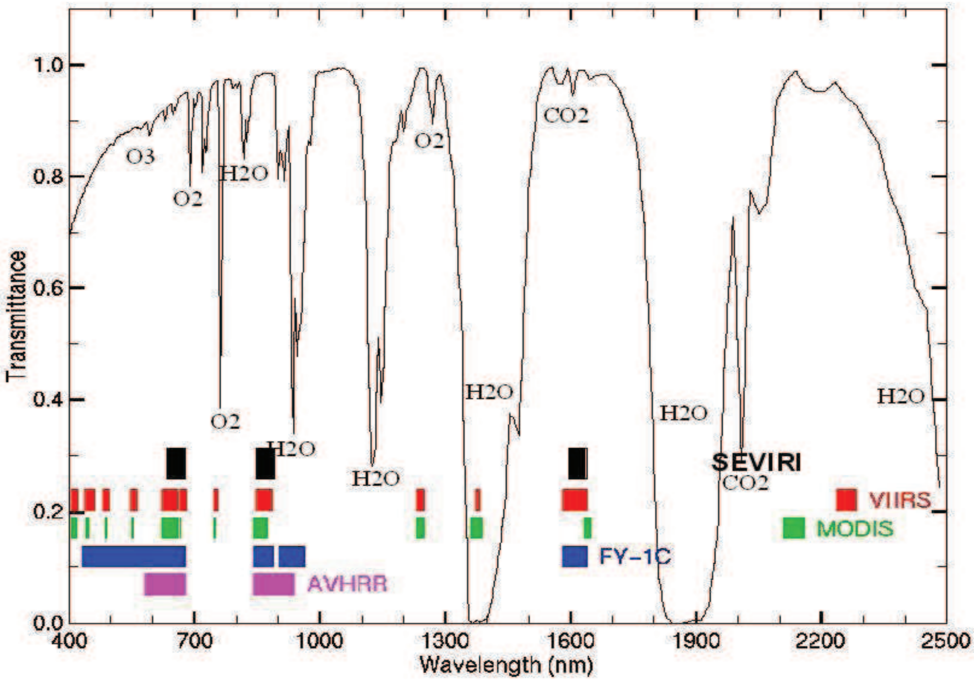

Figure 2.3: Atmosphere trasmittance at different wavelength form VIS to NIR. Colors bars represent the spectrum bands covered by different satellite sensors.

Brightness Temperature

One interesting parameter directly derived from B_λ is the *brightness temperature* (T), that is the temperature that corresponds to a particular Planck function value B_λ. This is determined by inverting the Planck function,

$$T = \frac{C_2}{\lambda \, ln(\frac{C_1}{\lambda^5 B_\lambda} + 1)} = \frac{C_2}{\nu \, ln(\frac{C_1 \nu^3}{B_\nu} + 1)} \tag{2.24}$$

As we have seen from Plancks Law, as temperature increases the radiance also increases; the percentage increase varies as a function of wavelength and temperature. The percentage change in radiance to a corresponding percentage change in temperature, called temperature sensitivity, α, of a given spectral band is defined as

$$dB/B = \alpha dT/T \tag{2.25}$$

For infrared wavelengths, we find that $\alpha \approx C_2\nu/T = C_2/\lambda T$. Thus the shorter wavelengths have a greater temperature sensitivity than the smaller longer wavelengths.

Consider two infrared windows 11 and 4 μm, for example; at 300 K, the temperature sensitivity for $11\mu m$ (longwave window) is 4.3 and for $4\mu m$ (shortwave window) it is 12. The temperature sensitivity indicates the power to which the Planck radiance depends on temperature, since B proportional to T^α satisfies the equation. Thus the radiance in the shortwave window is varying roughly as temperature to the twelfth power and in the longwave window roughly as temperature to the fourth power (Menzel, 2006). Figure 2.4 demonstrates the temperature dependence of the Planck Function B(,T) for infrared spectral bands between 4 and 15 microns for earth scene temperatures.

2.3 The Radiative Transfer Equation (RTE)

Radiative transfer serves as a mechanism for exchanging energy between the atmosphere and the underlying surface and between different layers of the atmosphere.

When dealing with radiation travelling in cloud and atmosphere, we need to consider these “objects” in terms of size, composition and their distribution along the path.

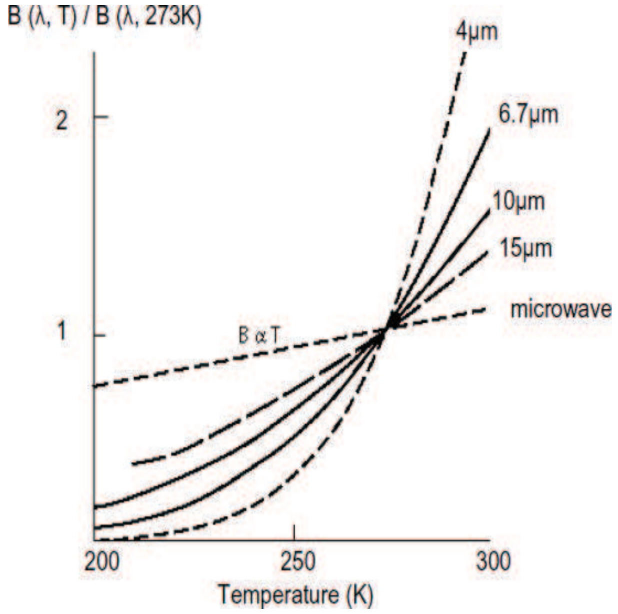

Figure 2.4: Temperature dependence of the Planck function B(λ,T) for earth scene by Menzel, 2006.

Consider a specific intensity or spectral radiance $I_\lambda(\vec{s},\, \hat{\Omega})$ incident upon a cylindrical elementary volume with cross section dA and length ds (see figure 2.5). Let this volume contain $n_0\, dA\, ds$ particles having the same size and composition, n_0 being the number of particles per unit volume. We want to find out the specific intensity of radiation coming out of the same volume in the same direction, that is $I_\lambda(\vec{s} + \hat{\Omega}\, ds,\, \hat{\Omega})$ for monochromatic radiation propagating along a line of sight distance $\hat{\Omega}$.

Each particle has a scattering cross section $\sigma_{\lambda,sca}$ and an absorbing cross section $\sigma_{\lambda,abs}$ for a total extinction cross section $\sigma_{\lambda,ext} = \sigma_{\lambda,sca} + \sigma_{\lambda,abs}$; this means that each particle absorbs the power $\sigma_{\lambda,abs} I$ and scatters the power $\sigma_{\lambda,sca} I$. Therefore the decrease of the specific intensity $dI_\lambda(\vec{s},\, \hat{\Omega})$ for the volume ds is

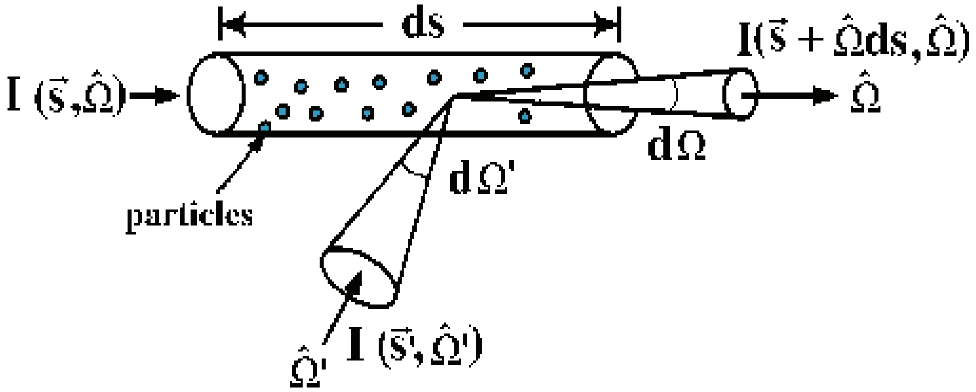

Figure 2.5: Radiative energy transfer for specific intensity $I_\lambda(\vec{s},\, \hat{\Omega})$ across an infinitesimal cylinder containing particles

$$dI_\lambda(\vec{s},\, \hat{\Omega})_{extinction} = -ds\, n_0(\sigma_{\lambda,sca} + \sigma_{\lambda,abs})\; I_\lambda(\vec{s},\, \hat{\Omega}) = -ds\, n_0\; \sigma_{\lambda,ext}\; I_\lambda(\vec{s},\, \hat{\Omega}) \tag{2.26}$$

Therefore, the intensity is increased by the emission of particles and can be written as:

$$dI_\lambda(\vec{s},\, \hat{\Omega})_{emission} = ds\, n_0\; (\sigma_{\lambda,abs})\; B_\lambda(T) \tag{2.27}$$

where $B_\lambda(T)$ is the Planck function that depends upon the temperature T.

Also the specific intensity increases because a portion of the specific intensity $I_\lambda(\vec{s}, \hat{\Omega}')$ incident on the volume from other directions $\hat{\Omega}'$ is scattered into the direction $\hat{\Omega}$, and is added to the intensity $I_\lambda(\vec{s},\, \hat{\Omega})$. Since the scattered intensity comes from all directions $\hat{\Omega}'$, the specific intensity contribution in the direction $\hat{\Omega}$ from the $n_0\, ds$ particles in the volume is:

$$dI_\lambda(\vec{s},\,\hat{\Omega})_{scattering} = ds\, n_0\, \sigma_{\lambda,sca} \int_{4\pi} p_\lambda(\vec{s},\,\Omega,\,\Omega')\, I_\lambda(\vec{s},\,\hat{\Omega}')d\Omega' \tag{2.28}$$

where $p(\vec{s},\,\Omega,\,\Omega')$ is the scattering phase function depending on the place and on the incoming and outgoing directions. Combining all these contributions and introducing the coefficients $k_{\lambda,abs} = n_0\,\sigma_{\lambda,abs}$, $k_{\lambda,sca} = n_0\,\sigma_{\lambda,sca}$ and $k_{\lambda,ext} = n_0\,\sigma_{\lambda,ext}$, we obtain the following radiative transfer equation (RTE):

$$\frac{dI_\lambda(\vec{s},\,\hat{\Omega})}{ds} = -k_{\lambda,ext}(\vec{s})\, I_\lambda(\vec{s},\hat{\Omega}) + k_{\lambda,abs}B_\lambda(T) + k_{\lambda,sca}\int_{4\pi} p_\lambda(\vec{s},\Omega,\,\Omega')I_\lambda(\vec{s},\hat{\Omega}')d\Omega' \tag{2.29}$$

where the terms on the right represent, respectively, the attenuation of the intensity along s due to absorption and outward scattering, the increase of intensity through emission due to temperature, and the increase of intensity due to scattering of incoming radiation into the line of sight direction. Thus the first term removes radiation from the beam and is known as *depletion term.* The last two add radiation to the beam and are known as *source terms.*

By introducing into the cylinder a population of particles with a size distribution $n(r)$, we can continue to use the equation 2.29 provided that the extinction, absorption and scattering coefficients are calculated in this way:

$$k_\lambda = \int_0^\infty n(r)\sigma_\lambda dr \tag{2.30}$$

More realistically, we can consider M kinds of particles with a size distribution $n^i(r)$ and cross sections σ^i_λ for $i = 1, ...M$. In this case, the expression 2.30 becomes:

$$k_\lambda = \sum_{i=1}^{M} \int_0^\infty n^i(r)\sigma^i_\lambda dr \tag{2.31}$$

Introducing the following parameters:

$$\tilde{\alpha}_\lambda = k_{\lambda,abs}/k_{\lambda,ext} \quad \text{absorption number} \tag{2.32}$$

$$\tilde{\omega}_\lambda = k_{\lambda,sca}/k_{\lambda,ext} \quad \text{single scattering albedo} \tag{2.33}$$

related by $\tilde{\alpha}_\lambda = 1 - \tilde{\omega}_\lambda$, and introducing the infinitesimal optical thickness $d\tau = k_{\lambda,ext}\, ds$, the 2.29 equation can be written in the following way:

$$\frac{dI_\lambda(\vec{s},\, \hat{\Omega})}{d\tau} = -I_\lambda(\vec{s},\, \hat{\Omega}) + \tilde{\alpha}_\lambda B_\lambda(T) + \tilde{\omega}_\lambda \int_{4\pi} p(\vec{s},\, \Omega,\, \Omega')\, I_\lambda(\vec{s},\, \hat{\Omega}')d\Omega'; \quad (2.34)$$

This is an integral-differential equation and its mathematical resolution it is difficult. Thus there are different numerical techniques and approximations to solve the 2.34. It may be approximated for the different parts of the spectrum, taking advantage of the relative dominance of scattering or absorption processes. Otherwise it can be numerically solving how will describe in next section.

2.3.1 RTE numerical resolution method

The Discrete Ordinate Radiative Transfer (DISORT) method resolves numerically the equation 2.34 (Stamnes et al., 1988). This algorithm is for time-independent transfer calculations in vertically inhomogeneous, non-isothermal, plane-parallel media. It has been designed to be as versatile and general as possible and should find applications from the UV through to the radar region of the electromagnetic spectrum. The physical processes included are thermal emission, scattering, absorption, and bidirectional reflection and emission at the lower boundary.

In order to solve the RT equation DISORT assumed two approximations:

- *plane parallel* that means horizontal homogeneity: the medium is assumed to consist of L adjacent homogeneous layers in which the single-scattering albedo and the phase function are taken to be constant within each layer (but allowed to vary layer to layer. For example, when considering radiative transfer through stratus clouds, it would be reasonable to require homogeneous conditions over a horizontal distance about 10 times the cloud-base height (Ricchiazzi and Guatier, 1998).

- *flat earth* coordinate system, this assumption is valid when the region of interest has a vertical extent much less than the radius of earth. Dahalback and Stamnes (1991) showed this approximation provides adequate estimates of atmospheric photolyses even for solar zenith angles as large as 90° when used with a plane-parallel radiative transfer model.

The resolution of the RTE is obtaining in two parts. At first the phase function p (in 2.34) is expanded in a series of 2N Legendre polynomials and the intensity I in a Fourier cosine series. By replacing these terms in the equation 2.34 we obtain 2N Independence equations one for each Fourier component. The second phase consist of transforming this new equation in a discrete ordinate approximation that replaces the integral with a summery. In order to solve analytically the last discrete equation the plane parallel approximation is necessary (for more detail Stamnes et al. (1988)).

2.4 Scattering geometry and bidirectional reflectance

When scattering processes are dominants (i.e. VIS-NIR wavelenghts) the reflection process is described by using a scattering geometry and by defining a new variable.

In reference to fig. 2.6 the sun radiation (denoted as I^{SUN}) reflected from a position-vector ($\vec{s}$) on the earth and the atmosphere is detected by a satellite sensor (denoted as I^{SAT}). The sun-pixel-satellite tridimensional geometry is specified by the $\hat{\mathbf{\Omega}} \downarrow$ and $\hat{\mathbf{\Omega}} \uparrow$ directions; equivalently, the sun zenith angle θ^{SUN} (or $\theta_{\odot}$), the satellite zenith angle θ^{SAT} (or θ) and the azimuth angle $\Delta\phi$ completely describe the scattering geometry.

For a fixed geometry, the scattering properties of a position-vector are

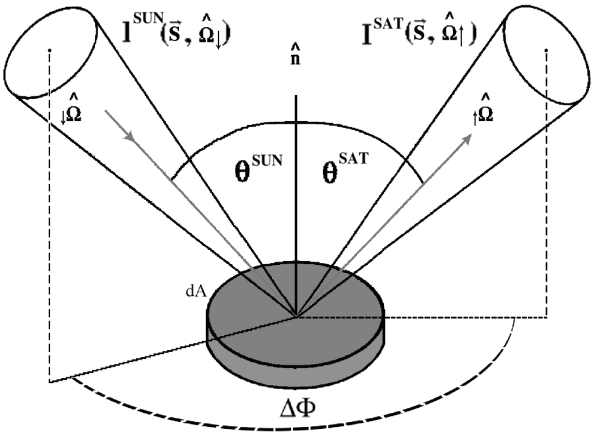

Figure 2.6: Bidirectional reflection functions geometry.

described in terms of Bidirectional Reflection Distribution function (BRDF) or bidirectional reflectance R_ν (or R_λ if it is expressed as function of λ). Considering an incoming radiation I_ν from a generic direction $\hat{\Omega}$ and the incremental radiance fraction reflected into the direction $\hat{\Omega}'$(see Fig. 2.6)

$$\rho(\hat{\Omega}', \hat{\Omega}) \equiv \frac{dI_\nu^{\uparrow}(\hat{\Omega})}{I_\nu^{\downarrow}(\hat{\Omega}')\; cos\theta' d\Omega'} \tag{2.35}$$

If the incoming radiation is collimated along the direction of the sun $\hat{\Omega}_\odot$, which is common in most remote sensing applications at VIS-NIR spectrum bands, the reflection function can be rewritten:

$$R(\hat{\Omega}_\odot, \hat{\Omega}_v) = \frac{\pi\; I_\nu^{\uparrow}(\hat{\Omega})}{F_\nu^{\odot}\; cos\theta_\odot} \tag{2.36}$$

where $I_\nu^{\uparrow}(\hat{\Omega})$ is the measured spectral radiance (namely, in the remote sensing application, arriving to the satellite sensor with $\hat{\Omega}_v$ angle of viewing), $\hat{\Omega}_\odot$ is the angle of viewing of the sun and thus $F_\nu^{\odot}\; cos\theta_\odot$ is the solar incident flux (θ is the sun zenith angle); at these wavelength this is the only significant incident radiation. Note that the π factor represents a common and conventional way to express the reflectance function in cloud remote sensing.

Reflectance is an important variable for cloud analysis, since it generally depends on the composition (via the refraction index, m) and the vertical profile of the particle size distribution of the cloud droplets, $n(r)$, so that it is crucial to infer many of the cloud parameters show in the next section. Therefore the outgoing $I_\nu^\uparrow(\hat{\Omega})$ can be expressed as:

$$I_\nu^\uparrow(\hat{\Omega}_\nu) = I_{refl}^{cloud\,top}(\hat{\Omega}_\odot, \hat{\Omega}_\nu) = R_\nu(\hat{\Omega}_\odot, \hat{\Omega}_\nu, m_\nu, n(r))\, I_\nu^\downarrow(\hat{\Omega}_\odot) \tag{2.37}$$

where $I_\nu^\uparrow(\hat{\Omega}_\nu)$ is the incident solar radiation, while $I_{refl}^{cloudtop}$ is the radiance reflected by the top cloud, since at VIS-NIR-IR region of the spectrum the only part of the thick cloud affecting the emission-reflection processes is its top (Kidder and Vonder-Haar, 1995).

The refraction index is a characteristic of the medium considered and it depends upon the wavelength. In solving the Maxwell equations in complex form, the refraction is conveniently expressed as being composed of a real part n and an imaginary part κ, thus: $m = n + i\kappa$. The real part n determines the phase speed $v = \omega\lambda_0/(2\pi n) = c/n$, while the imaginary part κ determines the wave attenuation during the propagation into the medium.

The cloud particles are water in a liquid or ice phase and figure 2.7 show the variability of the ice/water refraction index components varying the wavelength in the VIS/IR band. Considering the imaginary part, shown in the right side of the Fig. 2.7, in the VIS region (λ lower than 1 μm) water and ice show very low absorption, thus the electromagnetic field is not attenuated (conservative scattering). Whereas moving towards the higher wavelength, κ increases and the absorption progressively becomes more significant.

Another interesting observation is that water and ice have significant differences in κ around 1.6 μm and 3.7 μm. Therefore, these channels are particularly useful for distinguishing between water and ice clouds.

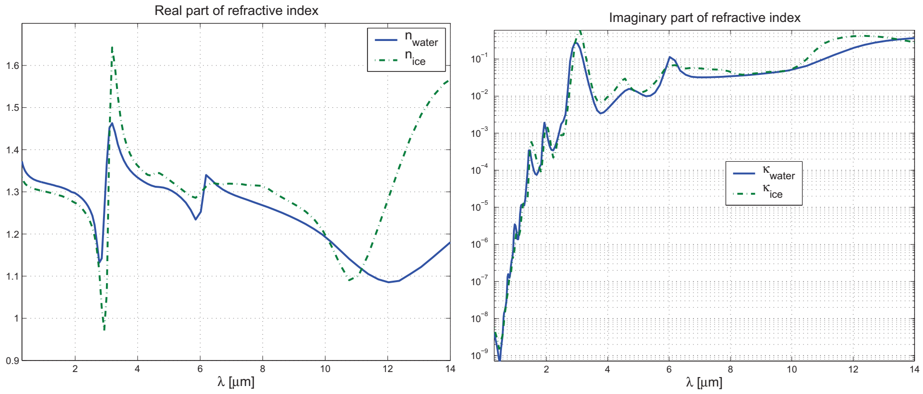

Figure 2.7: Water and ice refraction index for VIS/IR radiation

Finally, when both scattering and absorbing region are taken into account (e.g. for the 3.9μm channel), the measured radiance $I_\nu^{\uparrow}(\hat{\Omega}_\nu)$ of 2.37 becomes:

$$I_\nu^{\uparrow}(\hat{\Omega}_\nu) = I_{refl}^{cloud\,top}(\hat{\Omega}_\odot, \hat{\Omega}_\nu) + I_{emiss}^{cloud\,top}(\hat{\Omega}_\nu) = R_\nu(\hat{\Omega}_\odot, \hat{\Omega}_\nu, m_\nu, n(r)) I_\nu^{\downarrow}(\hat{\Omega}_\odot)_\nu + B(T)\varepsilon \tag{2.38}$$

where ε is the cloud emissivity. This, considering the Planck function B_ν and the solar incident flux $F_\nu^{\odot}\, cos\theta_\odot$, can be also written as:

$$I_\nu^{\uparrow} = (1 - R_\nu)\, B_\nu(T_{cloud\,top}) \;+\; \frac{F_\nu^{\odot}\, cos\theta_\odot}{\pi}\, R_\nu \tag{2.39}$$

The cloud-top temperature $T_{cloud\,top}$ can be obtained from the radiance measured by sensor at 11.03μm.

Considering the equation 2.39, the 2.36 take the form:

$$R_\nu = \frac{1 - B_\nu(T_{cloud\,top})}{\pi^{-1}(F_\nu^{\odot}\, cos\theta_\odot) \;-\; B_\nu(T_{cloud\,top})} \tag{2.40}$$

Further we have to specify that in 2.39, **??**, 2.40 the transmission functions t_ν (that in a more general form have to be multiplied by all the radiances considered) have been omitted, because it is assumed that their values are close to 1 at these wavelengths. Equations 2.36 and 2.40 are used to infer cloud parameters at different spectral bands.

2.5 Cloud parameters retrieval

Many cloud properties are of interest to the meteorologist. The main parameters retrieved by using images at VIS,NIR, IR are: cloud top temperature, cloud top height (or pressure), reflectance, optical thickness, phase (ice or water), liquid water content. Some of these parameter, such as cloud top temperature and reflectance, have been presented in previous sections, the rest will be described in this section.

2.5.1 Cloud optical thickness and cloud particles effective radius

As shown in equation 2.37, the bidirectional reflectance of a cloud generally depends on the composition (affecting the refraction index m_ν) and vertical profile of the particle size distribution, $n(r)$, of cloud particles. Instead of working with the very complicated particle size distribution profile (in this case the inversion problem is ill-posed, because the variables to be retrieved are far more than the measured quantities), it is better to use integrated scalar quantities, which provide a rougher description of the cloud but can be retrieved from the measured reflected radiances.

The first integrated quantity typically used is the cloud optical thickness, defined as:

$$\tau \equiv \int_0^{z_{cloud}} k_{\lambda,ext}(z)dz \qquad (2.41)$$

On the other hand, when the imaginary part of the refraction index is not negligible, the reflectance of the cloud depends on the effective radius as well. This quantity is defined as:

$$re = \frac{\int_0^\infty r^3\, n(r)\, dr}{\int_0^\infty r^2\, n(r)\, dr} \tag{2.42}$$

where $n(r)$ is the particle size distribution and r the particles radius. The numerator of the 2.42 is tightly related to the Liquid Water Content (LWC), since it can be written:

$$LWC = \frac{4\pi\rho_L}{3} \int_0^\infty r^3\, n(r)\, dr \tag{2.43}$$

where ρ_L is the density of water.

For wavelengths in the visible and typical cloud particles size, the optical regime is valid and we can consider the extinction paradox (i.e. extinction cross sections are equal to twice the particle areas). Thus, we can related the optical thickness to LWC and droplet size by using this formula:

$$\tau \approx \int_{\Delta z} \frac{3}{2\rho_L} \frac{LWC}{r_e} dz \approx \frac{3}{2\rho_L} \frac{\overline{LWC}}{\overline{Re}} \Delta z \tag{2.44}$$

Where $\overline{Re}$ and $\overline{LWC}$ are, respectively, the mean effective radius and the mean LWC along the Δz cloud vertical thickness. By considering two clouds having the same LWC: the cloud that contains a smaller droplet would have a larger optical thickness and therefore would reflect more sunlight.

The liquid water content of clouds varies greatly from cloud to cloud and the following characteristic values may be used (Pruppacher and Klett, 1997): cumulus (early stage), 0.2 to 0.5 g/m^3; cumulus (later stage), 0.5 to 1.0 g/m^3; dense cumulus congestus and cumulonimbus, 0.5 to 3.0 g/m^3; alto-cumulus-alto-stratus, 0.2 to 0.5 g/m^3; stratus-stratuscumulus, 0.1 to 0.5 g/m^3; nimbo-stratus, 0.2 to 0.5 g/m^3.

The optical thickness (eq. 2.41) accounts for how much radiance interacts with the cloud (Nakajima and King, 1990). When scattering is the only relevant process (i.e. at 0.6, 0.8 μm), it is the only parameter affecting the reflectance of a cloud, so that is possible to rewrite 2.37 in case of conservative scattering as:

$$I_\nu^{\uparrow}(\hat{\Omega}_\nu) = R_\nu(\tau)\, I_\nu^{\downarrow}(\hat{\Omega}_\odot) \tag{2.45}$$

The particles effective radius, (introduced by Hansen and Travis, 1974) is a balance between the numerators volumetric trend ($\propto r^3$, as the absorption process) and denominators superficial trend ($\propto r^2$, as the scattering phenomenon). It starts to be involved in the processes when the imaginary part of the refraction index increases (NIR region, e.g. 1.6 and 3.9 μm) and thus the absorption grows; in this case the 2.45 is given by:

$$I_\nu^{\uparrow}(\hat{\Omega}_\nu) = R_\nu(\tau, re(z_{top}))\, I_\nu^{\downarrow}(\hat{\Omega}_\odot) \tag{2.46}$$

The physical principle on which multi-spectral retrieval algorithms are based is the fact that the reflection function of clouds at a non-absorbing band (visible wavelengths) is primarily a function of the cloud optical thickness, while the reflection function at a water or ice absorbing band (near infrared wavelengths) is primarily a function of cloud particle size. A combination of visible and near-infrared absorbing bands therefore provides information on both optical thickness and effective radius.

Moreover, the variation of the relative magnitude of real and imaginary parts of the reflection index of water and ice along the VIS-IR spectrum, allows an estimation of the cloud top particle phase.

Retrieval methods for cloud optical thickness and effective radius

In order to retrieve the cloud optical thickness and effective particle radius, a radiative transfer model is first used to compute the reflected intensity field. Then the determination of τ and re from spectral reflectance measurements constitutes the inverse problem, that is: "*assigned* $I_\nu^{\downarrow}$ *and observation geometry estimating the cloud property (*τ *and* re*), from the measured*

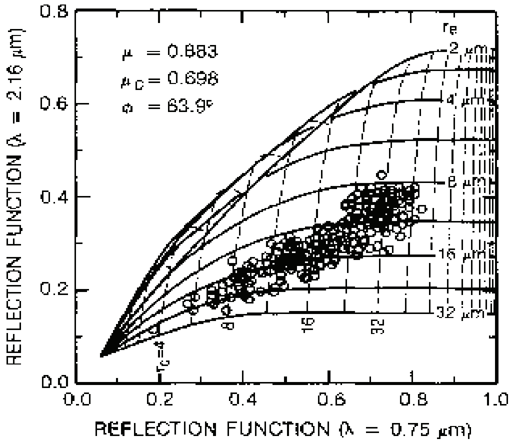

Figure 2.8: Reflection function at VIS and 2.16 μm (from Nakajima and King, 1990).

$I_{\nu}^{measured}$". This problem is typically solved by comparing the measured reflectances with entries in a look-up table of simulated reflection functions generated by different τ and re combinations. This retrieval scheme will be more extensively described in chapter 4.

Many efforts in the past three decades (early work by Arking, 1964) have been devoted to extracting cloud parameters, either by means of aircraft (Hansen and Pollack, 1970; King, 1987) or satellites (Curran and Wu, 1982; Durkee, 1989).

Nakajima and King (1990) retrieved τ and re using pairs of bands of the MODIS sensor: an appropriate optical thickness-sensitive band, together with an appropriate near-infrared band (e.g., VIS and 1.64 μm , VIS and 2.16 μm, and VIS and 3.75 μm, reflected part). In particular they considered for stratiform thick cloud layers the VIS-2.16 μm combination, whereas for optically thin layers, the addition of the wavelength 3.7 μm allows to reduce resulting ambiguous solutions in the re values inferences.

Figure 2.8 shows R_{λ} at VIS versus R_{λ} at NIR part of the spectrum (2.16 μm) for different cloud optical thickness and particle sizes. It also highlights that τ is largely determined by the R_λ at 0.75 μm , while, the NIR R_λ is very sensitive to re values. Further, the small particles with re around 2 μm present the biggest reflection capability , whereas the smallest R_λ values are due to big droplets (around 30 μm) that provide a greater absorption capability, excluding the very low R_λ values, corresponding to the smallest τ values (left-bottom corner).

The window bands around 4 μm are between bands where solar radiation is scattered (VIS and NIR windows bands) and bands where the emission-absorption processes are dominant (IR window bands). At 4 μm the radiation measured is composed by scattered sun radiation and emitted radiation: these two terms are comparable. Figure 2.9 shows that this wavelength is located in the region where sun and Earth Planck emission functions is overlap.

The utility of the 3.7 μm band on board the AVHRR has been demonstrated by several works (Arking and Childs, 1985; Platnick and Twomey, 1994; Platnick and Valero, 1995). The use of the 3.75 μm band complicates the retrieval algorithms because radiation emitted by the cloud is comparable to, and often dominates, the solar reflectance and to correct for thermal emission in the 3.75 μm band, the total upward reflection function at the top of the atmosphere has to be decomposed into solar, thermal, and surface contributions (Platnick and Valero, 1995; Nakajima and Nakajima, 1995).

Figure 2.10 displays the different behaviour of R_λ as a function of τ calculated at VIS wavelength and for different particle sizes, at 0.65, 1.6, 2.1 and 3.7 μm bands; again the VIS capability to infer τ , while the NIR capability to infer re is clearly highlighted.

The main objective of the work of King et al. (1997) was the development of routine and operational methods for simultaneously retrieving re and τ from daytime multiwavelength reflected solar and emitted thermal radiation measurements for plane-parallel liquid water clouds. This method requires a previous knowledge of cloud particle phase and cloud cover as inputs for the

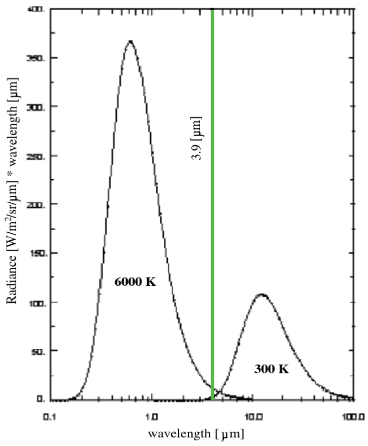

Figure 2.9: The Planck emission function for approximately Sun (6000 K) and Earth temperatures (300 K) with emission for both shown at 3.9 μm.

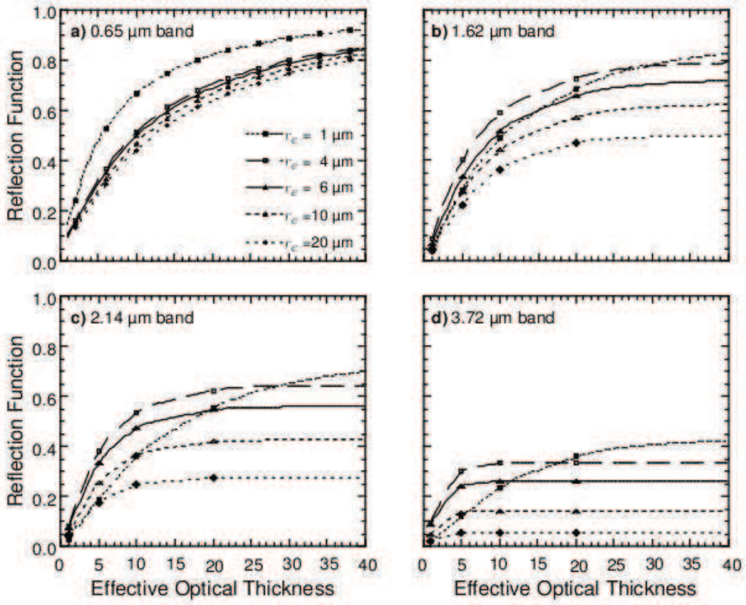

Figure 2.10: Reflection function as a function of τ at VIS wavelength and for different particles sizes, at 0.65, 1.6, 2.1 and 3.7 μmbands (from King et al., 1997)

$re - \tau$ retrieval. Cloud cover has been provided by the cloud top properties algorithm of Menzel and Strabala (1997) based on analysis of the cloud mask algorithm of Ackerman et al. (1998). The algorithm for cloud particle phase, using emitted thermal radiation measurements, has also been developed by Menzel and Strabala (1997), as will be explained next section.

Each near-infrared band is sensitive to the re at a different depths within the cloud: the 3.75 μm retrieval is the most sensitive to drops high in the cloud while the 1.64 μm much lower in the cloud. Chang and Li (2002) proposed a multispectral near-infrared technique applied to the MODIS data to estimate the vertical profile of re for stratiform water clouds using multispectral near-infrared (NIR) measurements. The basic idea of the retrieval technique is that radiance measurements at distinct multi-NIR wavelengths have different penetration depths inside the cloud and this conveys, at given geometrical conditions, information on the re vertical profile.

One of the relevant applications of effective radius estimates is related to its crucial capability to be used as an indicator of precipitation ($re > 14\mu m$), because an effective radius of 14 μm has been noted to be a threshold value above which clouds contain precipitation size particles that can be detected by meteorological radars (Rosenfeld and Gutman, 1994). Those authors justified this relationship assuming that if cloud top particles reach such value of re, the coalescence process (when cloud droplets growing by merging two or more droplets) start to take place and thus precipitation-sized particles are likely to be produced by the cloud.

A suitable methodology to infer re from NIR wavelengths was established by considering the 3.7 μm channel from the NOAA Advanced Very High Resolution Radiometer (AVHRR) by Rosenfeld and Lensky (1998). The aim was to follow the re evolution in continental (composed by many small droplets) and maritime (with small concentration of larger droplets) convective cloud particles versus the cloud-top temperature (T), used as a height indicator, and to infer from that information about the cloud microphysical structure and the precipitation forming processes. The R_λ calculated at 3.7 μm (defined in 2.40), was used to infer the re value, taking into account only fully cloudy pixels and thick enough to be potential precipitation procedures. Moreover, if in a satellite scene various convective clouds at different development stages are present, it is assumed (following Arakawa and Schubert (1974)) the so called ergodic hypothesis . The cloud top of different clouds at different stages may be assumed as representative of the structure of a single cloud as it grows through the various heights and that re is a conserved property for a given temperature, as long as precipitation has not developed.

From cloud base to top, the microphysical classification includes zones of diffusional droplet growth (by vapour diffusion), coalescence droplet growth (much faster), rainout (where the coalesce growth is balanced by the precipitation fall), mixed-phase precipitation (occurred at $T < 0°C$), and glaciation (with re nearly stable), due to the particular cloud system under observation since not all processes appear in a single cloud system. Application to maritime clouds shows, from base to top, zones of coalescence, rainout, a shallow mixed- phase region, and glaciation starting at $-10°C$ or even warmer. In contrast, continental clouds have a deep diffusional growth zone above their bases, followed by coalescence and mixed- phase zones, and glaciation at $-15°C$ to $-20°C$. Highly continental clouds have a narrow or no coalescence zone, a deep mixed-phase zone, and glaciation occurring between $-20°C$ and $-30°C$. An example of T versus re for a maritime cloud is shown if fig. 2.11.

2.5.2 Cloud particles phase and Cloud top height

To distinguish between ice and water cloud phases, spectral region presenting remarkable differences in terms of refraction index has to be chosen. These wavelengths may belong to the NIR or IR part of the spectrum (Platnick et al., 2003) and in Fig. 2.7 the importance of the 1.6 wavelength for

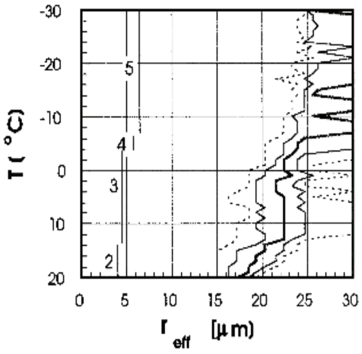

Figure 2.11: Temperature-effective radius relationship for a maritime cloud (from Rosenfeld and Lensky, 1998).

phase discrimination has been already anticipated.

The differences in reflected solar radiation between the 0.65 and 1.64 mum bands contain information regarding cloud particle phase due to distinct differences in bulk absorption characteristics between water and ice at the longer wavelength. The visible reflectance, suffering no appreciable absorption for either ice or liquid water, is relatively unaffected by thermodynamic phase. However, if the cloud is composed of ice, or if the background surface is covered by snow (similar in effect to large ice particles), then the reflectance of the cloud at 1.64 μm will be smaller than for an otherwise identical liquid water cloud. The 2.13 μm band is expected to show a significant decrease in reflectance as well, but this is somewhat less dramatic than the reduced reflectance at 1.64 μm. Demonstrations of the application of this method to the problem of distinguishing the thermodynamic phase of clouds can be found in Hansen and Pollack (1970), Curran and Wu (1982).

Other crucial bands for the phase retrieval belong to the thermal region, such as the 8.6, 11, 12 μm etc., that can be used for cloud cover and cloud top properties, including cloud top altitude, cloud top temperature and thermodynamic phase (Ackerman et al., 1998; Menzel and Strabala, 1997). This

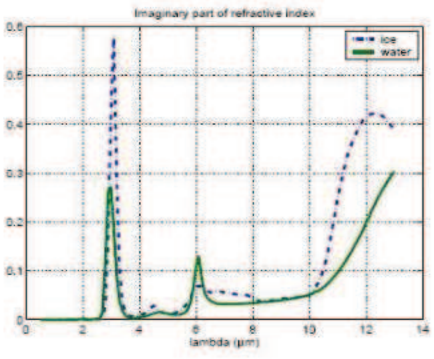

Figure 2.12: Imaginary part of the refraction index in VIS-NIR-IR part of the spectrum.

cloud particle phase algorithm works on infrared wavelengths and is based on the fact that the magnitudes of the imaginary part of the refraction index for ice and water are nearly equal between 8.5 and 10 μm but diverge between 10 and 13 μm (see Fig. 2.12.

Differences in the values of the refraction index for water versus ice will result in distinctive reactions to similar incident radiation. If water and ice clouds were to have the same temperature (i.e., same altitude), and have similar microphysical size and shape distributions, the 8.5μm cloud radiance would not depend greatly on thermodynamic phase. However, one might expect differences in the measured radiances between the ice and water cloud at 11μm and 12μm as ice has greater values of the imaginary part of the refraction index than water.

Strabala et al. (1994) demonstrated that radiances of ice clouds and water clouds tend to separate when brightness temperature differences (TD) between 8.5μm and 11μm ($TD[8.5-11]$) and 11μm and 12μm ($TD[11-12]$) are compared. Ice clouds tend to have greater values of $TD[8.5-11]$ than $TD[11-12]$ whereas water clouds tend to have greater $TD[11-12]$ than $TD[8.5-11]$ values (Fig. 2.13).

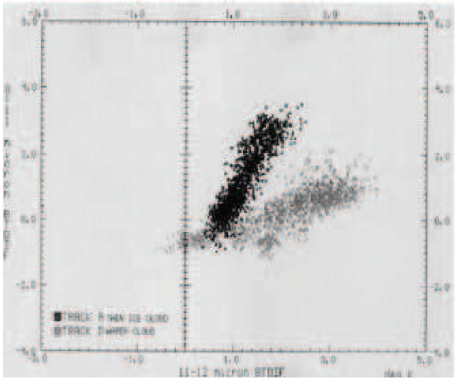

Figure 2.13: Scatter diagram of averaged TD[8.5-11] (on x axis) and TD[11-12] (on y axis) for ice (black dots) and water (grey dots). clouds (from Strabala et al., 1994).

Chapter 3

Cloud Mask using SEVIRI data

Cloud cover analysis involves different fields of application in climatology and meteorology. Besides that, a number of geophysical parameters can only be derived for satellite in cloud free conditions: algorithms for the retrieval of sea and land surface characteristics, aerosols contents, vertical temperature profiles, atmospheric gases and water vapour concentrations are designed to work minimizing cloud contamination.

Several satellite measurements usually provide different cloud products. Given the need of such cloud screening, the cloud mask is an operational product provided by a large number of satellite. The "cloud mask" consist of classification of pixel as *clear* or *cloudy* and in some case a confidence index is associated to these classes.

At the beginning of this chapter the current cloud mask methods will be reviewed. Then the cloud mask algorithm developed for SEVIRI will be introduced describing the preliminary studies and the algorithm structure. Finally, the derived cloud mask has been compared with the MODIS operational product with validation purposes.

3.1 Cloud mask methods

Clouds mask algorithms are based on different principles which depend on the spectral information and detection strategies. Methods that used only IR and VIS bands are essentially based on the following principles:

- clouds reflect more in visible than the earth surfaces;
- clouds have temperature relatively lower than earth surfaces;
- clouds reflectivity and temperature have higher spatial and temporal variability than the earth surface.

These are three rules of thumbs that summarize the main cloud radiative properties. This approach is not simple to apply mainly because of the several limitations and exceptions to these rules. The reduced cloud-surface contrast is the main problem to cope with, in particular in cases of:.

- *low clouds*
- *thin clouds*
- *sub-pixel structures*
- *clouds on ice/snow surface*

In case of *low clouds* the radiation that reaches the sensor mainly comes from the top of the cloud: only 10% for $\tau = 5$ comes from lower levels (Rossow and Shiffer, 1999). The transmittance is depending on the hydrometeors dimensional distribution. The cloud top is distinct in the optical thickness increases from zero to a moderately large value over a very small vertical extent (say 30-100m; see Minnis et al., 1992). A global annual mean of low-cloud optical thickness is about 5.3 and low cloud top temperature is about $280.5K$ (Rossow and Shiffer, 1999). Considering these characteristics (high temperature, small vertical extent, moderate optical thickness) clouds that are low in the atmosphere are often difficult to detect. The thermal contrast between clear sky and low cloud is small and sometimes undetectable by infrared techniques. Thus reflectance techniques can be applied during daylight hours to improve the detection of low clouds.

In case of *sub-pixel structures* the radiation that reach the sensor can be estimated by this formula $R_\lambda = (1 - \eta)B_\lambda(T_s) + \eta B_\lambda(T_c)$ where η is the pixel fraction covered by cloud, λ is the central wavelength band of the sensor and Tc and Ts are respectively the temperature of the top of the cloud and the temperature of the ground surface. Figure 3.1 shows the brightness temperature correspondent to $R_{10.8}$ which has been computed for Tc between 200-300K, η between 0-1, and Ts is 300K. Figure 3.1 shows also the ambiguous meaning of cloudy pixel temperature when the dimension of cloud is smaller than the instrument spatial resolution, this is the case, as example of small cumulus congestus or the edges of large clouds (partially covered pixel). A 10K temperature decrease we have two cases: they are produced 1) by a low cloud with a top at 265K that covers 30% of pixel, 2) by an high cloud with a top at 220K that covers 15%.

Problems related to broken clouds have not already received adequate treatment in satellite meteorology (Kidder and Vonder-Haar, 1995). Because broken clouds radiatively interact with each other, and because the nonnadir viewing sees the sides as well as the tops of the clouds, effective cloud amount in broken cloud fields is not necessarily proportional to the fractional area covered with clouds (Wienman and Harshvardhan, 1982).

Thin clouds, like cirrus, are characterized by low optical thickness, due to their low ice content. In this case the radiation that reaches the sensor comes from levels below cloud and it is nearly transmitted by cloud.

A rough count obtained using CO_2 slicing method (Wylie and Menzel, 1999) can give an idea of the problems in detecting cirrus in window IR

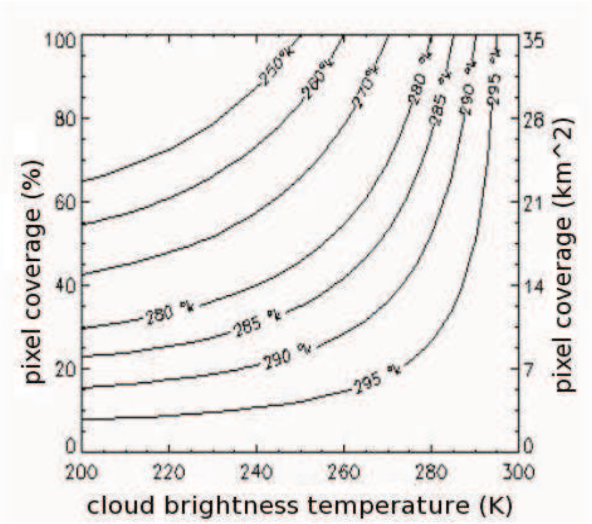

Figure 3.1: Brightness temperature at 10.8μm varying the top of cloud and the coverage fraction. The temperature of ground surface is 300K.(Dalla Libera, 2002)

channels. Since the instrument used (HIRS) has a field of view (FOV) of 20 Km, in most of case the pixels are partially cover thus the effective emissivity values, that is the emissivity (ϵ) produced by the cloud fraction of pixel have been estimated. The effective emissivity of clouds above 6km ranges from 0.2 to 0.6 with an average value of about 0.5. This results con be translated in brightness temperature. Considering a surface temperature of 280 K and a temperature of 250K for a cloud heights 6 km (about 450hPa at mid latitude). The temperature retrieved by sensor is 266 K for 0.5 of effective emissivity and 274 K for 0.2 of effective emissivity. In the worse case only 6 K cooler than clear sky case. This .

Snow and ice surface are difficult to distinguish from clouds because their low brightness temperature and high reflectivity are similar to cloud ones. Thus visible and infrared bands often fail on these surface because of the small visible and thermal contrast between clouds and surface. Moreover the thermal structure of troposphere on ice can be characterised by isothermal inversion layers. Information from the near-infrared bands is used in this case. NIR bands show great potential differentiating clouds from snow and ice surface (Kidder and H.-T.Wu, 1984; Yamanouchi et al., 1987) because of reflectivity of snow in NIR is lower than reflectivity of clouds.

3.1.1 Cloud mask algorithms

In order to improve cloud detection from satellite observation different methods have been proposed. Two types of cloud detection methods can be distinguished:the *statistical methods*, such as artificial neural network and pattern recognition techniques, based on the training of textural and spectral parameters; the *physical methods* consisting of multispectral threshold techniques applied to single pixels. Table 3.1 summarizes a number of published cloud mask algorithms.

Several cloud detection algorithms use statistical methods. Ebert (1987) distinguished surface from cloud type in polar regions by using an automated pattern recognition algorithm which identifies regions of various surface and cloud types at high latitudes from visible, near-infrared and infrared AVHRR satellite data. The maximum likelihood decision rule is used to classify the regions into one of seven surface categories or eleven cloud categories. The algorithm showed a skill score of 84.6% when on training imagery, and an estimated skill score of 83.0% when verified against the analyses of three experts.

Artificial Neural Network (ANN) is also employed in cloud statistical detection algorithm. Schroder et al. (2002) developed a cloud-masking technique based on supervised learning of an ANN for images measured by an airborne spectrographic imager. They trained the neural network on radiances textural features and gradient-filtered radiances demonstrating a correct classification of clouds over water surface affected by sunglint. This method shows some difficulties in detecting cloud borders and clouds with low albedo.

In many cases, ancillary data such as climatology, NWP temperatures, humidity profiles and surface land and sea temperatures are used in order to define the thresholds. For instance the fully probabilistic Bayesian approach by Merchant et al. (2005) detects cloudy pixels in thermal infrared imagery observed from polar satellite over oceans. It makes use of climatology and Numerical Weather Prediction (NWP) forecast data in order to build a-priori information.

Physical methods also make use of ancillary data. The SEVIRI cloud mask by Derrien and Gleau (2005) used a multi-spectral threshold technique for a real time cloud detection algorithm, which was included in Satellite Application Facility for supporting NoWCasting and very short range forecasting (SAFNWC). Most thresholds of this algorithm are dynamically computed from ancillary data (atlas, climatology map and NWP model forecast fields). The SAFNWC cloud mask sometimes presents a night time cloud overestimation in cloud-free conditions , whereas it shows a slight cloud underestimation in overcast conditions during both night time and twilight, due to the non-detection of low, thin and semi-transparent cloud (Derrien and Gleau, 2005). Nonetheless ancillary data are not always available in real time, and this may cause problems when it is necessary to obtain cloud detection in real time.

Several cloud detection algorithms are developed using reflectance and temperature thresholds. Ackerman et al. (1998) for MODIS cloud mask detection, combine the results of several spectral threshold tests to determine if a given pixel is clear, probably clear, uncertain or cloudy. At night time, it sometimes detects clouds over desert regions incorrectly and it indicates some false clouds over coastlines, rivers and inland lakes. EUMETSAT (2007) proposed a Meteorological Product Extraction Facility (MPEF)/MSG software package: 34 thresholds tests are applied to the twelve SEVIRI channels in order to get the cloud scene analysis (SCE) and the cloud analysis (CLA).

The scene analysis derives a cloud mask (cloud/no cloud decision) on pixel basis, while the cloud analysis derives detailed information on the cloud type.

In some cases the statistical and physical methods are combined (*hybrid method*) in order to improve or develop a cloud detection algorithm. Ricciardelli et al. (2008) by using an hybrid method developed a SEVIRI cloud mask which uses 9 sensor spectral bands. A set of thresholds discriminates cloudy from clear pixels with a confidence level, then a further temporal statistical test was applied to that pixel having low confidence. This algorithm was tested comparing it to MODIS cloud mask, MPEF-SCE and CPR 2B-GeoProf product. The comparison with MODIS showed an agreement of 91.8% for cloudy pixels. Cappelluti et al. (2005) developed a cloud mask algorithm for MODIS without defining thresholds tests determined in advanced, but with thresholds carried out from classification methods. This algorithm permits to obtain thresholds directly from the images. The algorithm is able to produce cloud masks pertinent to limited regions at the mesoscale level.

Cloud mask also can be obtained as by-product of cloud classification algorithms. These algorithms are also developed by a series of threshold tests (Saunders and Kriebel, 1987) and by statistical techniques (Baum et al., 1997; Bankert, 1994; Garand, 1987; Porcú and Levizzani, 1992).

me false clouds over coastlines, rivers and inland lakes. Cappelluti et al. (2005) developed a cloud mask algorithm for MODIS without defining thresholds tests determined in advanced, but with thresholds carried out from classification methods. This algorithm permits to obtain thresholds directly from the images. EUMETSAT (2007) proposed a Meteorological Product Extraction Facility (MPEF)/MSG software package: 34 thresholds tests are applied to the twelve SEVIRI channels in order to get the cloud scene scenes analysis (SCE) and the cloud analysis (CLA). The scenes analysis derives a cloud mask (cloud/no cloud decision) on pixel basis, while the cloud analysis derives detailed information on the cloud type. Ricciardelli et al. (2008) using combined statistical and physical methods developed a SEVIRI cloud mask. A set of dynamic thresholds discriminates cloudy from clear pixels with a confidence level, then a further temporal statistical test was applied to that pixel having low confidence. This algorithm was tested using MODIS cloud mask, MPEF-SCE and CPR 2B-GeoProf product.

`Author`	`method`	`type`	`data`	`bands`	`ancillary`
Ebert (1987)	statical	pattern recognition	sat-leo AHVRR	VIS-IR 4 bands	no
Ackerman et al. (1998)	physical	thresholds	sat-leo MODIS	VIS-NIR 20 bands	yes
Schroder et al. (2002)	statistical	ANN	airborne casi	NIR 1 band	no
Merchant et al. (2005)	statistical	Bayesan	sat-leo	thermal IR	yes
Derrien and Gleau (2005)	physical	thresholds	sat-geo SEVIRI	VIS-IR 9 bands	yes
Cappelluti et al. (2005)	hybrid	dynamic thresholds	sat-leo MODIS	VIS-IR 20 bands	no
EUMETSAT (2007)	physical	thresholds	sat-geo SEVIRI	VIS-IR 9 bands	no
Ricciardelli et al. (2008)	hybrid	thresholds and temporal statistical	sat-geo SEVIRI	VIS-IR 9 bands	no

Table 3.1: List of some cloud mask algorithms that employ data from visible to infrared bands.

3.2 TESCM Cloud mask algorithm

One of the aim of this study is to develop, implement and test a cloud mask algorithm for MSG-SEVIRI data that takes advantage of the high MSG-SEVIRI temporal resolution and does not use ancillary data. The proposed algorithm is fast in terms of computational efficiency because of low amounts of data used, and simple, in terms of algorithm structure.

This cloud mask, called TESCM (TEmporal Statistical Cloud Mask), is based on the principle that the brightness temperature (T) of a pixel, if measured every 15 minutes, varies very little during the diurnal cycle, while the brightness temperature variation is much higher when a cloud covers the pixel. In order to evaluate this variation the parameter considered during this analysis is the brightness temperature difference between given time and the previous one (15 minutes before):

$$\Delta T = T_i - T_{i-1} \tag{3.1}$$

3.2.1 ΔT sensitivity at 3.9, 8.7, 10.8 μm

Preliminary studies to test the sensitivity of the SEVIRI IR window bands (see tab. 3.2) to diurnal cycle were carried out, in particular we focused on 3.9 (channel 04), 8.7 μm (channel 07) and 10.8 μm (channel 09). The area of interest, where TESCM was applied, is the Mediterranean basin and part of Continental Europe, in particular within 30N-54N and 10W-43E. This area includes many different background types: desert, sea, vegetate, arid, thus a different analysis at channel 04, 07, 09 was carried out for each background.

The diurnal cycle influences ΔT in a narrow ranges of few degrees around zero. In addition, the variation of ΔT depends on the background. In order to evaluate this variation, different ΔT distributions (in visually selected clear sky condition), for each backgrounds and channels, are shown in figure

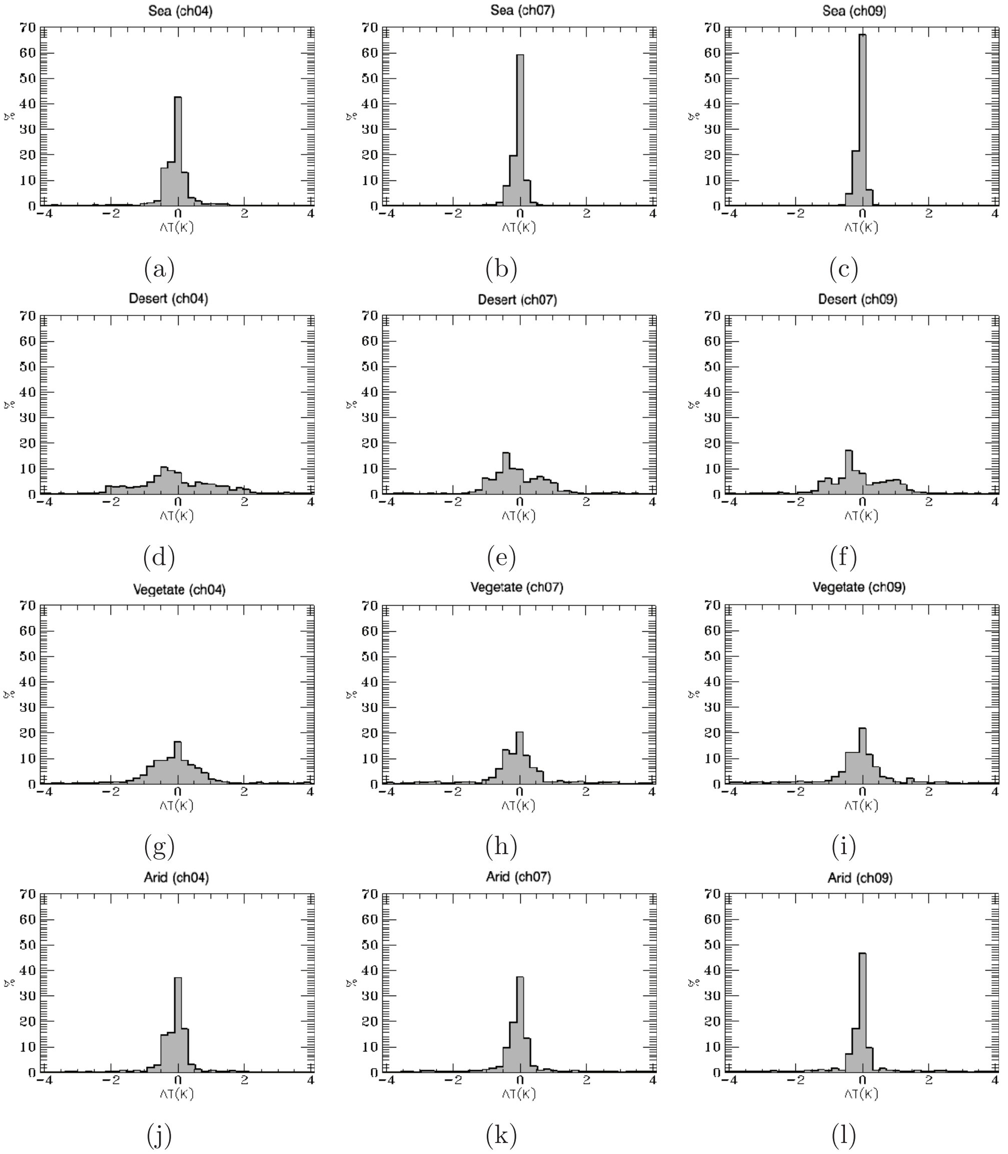

(a) (b) (c)

(d) (e) (f)

(g) (h) (i)

(j) (k) (l)

Figure 3.2: ΔT (in K) distribution for different background: sea (a,b,c), desert (d, e, f), vegetate (g, h, i), arid (j, k, l) in SEVIRI channel 04 (a, d, g, j), channel 07 (b, e, h, k) and channel 09 (c, f, i, l).

Channel	Nominal central wavelength (μm)	Nominal spectral band (μm)	Spatial resolution at nadir (km)
HRV	0.75	0.6-0.9	1
VIS 0.6	0.64	0.56-0.71	3
VIS 0.8	0.81	0.74-0.88	3
NVIS 1.6	1.6	1.50-1.78	3
NIR 3.9	3.92	3.48-4.36	3
WV 6.2	6.2	5.35-7.15	3
WV 7.3	7.3	6.85-7.85	3
IR 8.7	8.7	8.30-9.10	3
IR 9.7	9.7	9.38-9.94	3
IR 10.8	10.8	9.80-11.80	3
IR 12.0	12.0	11.00-13.00	3
IR 13.4	13.4	12.40-13.40	3

Table 3.2: Spectral channels of SEVIRI with the corresponding bandwidths and spatial resolutions.

3.2. Each distribution is referred to 4 contiguous pixels that are placed on the same background observed at channel 04, 07 and 09 for 2 days (i.e. 192 slots). Panels a, b and c are referred to sea surface: the distributions are sharply peaked around 0 K of ΔT. Desert distributions (d, e, and f in fig.3.2) are spread over a couple of degrees around 0 K peaked at -0.5 K. Vegetate and arid surfaces (g, h, i and j, k, l in fig.3.2, respectively) present distributions almost symmetric around 0 K.

One possible reason for the fact that desert ΔT distribution is peaked in the negative part is because cooling appears faster than heating if measured by IR sensors. This is true because for lower temperatures the IR channels have lower resolution due to flatter variation of radiance as function of temperature for low temperature than for high temperature (see figure 2.4). Furthermore, the distribution for channel 04 is wider than for channels 07 and 09 for all the considered backgrounds. These results are numerically summarized in table 3.3 where the standard deviation, the mean, the maximum and minimum of ΔT for each type of surface and for each channel are compared for the training period.

Some possible explanations for the main differences of ΔT distribution are:

1. the sensitivity of 3.9μm band at high temperature is higher than (see plot in figure 2.4) at channel 10.8 μm where the brightness temperature has more variability also at low temperature;
2. the emissivity varies with the backgrounds and with the wavelength, in particular deserts show a significant decrease in emissivity around 4 μm, and also around 9 μm, as it illustrated in figure 3.3, while at 10.8 μm the emissivity is close to one for all the considered surfaces.

This sensitivity analysis has shown how the distributions for channels 09 have ΔT occurrence peaks for clear sky conditions symmetrically centred at 0 K of ΔT, and the peaks are sharper than for the other two channels (04 and 07), for this reason the data relative at channel 09 have been chosen for cloud mask algorithm.

3.2.2 The algorithm

The first part of the algorithm consist of a training phase in order to obtain an initial configuration to start with. The second step classifies the clear/cloudy pixels analysing the brightness temperature difference at 10.8 μm between two instants. This algorithm does not use a fixed threshold but

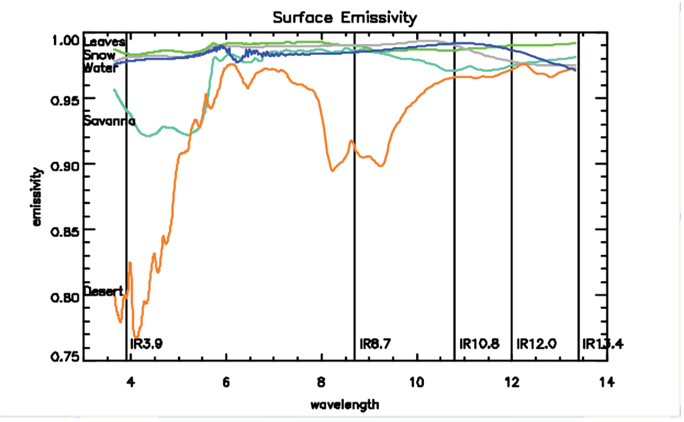

Figure 3.3: Surface emissivities (at nadir viewing) for leaves (green) snow (grey), water (blue) savanna (turquoise), and desert (tan) for wavelengths between 3.5 and 13.5 microns (Menzel, 2006).

discriminates the clear/cloudy pixels using statistics of temperature variations computed for each pixel during the diurnal cycle.

Training phase

The training consist of the analysis of data for 5 days (about 400 images) before the day the cloud mask is expected. The maximum of temperature (T_{max}) for each pixel is computed during the training period. T_{max} is assumed as the clear condition for each pixels and is the starting temperature at the instant t_0. Thus the first temperature difference (ΔT_0), at t_1, is the difference between T_1 and T_0 that is T_{max}. The T_{max} values in the area of interest are shown in figure 3.4. During the training procedure, the standard deviation (σ) of ΔT distributions for each pixel is also computed. In this scheme each pixel has is own independent statistics.

		`sea`	`desert`	`vegetate`	`arid`
ch04	$\overline{\Delta T}$	0.00	0.00	-0.04	0.00
(T±0.09)	σ	0.4	3.5	1.1	0.8
	max(ΔT)	1.63	35.31	6.35	12.11
	min(ΔT)	-4.32	-28.52	-5.91	-10.43
ch07	$\overline{\Delta T}$	0.01	-0.07	-0.03	-0.02
(T±0.05)	σ	0.2	3.8	1.7	1.6
	max(ΔT)	0.73	34.62	11.70	21.55
	min(ΔT)	-0.95	-40.06	-14.84	-19.22)
ch09	$\overline{\Delta T}$	0.01	-0.00	0.02	-0.03)
(T±0.05)	σ	0.1	4.4	1.7	1.9
	max(ΔT)	0.51	36.69	11.71	25.94
	min(ΔT)	-0.51	-40.77	-15.01	-23.67

Table 3.3: Mean, standard deviation, maximum and minimum of ΔT in K, at channels 04, 07 and 9 of SEVIRI for different backgrounds.

Structure of algorithm

TESCM algorithm is based on different tests on ΔT routinely applied every 15 minute, where the thresholds are dynamic and computed for each single pixel. In fact the standard deviation, computed in the training phase for each pixel, is applied as a sort of threshold.

This method is based on two principles which are:

- strong *cooling* effect ⟶ caused by cloud when it covers the pixel;
- strong *heating* effect ⟶ when the cloud leaves the pixel and it becomes again clear. The strength of pixel cooling and heating is evaluated by comparing the actual ΔT value with the σ stored for the given pixel.

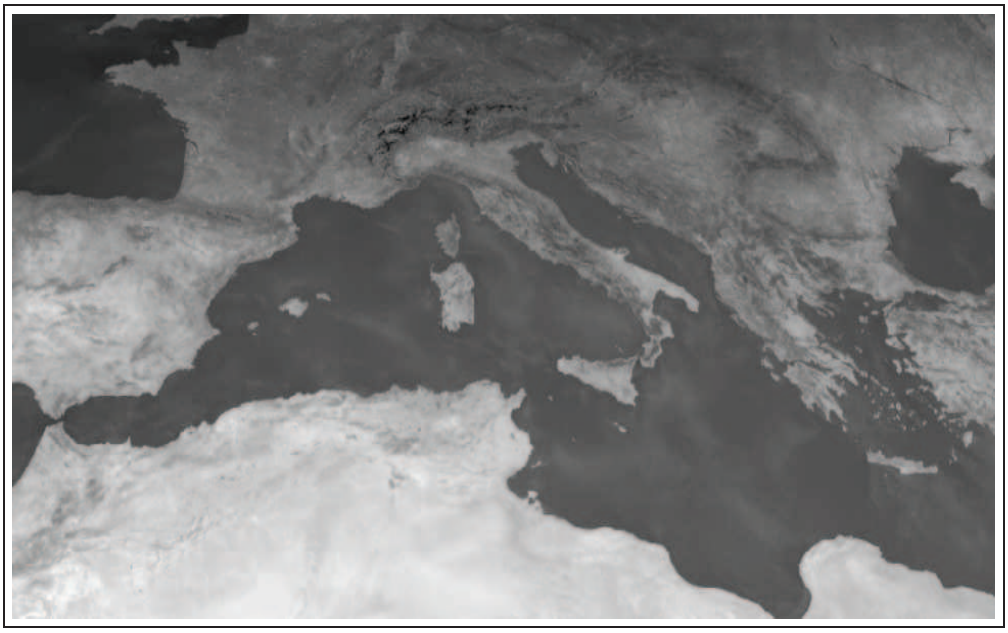

Figure 3.4: Display of the maximum of brightness temperature at 10.8 μm in the area of interest.

A schematic description of the algorithm is shown in figure 3.5. At the first instant t_1 if the σ test:

$$\Delta T_0 < -\sigma \tag{3.2}$$

is true a cloudy flag is set for the given pixel, and the clear sky temperature (T^{cs}) at the instant t_1 is stored for further tests.

At t_2 the test considers the previous status of the pixel (clear/cloudy) and applies the σ test:

- if the previous status of the pixel is clear and the sigma test is true then the cloudy flag is set;
- if the previous status of pixel is cloudy and the σ test is true (i.e. the pixel goes on cooling) then the cloudy flag is confirmed. If the σ test is false a further test on ΔT^{cs} ($\mathrm{T}^{cs} - T_i$) is applied:

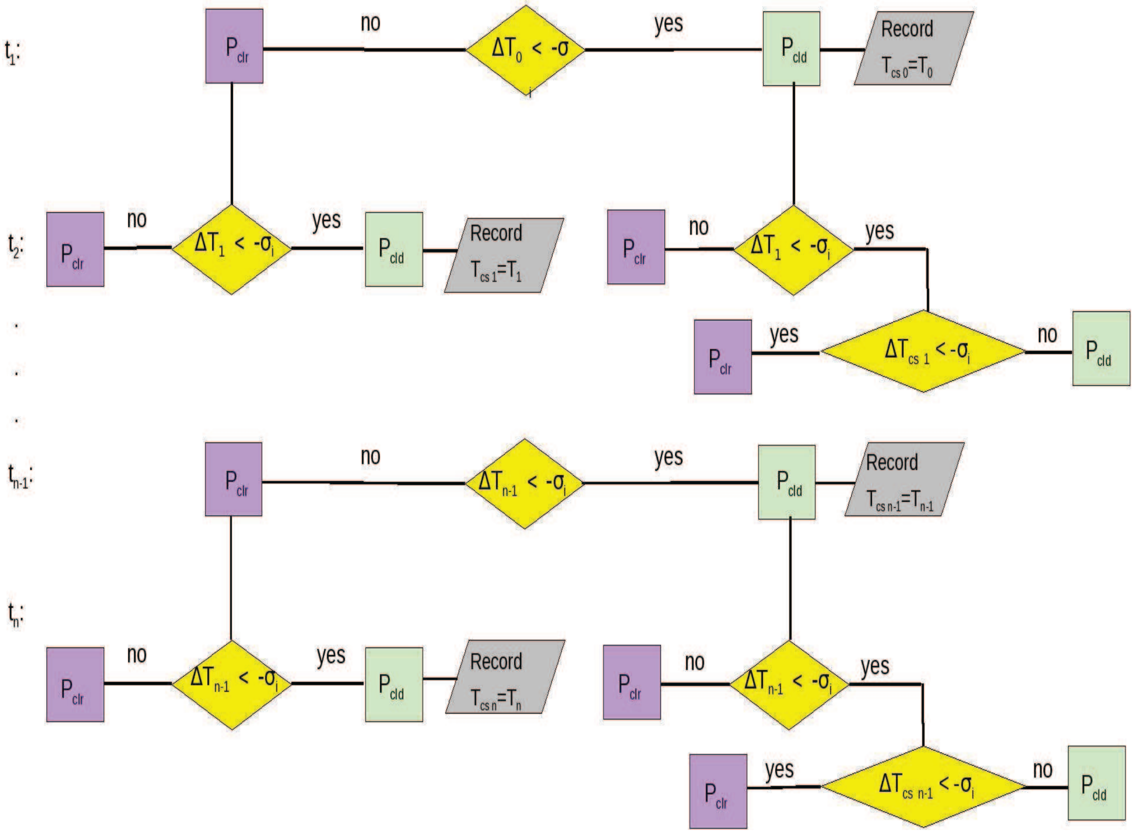

Figure 3.5: TESCM cloud mask algorithm structure.

if $$\Delta T^{cs} < \sigma$$

then the cloudy flag is removed and the pixel becomes clear. Otherwise the pixel remains cloudy.

This routine continues until t$_n$ and ΔT_{n-1} storing a cloud mask at each time.

3.3 Comparison with operational products

To asses the quality of a cloud mask is a difficult task. The validation made by another cloud mask product has to take into account of its known intrinsic deficiencies. For instance if we want to validate our cloud mask product with synoptic observations, we have to take into account the different point of view and viewing geometry, especially in case of multilayer and overlapping cloud (Henderson-Sellers et al., 1987).

On the other hand, even the comparison between two cloud mask products from different satellites is affected by the different satellite viewing geometry and by spatial and temporal resolutions. It is therefore difficult to univocally define a reference cloud cover measurement at satellite resolution, that can be assumed as a ”true” cloud fields to be used in any validation processes. We decided to consider a comparison rather than a validation and taking advantages of the comparison results to improve the cloud detection technique.

The cloud mask produced by TESCM algorithm has been compared to the MODIS cloud mask (Ackerman et al., 1998). The MODIS cloud mask is constantly upgraded and checked, and it is widely used as validation of different satellite cloud mask algorithms (Ricciardelli et al., 2008; Derrien and Gleau, 2005) thus we consider this comparison as a valuable benchmark for our algorithm. Remarking upon the results of comparison between polar-orbiter and geostationary cloud masks, it is important to consider that some disagreements are due to the differences in the time of overpass, pixel size and spectral width of the channels.

Two 15-days datasets of MSG-SEVIRI data are analysed: from 1 to 15 of April 2009, and from 1 to 15 of June 2009 for a total of 1440 items per dataset. The first 5 days per dataset have been used in the training phase (480 items). For the two dataset selected the cloud mask algorithm has been applied to the selected target area described in section 3.2.1. During these two periods and within the area 70 MODIS overpasses have been selected, in order to be compared to SEVIRI.

In this section the main features of MODIS cloud mask are described in order to underline the difference between TESCM algorithms. Finally the main results of the validation are shown.

3.3.1 MODIS cloud masks

The MODIS is an instrument belonging to EOS constellation and it measures radiances at 36 wavelengths (from 0.4 to 14.5 μm) at 250 m spatial resolution in two visible bands, 500 m resolution in five visible bands and 1000 m resolution in the infrared bands. The MODIS team uses 20 out of 36 spectral bands for cloud clearing obtaining a product at 1000 m of spatial resolution. About once a years the MODIS project collects all calibration/algorithm improvements and reprocesses the entire data stream. The resulting product are called Collections. There has been major improvements in the cloud clearing process between Collection 4 and Collection 5. The two areas of greatest improvements in Collection 5 are night time oceans and polar regions.

The MODIS cloud mask product (MOD035) is operationally archived and distributed in Hierarchical Data Format (HDF) from the NASA Goddard Distributed Active Archive Centre (DAAC). The product from NASA is disseminated in "granules", with each granule containing an image 2030

pixels along track x1354 pixels across track, equivalent to a covered area of 2030x2330 km^2.
From the web site http://daac.gsfc.nasa.gov/data/dataset/MODIS/, it is possible to order and download granules.

The product provides more information than a simple yes/no decision; there are 48 bits of output per 1-km pixel that include information on sets of multispectral test results, the processing path, and limited ancillary information such as a land/ocean tag. The first eight bits provide a summary sufficient for most applications. Additionally, the first two bits simply offer information in four categories: confident clear, probably clear, uncertain/probably cloudy, and cloudy.

The algorithm uses a variety of multispectral tests (shown in table 3.4) involving combinations of up to 19 spectral bands. Different sets of tests are applied depending on the surface (land, water, snow/ice, desert, and coast) and solar illumination (day/twilight/night). In addition to the multispectral tests, a textural test is applied over ocean to improve the detection of dust.

Several ancillary data sets are used in the cloud clearing process. Surface snow and ice data are provided by the Near Real-Time Ice and Snow Extent (NISE) product from the National snow and Ice Data Center, and the NOAA National Center for Environmental Prediction (NCEP) 0.5° resolution sea concentration product. The NCEP Reynolds blended SST product (Reynolds and Smith, 1994) has been implemented to improve the product at nighttime over oceans and in areas where there are strong temperature gradients such as in the vicinity of the Gulf Stream.

3.3.2 Results of comparison

For each MODIS granule the pixels with corresponding to scan angle greater than 40 degrees are removed. This is because with increasing scan angle the resolution of the corresponding MODIS measurement increases as

	Day ocean	Night ocean	Day land	Night land	Polar day	Polar night	Coast day	Coast night	Desert day	Desert night
T_{11}	✓	✓								
$T_{13.9}$	✓	✓	✓	✓	✓	✓	✓	✓	✓	✓
$T_{6.7}$	✓	✓	✓	✓	✓	✓	✓	✓	✓	✓
$T_{1.38}$	✓		✓		✓		✓		✓	
$T_{3.7} - T_{12}$				✓		✓				✓
$T_{8-11}\&T_{11-12}$	✓	✓	✓	✓			✓	✓	✓	✓
$T_{3.7} - T_{11}$	✓	✓	✓	✓	✓	✓	✓	✓	✓	✓
$R_{.66}$ *or* $R_{.87}$	✓		✓				✓			
$R_{.87}$ & $R_{.66}$	✓		✓							
$R_{.99}$ & $R_{.87}$	✓		✓		✓		✓			
$T_{3.7} - T_{3.9}$	✓		✓				✓		✓	

Table 3.4: MODIS cloud mask test for T (Brightness Temperature) and R (Radiances) executed ✓for a given processing path.

well. Limiting the range of scan angles it has the effect of reducing parallax errors, which are very significant in cloud when comparison with other sensors/data are involved.

The validation algorithm selects the MODIS granules that are within the MSG area of analysis for at least the half of the pixels in the MODIS image. Then it cuts the MSG area considering the MODIS boundary coordinates, in order to cover the same areas with both cloud masks. The comparison is made considering TESCM and MODIS cloud masks over the same area at nearly coincident time (time difference is at most seven minutes). The cloud fraction (CF) is computed for each clouds mask counting the total number of cloudy pixels and divided by the total number of pixels. For the MODIS cloud mask only the pixels in the class cloudy are considered for CF computation.

The CF values for MODIS and SEVIRI cloud mask and their differences

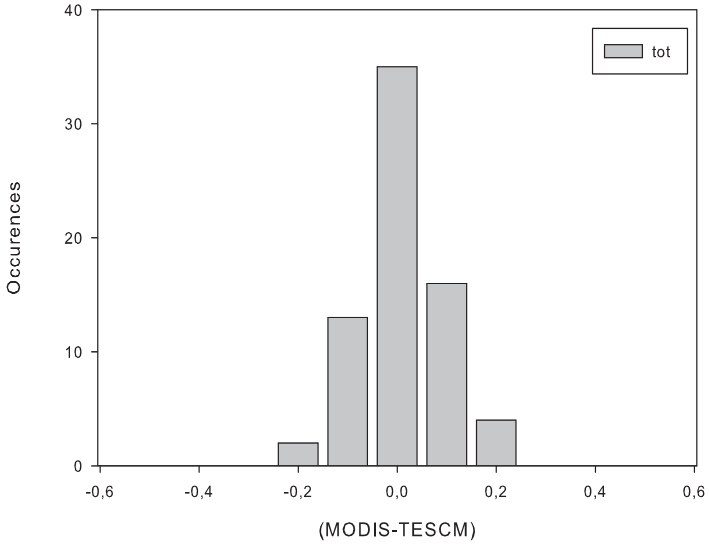

Figure 3.6: The occurrences of the difference (CF MODIS -CF TESCM).

ΔCF ($\Delta CF = CFMODIS - CFTESCM$) are shown for April dataset in table 3.5 and June dataset in table 3.6. In addition, these values are shown in histogram 3.6 where the occurrences of ΔCF are distributed in 11 classes, from -0.55 to +0.55 and each class is large 0.10. Half of the difference (35 out of 70) are peaked at interval 0.0 (within -0.05 and +0.05) and the occurrence distribution is almost symmetric around 0.0. This plot indicates that 50 % of the cloud mask couple (MODIS and TESCM) agree within 5% of error and they disagree within 25% in the worst case.

An example of a good agreement between MODIS and TESCM cloud mask is shown in 3.7. In these images it is possible to notice the different resolution and geometry of the two cloud masks (panels a and b), thus a different cut of the original images are made by validation algorithm. The right panel shows the brightness temperature at channel 9 of MSG-SEVIRI, this image is not cut by algorithm thus it displays a larger area than SEVIRI cloud mask image.

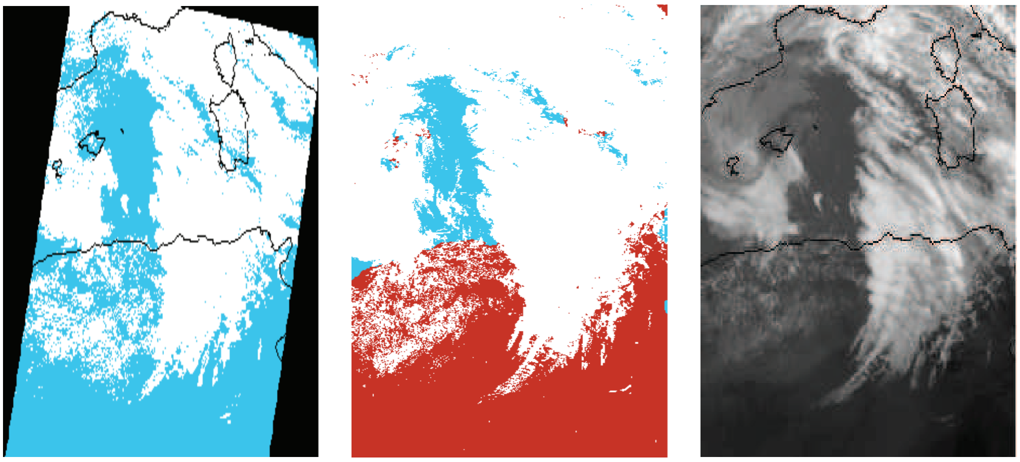

(a) *TESCM.* (b) *MODIS.* (c) *SEVIRI ch09.*

Figure 3.7: TESCM (a) on 2009-04-08 at 10:27: white is clouds and blue is land and sea. MODIS cloud mask (b) on 2009-04-08 at 10:30: white is clouds, brown is land, and blue is sea. MSG-SEVIRI (c) channel 9 brightness temperature (the highest are white pixels) on 2009-04-08 at 10:27(10.8 μm).

A larger difference ($\Delta CF = 0.245$) than the previous case is showed in 3.8, where MODIS cloud mask detects more cloudy pixels than TESCM. For instance, in the area delimited by blue dashed box, the IR show the presence of low clouds (rather high brightness temperature), and MODIS correctly delineates the cloudy pattern, while TESCM completely misses the detection. This highlights some TESCM problems in detection of low clouds or haze with warm top.

In figure 3.9, it is evident the effect of different viewing geometry of the two sensors, that prevents a pixel-by-pixel matching strategy. Anyway, in this case a good agreement($\Delta CF = -0.016$) is found between the two maps.

The analysis of (ΔCF) has been led for two different surfaces: land and sea. As a matter of fact, different performance of TESCM is expected over sea and over land, by considering the plots in fig 3.2. The CF for pixels in land and sea area are computed and the histogram of cloud fraction difference

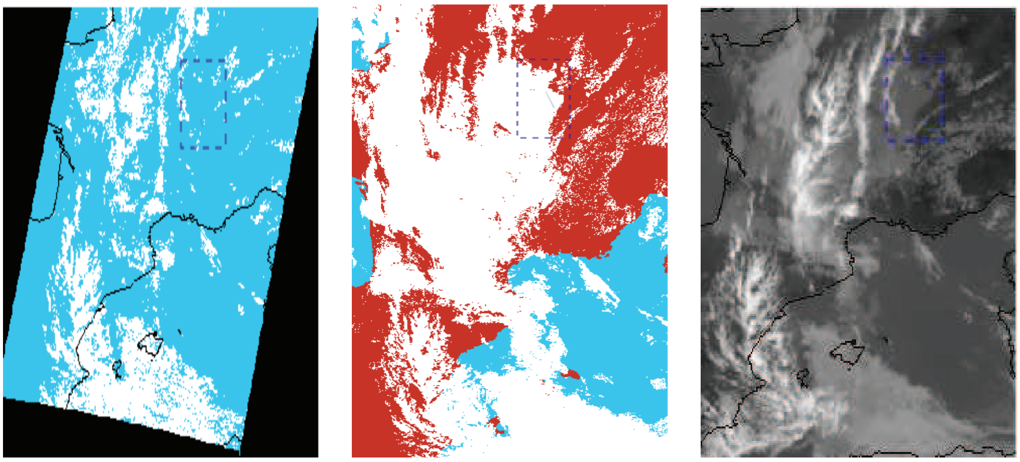

(a) *TESCM.* (b) *MODIS.* (c) *SEVIRI ch09.*

Figure 3.8: TESCM (a) on 2009-04-13 at 10:42: white is clouds and blue is land and sea. MODIS cloud mask (b) on 2009-04-13 at 10:45: white is clouds, brown is land, and blue is sea. MSG-SEVIRI channel 9 (c) on 2009-04-13 at 10:45 (10.8 μm.

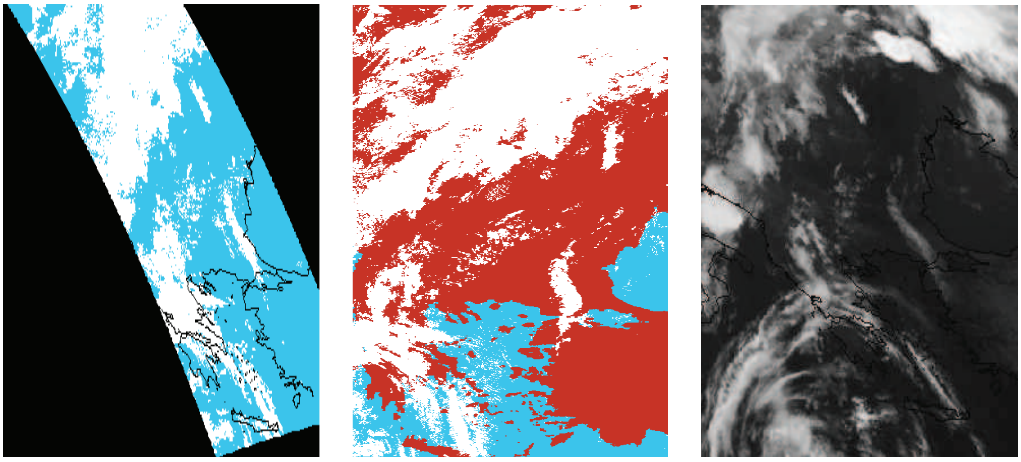

(a) *TESCM.* (b) *MODIS.* (c) *SEVIRI ch09.*

Figure 3.9: TESCM (a) on 2009-06-07 at 20:27: white is clouds and blue is land and sea. MODIS cloud mask (b) on 2009-06-13 at 20:20: white is clouds, brown is land, and blue is sea. MSG-SEVIRI channel 9 (c) on 2009-06-07 at 20:27 (10.8 μm.

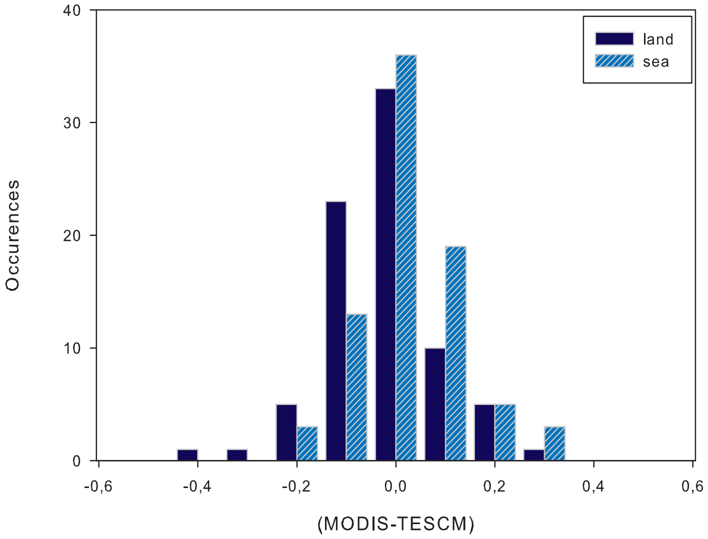

Figure 3.10: The occurrences of the difference ΔCF (CF MODIS -CF TESCM) for sea and land surface.

(ΔCF) for each surface is shown in figure 3.3.2. Over sea area more occurrences are found in the 0.0 class than over land. Moreover, the occurrences of sea pixels populate more the positive (ΔCF) classes than land pixels. This indicates that TESCM tends to underestimates cloudiness over the sea and to overestimate cloudiness over land, with respect to MODIS algorithm.

The MODIS cloud mask is obtained by using visible, near infrared and infrared bands, while TESCM uses only the infrared $10.8 \mu m$ bands. For this reasons the two cloud masks are expected to perform differently during daytime and nighttime. The histogram in figure 3.11 shows the occurrences of the difference (CF MODIS -CF TESCM) for daytime and nighttime. The daytime has more occurrences in positive differences which indicates that TESCM cloud fraction is underestimated compared to MODIS. The nighttime occurrences distribution is more symmetric than daytime, because MODIS can not use visible channels, and the two algorithms are expected to

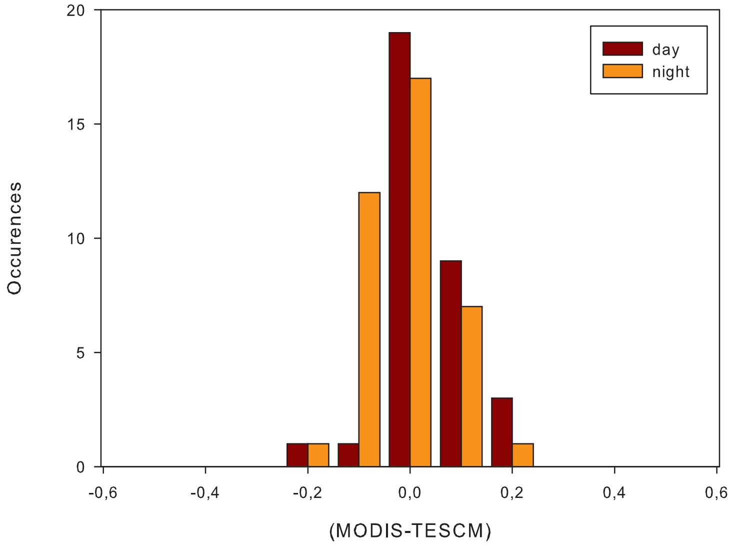

Figure 3.11: The occurrences of the difference ΔCF(CF MODIS -CF TESCM) for daytime and nighttime.

give more comparable results.

To get further hints form the comparison between MODIS and SEVIRI, cloud masks are compared for different geographical areas in our domain. In fact the different geometry of SEVIRI pixel influences the calculus of cloud fraction because the more the SEVIRI pixel is Northern and the more is large. For this reason we evaluate the comparison dividing the images that are completely below 50 latitude degrees (called South), and the others that cover the area also under 50 degrees of latitude (called North). The histogram in figure 3.12 shows the occurrences of ΔCF for North images and South images. The South occurrences have more differences at 0.0 class than North occurrences which are spread also in the other classes. These results can be attributed to problems of SEVIRI cloud mask to discriminate cloudy pixel when it covers a large area (higher number of partially covered pixels). In fact in this case the broken clouds problem is larger than in case of pixel that covers smaller area.

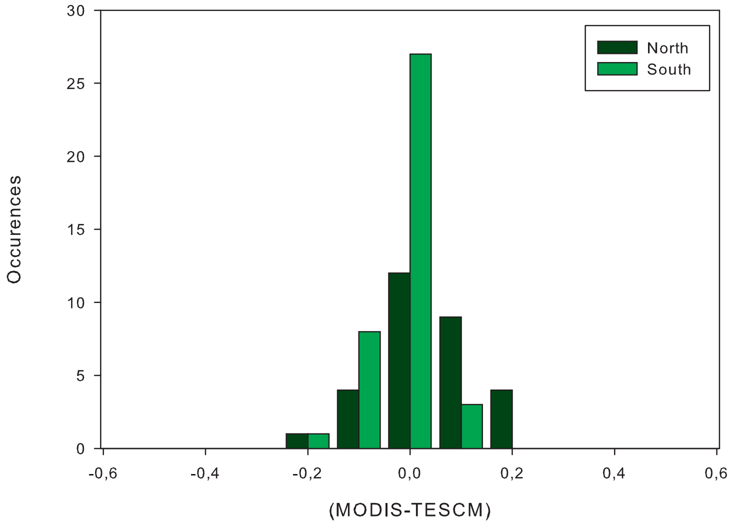

Figure 3.12: The occurrences of the difference ΔCF(CF MODIS -CF TESCM) for images completely below 50 latitude degrees (North) and that cover the area also images over 50 degrees of latitude (South).

In conclusion, the proposed SEVIRI cloud mask shows acceptable agreement (50% of case are different from MODIS within ±0.05 and at least they are in disagreement for ±0.25) compared to MODIS cloud mask for most cases. The main problems of TESCM can be attributed to the detection of low clouds, that can be caused by the absence of visible channels in the cloud mask algorithm. Consistently, the nighttime comparison shows higher agreement than the daytime. The geometry of the SEVIRI pixel also influenced the discrimination of cloudy pixel.

This comparison suggests that our approach can be a starting point for further improvement, e.g. adding a better description of the ground diurnal and seasonal thermal cycle, without increasing too much the algorithm complexity.

Table 3.5: MSG and MODIS date used for comparison for the dataset of April. The CF for the two cloud mask and the difference between MODIS CF and MSG CF.

`Date`	`MODIS hour`	`MSG hour`	`MODIS CF`	`TESCM CF`	ΔCF
2009-04-06	10:40	10:42	0.142633	0.083805	0.058829
2009-04-06	20:05	20:12	0.538739	0.646083	-0.107344
2009-04-06	21:45	21:42	0.308957	0.358765	-0.049808
2009-04-07	09:45	09:42	0.119870	0.076072	0.043798
2009-04-07	20:50	20:57	0.162415	0.162415	-0.027069
2009-04-08	10:30	10:27	0.567578	0.503242	0.064336
2009-04-09	09:35	09:42	0.415418	0.304190	0.111228
2009-04-09	11:10	11:12	0.481958	0.358274	0.123683
2009-04-09	22:15	22:12	0.459085	0.434866	0.024218
2009-04-10	10:15	11:27	0.271573	0.217424	0.054149
2009-04-10	21:20	21:27	0.377396	0.307325	0.070071
2009-04-11	11:00	10:57	0.585930	0.544513	0.041417
2009-04-11	20:25	20:27	0.345593	0.244512	0.101081
2009-04-12	10:05	11:12	0.605579	0.462313	0.143265
2009-04-12	21:10	21:12	0.592428	0.577150	0.015278
2009-04-13	10:45	10:42	0.489919	0.244926	0.244993
2009-04-14	09:50	09:57	0.367722	0.267140	0.100583
2009-04-14	20:55	20:57	0.209748	0.097472	0.112276
2009-04-15	10:35	10:42	0.313998	0.243016	0.070982
2009-04-15	21:40	21:42	0.549287	0.494033	0.055255

Table 3.6: MSG and MODIS date used for comparison for the dataset of June. The CF for the two cloud mask and the difference between MODIS CF and MSG CF

Date	MODIS hour	MSG hour	MODIS CF	TESCM CF	ΔCF
2009-06-06	11:50	11:57	0.665949	0.252582	0.413367
2009-06-06	19:35	19:42	0.100102	0.091164	0.008938
2009-06-06	21:15	21:12	0.506841	0.417703	0.089138
2009-06-06	22:50	22:42	0.132668	0.105483	0.027185
2009-06-06	22:55	22:57	0.385516	0.211124	0.174392
2009-06-07	09:15	09:12	0.191378	0.244825	-0.053447
2009-06-07	10:50	10:42	0.360979	0.279610	0.709771
2009-06-07	10:55	10:57	0.102626	0.042594	0.060032
2009-06-07	20:20	20:27	0.395258	0.410901	-0.01564
2009-06-07	21:55	21:42	0.024967	0.020080	0.004887
2009-06-07	22:00	21:57	0.623356	0.385793	0.237562
2009-06-08	09:55	09:42	0.255694	0.109707	0.145987
2009-06-08	10:00	09:57	0.008322	0.002339	0.005982
2009-06-08	11:35	11:42	0.833594	0.572481	0.261113
2009-06-08	19:25	19:27	0.291677	0.356557	-0.064881
2009-06-08	21:00	20:57	0.057611	0.080461	-0.022850
2009-06-08	21:05	21:12	0.638013	0.485677	0.152335
2009-06-08	22:40	22:42	0.381867	0.381512	0.000355
2009-06-09	09:00	08:57	0.125140	0.098995	0.026145
2009-06-09	10:40	10:42	0.480351	0.350382	0.129969
2009-06-09	20:05	20:12	0.155632	0.186893	-0.031261
2009-06-09	21:45	21:42	0.342469	0.371361	-0.028892
2009-06-10	09:45	09:42	0.181935	0.151779	0.030155
2009-06-10	11:25	11:27	0.294607	0.101640	0.192967
2009-06-10	20:50	20:57	0.183940	0.177485	0.006454
2009-06-10	22:30	22:27	0.247408	0.059781	0.187627
2009-06-11	08:50	08:57	0.044907	0.014835	0.030072
2009-06-11	10:25	10:12	0.476841	0.211160	0.265682

Table 3.6: continue in next page

Table 3.6: continue from the previews page

`Date`	`MODIS hour`	`MSG hour`	`MODIS CF`	`TESCM CF`	ΔCF
2009-06-11	10:30	10:27	0.027676	0.024932	0.002743
2009-06-11	19:55	19:57	0.449426	0.510954	-0.061528
2009-06-11	21:30	21:27	0.151294	0.176813	-0.025519
2009-06-11	21:35	21:42	0.099359	0.098724	0.251701
2009-06-12	09:30	09:27	0.309550	0.183250	0.533032
2009-06-12	09:35	09:42	0.024085	0.000724	0.023361
2009-06-12	11:10	11:12	0.299864	0.078929	0.220935
2009-06-12	20:35	20:27	0.036813	0.012963	0.02385
2009-06-12	20:40	20:42	0.269430	0.146494	0.122936
2009-06-12	22:15	22:12	0.254808	0.320120	-0.065312
2009-06-13	08:40	08:42	0.159140	0.022167	0.136972
2009-06-13	10:15	10:12	0.051735	0.008578	0.043157
2009-06-13	11:55	11:57	0.609033	0.299914	0.309119
2009-06-13	21:20	21:27	0.055559	0.022963	0.032596
2009-06-14	09:20	09:27	0.062560	0.045667	0.016893
2009-06-14	11:00	10:57	0.556103	0.536665	0.019438
2009-06-14	20:25	20:27	0.040221	0.034628	0.005593
2009-06-14	22:05	22:12	0.801483	0.781801	0.019682
2009-06-15	10:00	09:57	0.498149	0.415007	0.083141
2009-06-15	10:05	10:12	0.019908	0.003216	0.016692
2009-06-15	11:40	11:42	0.296080	0.475335	-0.179255
2009-06-15	19:30	19:27	0.352565	0.433694	-0.081129
2009-06-15	21:05	20:57	0.005764	0.001005	0.004759
2009-06-15	21:10	21:12	0.386163	0.278779	0.107384
2009-06-15	22:45	22:42	0.902869	0.896293	0.006575
2009-06-15	22:50	22:57	0.579941	0.622801	-0.042860

Chapter 4

Retrieval of clouds parameters using SEVIRI

Several works have shown the capabilities of VIS, NIR and IR satellite measurements to characterize cloud-top microphysical structure and several algorithm have been introduced to retrieve cloud top parameters. The availability at geostationary scales of VIS-NIR-IR radiances from SEVIRI (in Europe) makes possible to observe the evolution of such cloud top parameters following the cloud life cycle every 15 minutes, and assess closer relations with cloud features. The objective of this chapter is to introduce a retrieval scheme in order to estimate cloud optical thickness and cloud effective radius using SEVIRI data and the radiative transfer model Santa Barbara DISORT Atmospheric Radiative Transfer (SBDART) and to apply these measurements to analysis temporal evolution of convective systems.

In this chapter SBDART model and its sensitivity analysis will be presented. Then, the cloud parameters retrieval method and its applications to convective systems analysis will be described.

4.1 SBDART: simulation scheme and sensitivity analysis

SBDART (Ricchiazzi and Guatier, 1998) is a software that computes plane-parallel radiative transfer in clear and cloudy conditions within the earth's atmosphere and at the surface. It includes all relevant processes that affect from ultraviolet to infrared radiation fields. The code resolves the radiative transfer equation numerically integrated with a sophisticated DISORT model (see section 2.3.1).

Scattering by spherical water droplets and ice crystal is computed by SBDART using a Mie scattering code. Molecular absorption is based on low-resolution band models developed for LOWTRAN 7 (LOW-resolution atmospheric TRANsmition) atmospheric transmission code (Pierluissi and Peng, 1985).

The model allows to describe a scene using different physical models available in SBDART or a user defined description for each of the following parameters:

- For the description of the *atmospheric profile* it provides standard vertical profiles of pressure, temperature, water vapour and ozone density. Six different standard atmospheric profiles (tropical, midlatitude summer, midlatitude winter etc.) can be adopted.

- In order to parametrize the *ground surface* spectral albedo SBDART use 6 types of surface: snow, ocean water, lake water, sea water, sand, vegetation. Each surface is assumed Lambertian, i.e. it reflects the radiation completely isotropic.

- SBDART can compute the radiative effects of several lower- and upper-atmosphere *aerosol types*. In the lower atmosphere, typical rural, urban or maritime conditions can be simulated.

- *Cloud* parametrization occurs setting the cloud optical thickness (or the LWC), the effective radius and phase of cloud particles, and height (or pressure) top cloud.

After setting the optimal parameters to describe the scene and the sun-satellite geometry (sun and satellite zenith and azimuth angles) the model compute the satellite radiances in the chosen spectral range. The radiances can be simulated using a specific filter function that characterize the given sensor. In our cases the SEVIRI filter functions for each channel used have been downloaded from EUMETSAT website and have been set as input files in order to obtain the most accurate radiance simulation.

4.1.1 Sensitivity analysis of the model

Several sensitivity tests has been implemented to verify and evaluate the SBDART behaviour in the VIS-NIR spectral bands varying different cloud and atmospheric parameters. In this section only few examples are reported, among several test carried out during this preliminary phase of work.

Figure 4.1 shows the strong sensitivity of visible reflectance to cloud optical thickness, while effective radius and phase of cloud particles slightly affect visible reflectance. On the other hand 1.6 reflectance depends on effective radius as is shown in figure 4.2, while dependence on cloud optical thickness is flatter than at visible wavelength. Moreover, in this figure the reflectance dependence on particle phase is shown, this fact is more highlighted in figure 4.3 where ice particles has higher reflectance (until 0.7 of difference for 5 μm of effective radius) than the water ones.

4.2 The retrieval scheme

The parameters extraction algorithm, purposely developed for the SEVIRI sensor, is based on the following steps.

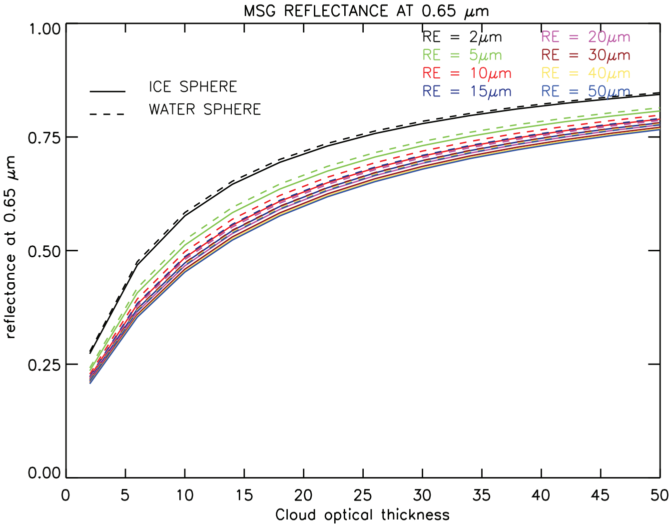

Figure 4.1: The SBDART simulated reflectance as function of cloud optical thickness for different effective radius of spherical (ice or water) cloud particles at 0.6 μm MSG channel.

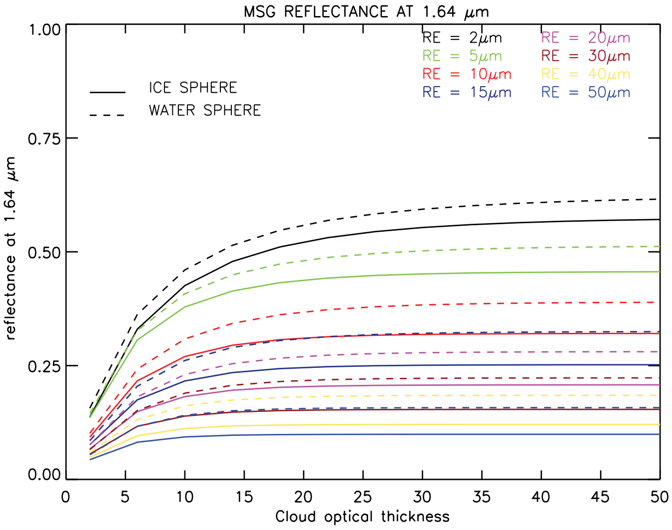

Figure 4.2: The SBDART simulated reflectance as function of cloud optical thickness for different effective radius of spherical (ice or water) cloud particles at 1.6 μm MSG channel.

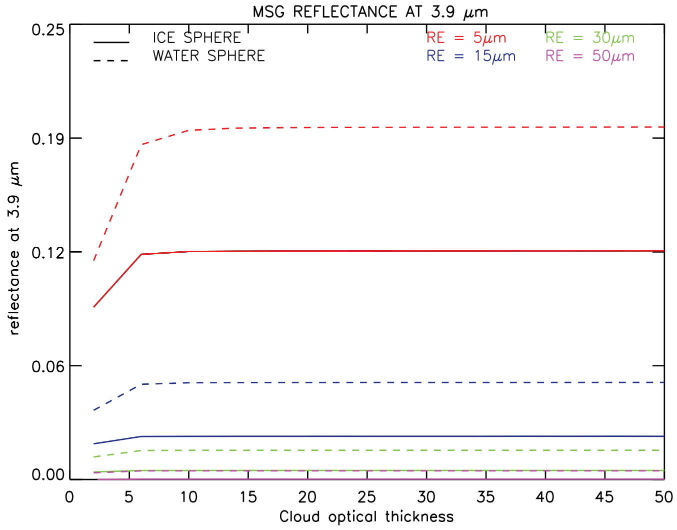

Figure 4.3: The SBDART simulated reflectance as function of cloud optical thickness for different effective radius of spherical (ice or water) cloud particles at 3.9 μm MSG channel.

The reflectance has been simulated setting:

1. Zenith sun, azimuth difference and zenith satellite angles fitting the data set.
2. Cloud optical thickness (τ) from 0 to 100.
3. Effective radius (Re) from 2 to 40 μm(ice sphere).

Collecting all simulations the resulting two look-up tables (one for each band) consist of a series of τ and Re values matched with the corresponding reflectance. By fixing a triplet of angles we obtain by trilinear interpolation a series of simulated reflectances depending on τ and Re for each band. From 0.8 μm and 1.6 μm satellite measurements and the actual scattering geometry the Re and τ cloud parameters are determined by minimizing over the look-up tables the root mean square difference (RMSD) between simulated and observed radiances:

$$RMSD = \sqrt{(0.85_{measured} - 0.85_{simulated})^2 + (1.64_{measured} - 1.64_{simulated})^2} \tag{4.1}$$

It is worth to remark the approximation on which the simulation is based:

- Atmosphere is non-scattering and non-absorbing (perfect window);
- Cloud-top particles are ice spheres;
- Cloud-top height is fixed at 5 km.
- Earth surface is a plane parallel Lambertian surface and its albedo is chosen as sea water type.

Further, for the SBDART simulation, the mid-latitude summer standard atmospheric profile has been set. Varying the cloud optical thickness and the effective radius the 0.85 and 1.64 μm look-up tables are obtained.

Fig. 4.4 shows the simulated reflectance values versus cloud optical thickness and for several effective radius values in VIS and NIR bands. The red star is determined by the 0.8 μm and 1.6 μm satellite measurements. The position in the look-up table indicates the closest Re and τ that are respectively: 8 μm and 14.

4.3 Application: τ and Re temporal analysis of cloud convective systems

One application of these parameters is to analyse the development of the top of convective systems following their life-cycle.

The convection process starts when a portion of moist and warm air is lifted up. This moist air is highly buoyant and causes a strong vertical motion (called updraft) when the hydrometeors production takes place, the latent

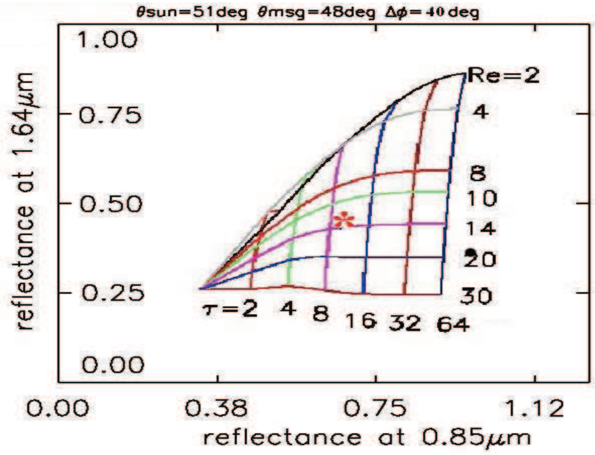

Figure 4.4: The cloud optical

heat released and the buoyancy increased. Convective structures may extend from few kilometres and duration of less one hour to hundreds kilometres and duration of one day for mesoscale organised clusters.

Fig. 4.5 shows the typical single-cell thunderstorm evolution detected by radar, where the early (left), the mature (middle) and the dissipative life stage (right) are shown. The beginning stage is characterized only by the starting updraft thanks to which the precipitation particles begin to grow. The mature stage presents an increased upward motion, so that the suspended particles may further grow. During this stage the convective precipitation is generated. The last is the decaying stage with only the downward motion that leads to more widespread and lighter stratiform precipitation.

The deepest convective events present very high and cold cloud top in the satellite IR observation, and the ice large top particles are well identified using the NIR channels. In this analysis we defined “cell” as a small clouds entity recognised from satellite VIS-IR observations as a compact cloud signature characterised by a rapid growth in size and with a round shape at the early stage. It has to be remarked that this ”cell” could also be a cluster of single updraft that can be properly detected only by radar. From the IR point

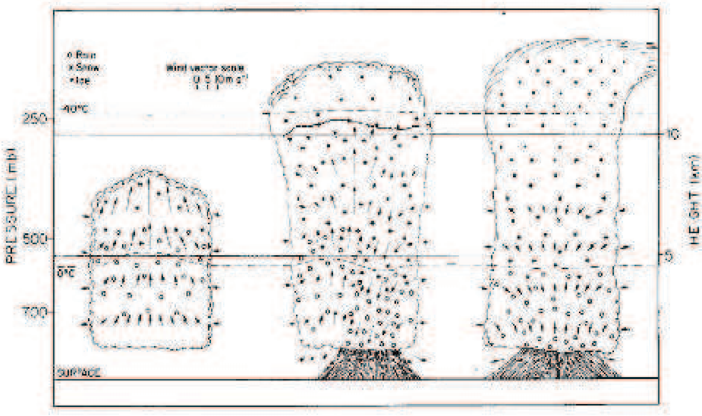

Figure 4.5: Single cell storm life evolution (from Rogers, 1977).

of view the cell life-cycle can be recognised: at early stage few cold pixels detects the updraft of the single cells, during the mature stage the cloudy areas increase adding warmer pixels that detects the anvils, at the dissipative stage the temperature of the area increase.

The aim of this analysis is to follow the cloud top evolution to understand how the physical properties change during the different stages of the storm formation and development, from the early to the mature and then dissipative stage of the cloud system. Following the estimated parameters (tested by Roberto et al. (2006) at our University) are listed:

Cloud optical thickness is computed from bispectral (VIS-NIR) SEVIRI analysis as described in section 4.2, its maximum considered value is 100 and it is sampled in 4 categories (20-40, 40-60, 60-80, and > 80). The threshold above 20 is chosen in order to screen out thin clouds that can be affected by ground reflectance.

Cloud particles effective radius for pixel with optical depth higher than 20, is sampled in 4 categories, from 2 to 8 μm, from 8 to 14 μm, from 14 to 20 μm and above 20 μm: the value of 14 μm is highlighted, since there is a relationship between this value of particle size and the probability of precipitation at the ground (Rosenfeld and Gutman, 1994).

Cloud top temperature, computed from SEVIRI 10.8 μm channel, is a measure of the cloud top height and analysing its time evolution can be estimated the updraft velocity by the cloud top divergence. A fast cloud top cooling and a rapid increase of the size of the cold area is referred to the first stages of the cell development. For the analysis of convective episodes, the cloud area is estimated starting from the 231 K isotherm, usually used to define deep convection at mid-latitude (Maddox, 1980), and sampled in 4 categories: $> 231K$, $231 - 226K$, $226 - 221K$, and $< 221K$ (i.e. above the tropopause).

4.3.1 Temporal development of a convective event

A convective system occurred in Balkans on 20 June 2004 characterized by the development of a number of convective cells. It has been possible to analyse the temporal development of two distinct cell from satellite images.

Two cells (A and B) are selected in this region and their temporal development in terms of cloud optical thickness (see figure 4.6) is followed. At first time (10:27) only cell A is present (red box in fig.4.6-a), while cell B is detected at 11:27 (orange box in fig.4.6-e). Cell A at the early stage (from 10:27) is composed by few pixels showing high τ values at the centre surrounded by lower values. The cell grows keeping the same shape until 11:42 where it reaches the maximum extension with the higher τ values considered as the end of mature stage. Then the dissipative stage occurs: the optical thickness decreases and the cloud extension starts reducing. Cell B is detected by just 3 pixels with low τ values, it grows in terms of size and τ values until 12:57 (mature stage 4.6-h) and then τ values decrease (dissipative stage).

The temporal development of the cells can be also followed in fig. 4.7, where the four range of optical thickness, effective radius and cloud top

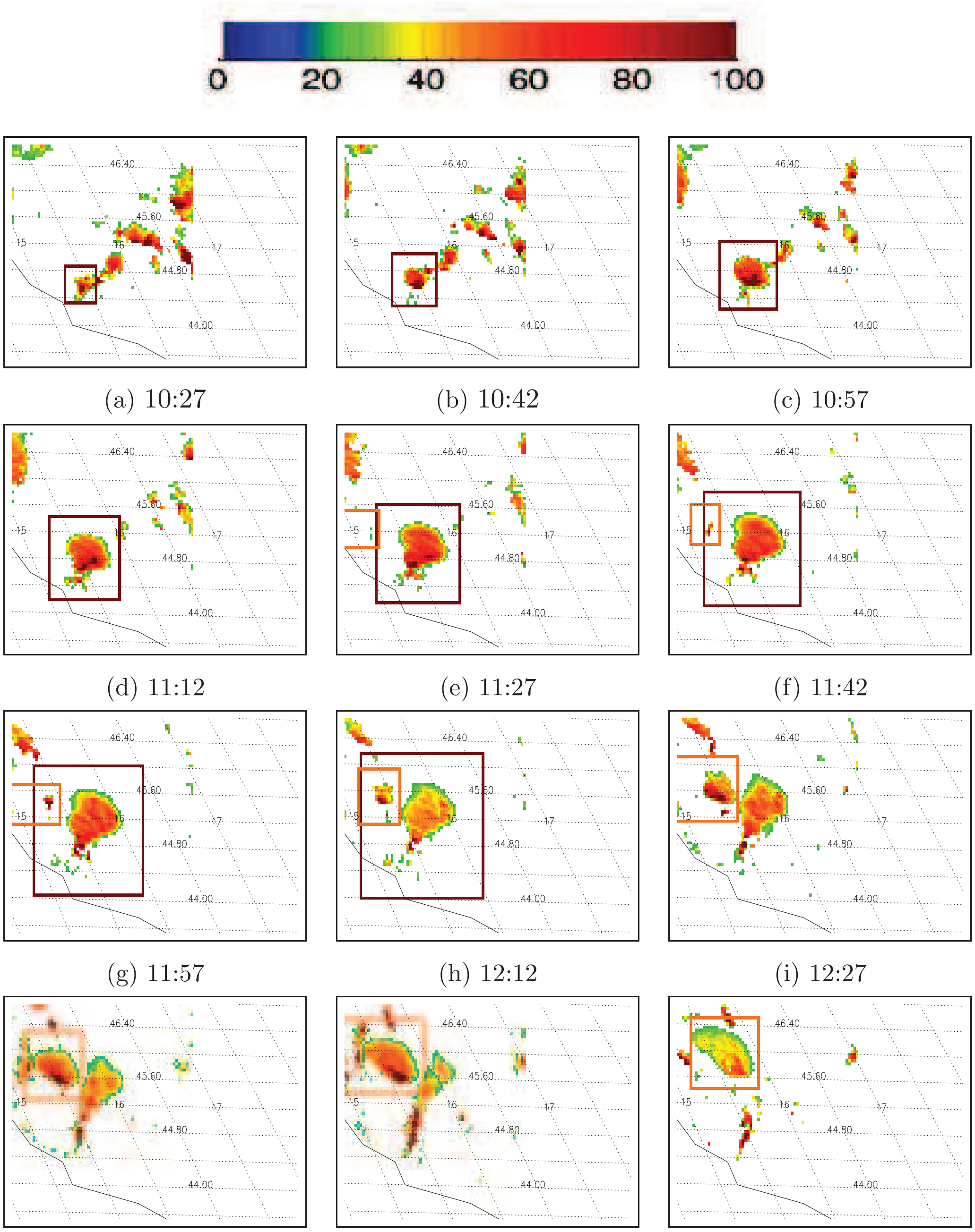

(a) 10:27 (b) 10:42 (c) 10:57

(d) 11:12 (e) 11:27 (f) 11:42

(g) 11:57 (h) 12:12 (i) 12:27

(j) 12:42 (k) 12:57 (l) 13:12

Figure 4.6: The optical thickness temporal evolution of a two convective events: *A* (selected by the red square) and *B* (selected by the orange square). The event occurred from 10:27 to 13:12 on 20-06-2004.

temperature (described in previous sections) are plotted trying to recognise the different stages of its life-cycle.

The analysis of τ of cell A and B (fig. 4.7 a and b) shows similar behaviour: all the areas grow in size with comparable growth rate. The maximum thickness area (yellow lines) after the initial growth remains constant, being related to the size of the main updraft currents. The end of the mature stage is characterized by a decreasing of the size of intermediate thickness areas, and a grow of the low τ areas.

The effective radius analysis (fig. 4.7 c and d) shows that the area of largest re grow at the same rate. Cell A shows also an increase of 14-20 μm area during the early stage, identifying the presence of a wide anvil structure.

The temperature time series (fig. 4.7 e and f) show different behaviour. For cell A, the cloud top remain warmer (above 231 K) during all the event. The thermal structure of cell B is more complex: the updraft in the early stage reaches the tropopause at 223 K (from San Pietro Capofiume sounding at 12:00 UTC) and then the cluster grows below the tropopause at higher temperature.

4.3.2 Convective cluster analysis

The convective events analysed here occurred on 07 June 2005 in South Corsica and lasted from 9:42 to 14:42. It was characterized by the development of several convective cells that is difficult to distinguish from satellite image

The temporal evolution of cloud optical thickness is shown in Fig.4.8 and 4.9. At the first time one pixels for τ above 20 is found and it is the first embryo of the cluster (cell C). It grows in size and τ values for a couple of hours and at 12:12 another cluster is detected at North-East of cell C. At the next time (12:27) the two cells merge although it possible to distinguish the temporal evolution of each one. After 12:27 cell C begins its dissipation

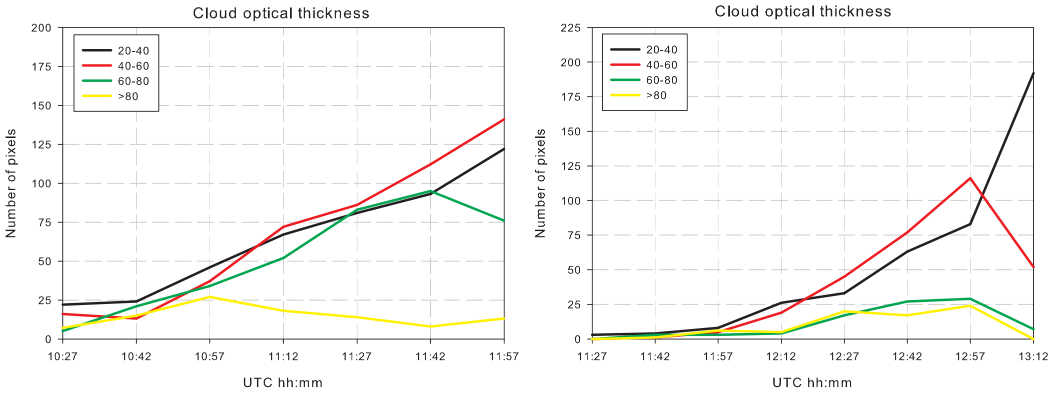

(a) cell *A* (b) cell *B*

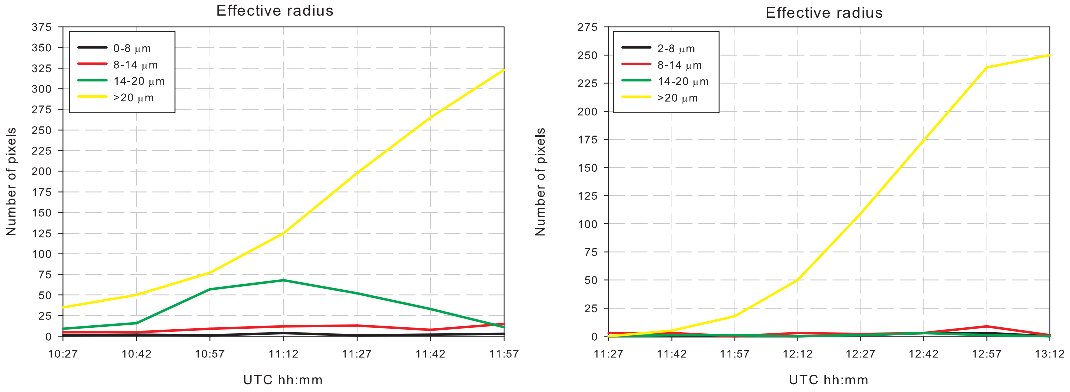

(c) cell *A* (d) cell *B*

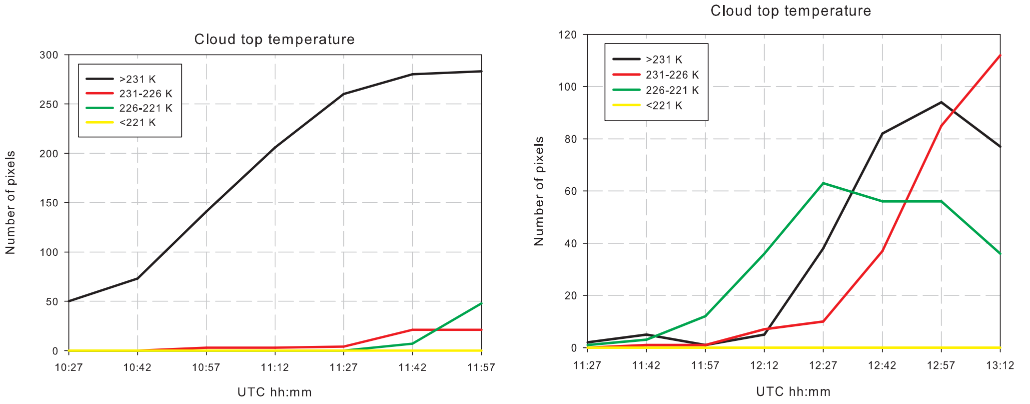

(e) cell *A* (f) cell *B*

Figure 4.7: Area of pixels in four classes of cloud optical thickness (a and b) effective radius (c and d) and cloud top temperature (e and f) function of time: cell *A* in the left panels (a, c and e) and cell *B* in right panels (b, d and f). Convective event on 20-06-2004.

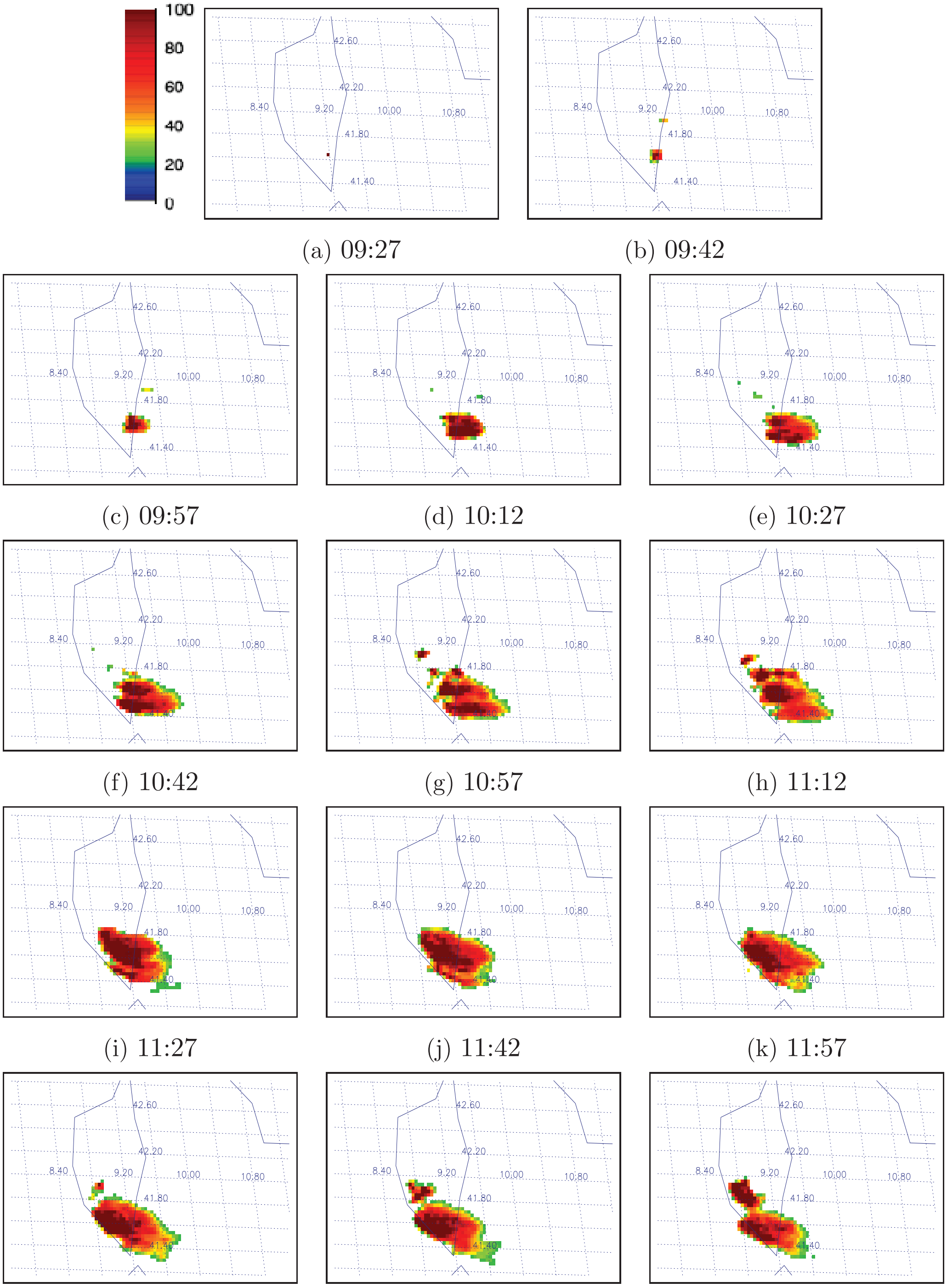

(a) 09:27 (b) 09:42

(c) 09:57 (d) 10:12 (e) 10:27

(f) 10:42 (g) 10:57 (h) 11:12

(i) 11:27 (j) 11:42 (k) 11:57

(l) 12:12 (m) 12:27 (n) 12:42

Figure 4.8: The optical thickness temporal evolution of a two convective cells. The event occurred from 09:27 to 14:42 on 07-06-2005.

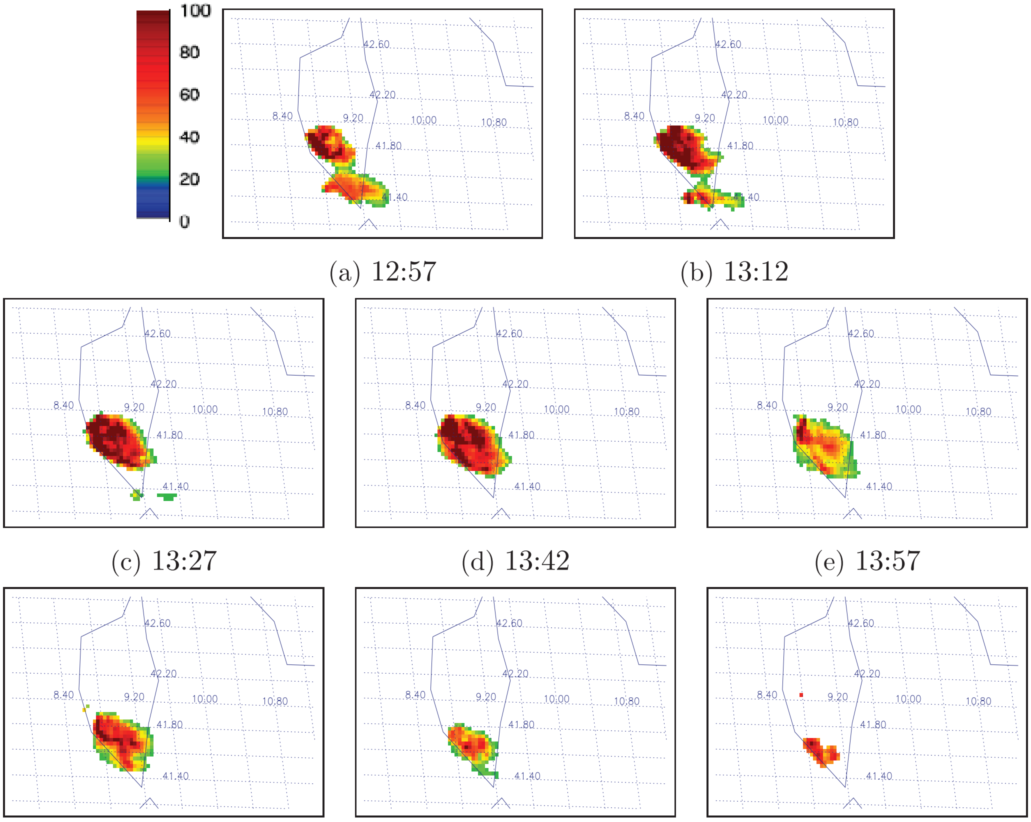

(a) 12:57 (b) 13:12

(c) 13:27 (d) 13:42 (e) 13:57

(f) 14:12 (g) 14:27 (h) 14:42

Figure 4.9: continue figure 4.8

stage, while cell D grows until 13:42 where cell C is completely dissipated. During the last hour of the event the cell D dissipation stage occurs.

The temporal evolution of the event is shown in figure 4.10 respectively in terms of optical thickness, effective radius and cloud top temperature distributed in the four classes previously described. The optical thickness is variable for the four classes due to the growth and dissipation of a number of cells. Despite of this the area of τ follow a similar trend for all the classes. In the first part (from 9:27 to 11:12) the four τ areas grow, during the same time interval the areas of effective radius over 14 μm increase and the cloud top temperature is above 231 K. For the following two hours and half (from 12:12

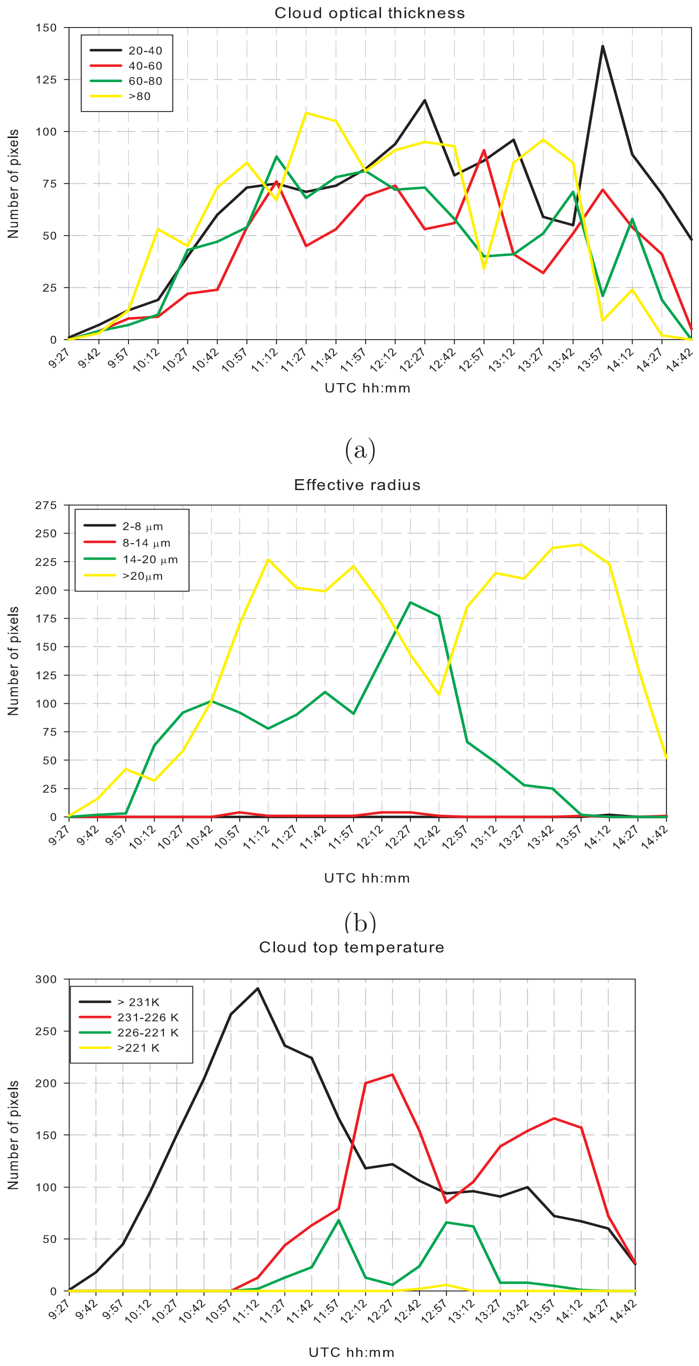

(a)

(b)

(c)

Figure 4.10: Area of pixels in four classes of cloud optical thickness (a) effective radius (b) and cloud top temperature (c) function of time for the convective event on 20-06-2004.

to 13:57) the area of cluster remain almost stationary but its temperature decrease. During the last part of the events (from 13:57 to 14:42) the cloudy area decrease, τ are smaller, and CTT increases.

In these plots the detection of the second cluster is highlighted after 11:57 by the area decrease of highest τ (> 80), the area decrease of effective radius $> 20\mu m$ and the area increase of re $14 - 20\mu m$ and the decreasing of the cold area (226-220 K). The early stage of the second cluster is underlined by the increase of CTT area 226-220 K after 12:27 being related to high height level of the cell towers.

The second of the two clusters analysed is characterised by a shorter lifespan and quick growth of the cold area probably determinate by different large number of updraft columns that fast reach upper tropospheric levels.

4.3.3 Comparison between VIS-NIR-IR retrievals and MW observations

A qualitative comparison to passive MW satellite images for the analysed cells is described in this section. The characteristic of the radiation at MW is that, depending on the frequency, hydrometeors interacts differently with radiation: ice particles have high transmissivity at the lower frequencies (below 20 GHz), while rain drops has high emissivity. Analysing multifrequncy data is then possible to retrieve information from inner cloud layers (Mugnai and Smith, 1984; 1988).

The drawback of a MW approach to cloud studies is that, due to diffraction problems, MW radiometers can only be used on low orbit and thus with a revisiting time not suitable for meteorological monitoring. In this work we just used the available Advanced Microwave Scanning Radiometer - Earth Observing System (AMSR-E) overpasses to qualitatively support the cell analysis carried on with VIS-NIR-IR retrieved parameters in the previous sections. In figure (4.11-a) the retrieved optical thickness from SEVIRI at 12:12 UTC is shown compared to the AMSR-E 12:13 overpass over Adriatic sea, on 20-06-2004. The optical thickness of the considered cell (dark red box in fig.4.11-a) is rather low for most of the cloud structure, with only few pixel at higher value at the southmost tip of the cloud. The brightness temperature at 89 GHz, shown at the original ground resolution (6x4 km^2) in fig.4.11-b , in the area covered by the cloud (box in fig.4.11-b) is very close to the one of the background. This indicates that the thickness of the cloud ice layer is not thick enough to scatter a sensitive amount of radiation, and thus the relatively thin cloud can not be detected by MW observations.

The AMSR-E overpass (at 12:10) for the second case study on 07-06-2005 occur at an early stage of the cell development, when a large part of the cloud has high optical thickness (see fig box 4.12-a). The 89 GHz temperature (see fig. 4.12-b)in this case is affected by the cloud and is much lower than the background, indicating the presence of thick ice layer. Even at lower frequency the signature of the cloud is evident: in fig.4.12-c and -d the brightness temperature at 37 and 23 GHz is shown at the ground resolution of 14x8 and 31x18 km2, respectively. This indicates that the cloud has also a water drops layer, and precipitation is expected.

Further studies would be needed to set up a multispectral observation strategy that takes advantage of the VIS-IR and MW capabilities.

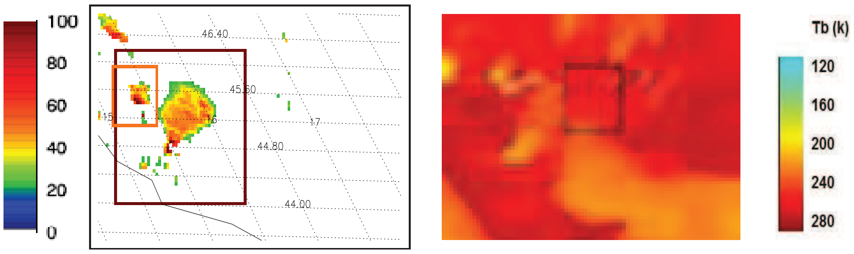

(a) (b)

Figure 4.11: (a) The optical thickness retrieved by VIS-NIR and (b) 89H (Horizontal polarization) GHz image for the convective event occurred on 20-06-2004.

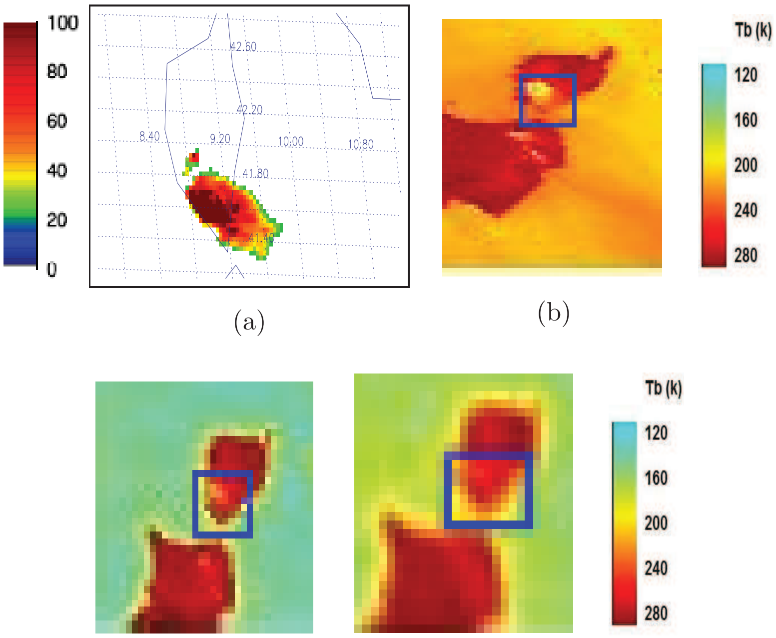

(a) (b)

(c) (d)

Figure 4.12: (a)The optical thickness retrieved by VIS-NIR and the (b) 89H GHz, (b) 37H GHz and (c) 23H GHz images for convective events occurred on 07-06-2005.

Chapter 5

Cloud cover associated to cyclone in upper troposphere

In the previous two chapters we have presented different high resolution cloud analysis to exploit the most advanced capabilities of new generation of geostationary orbit sensors. In this chapter we will move to larger scales, analysing cloud systems at synoptic/sub-synoptic scale, to exploit the satellite capabilities at climatological scale. This task does not need high resolution data thus the ISCCP-DX data at 30-km spatial resolution and 3 hours temporal resolution has been used.

The present analysis is aimed at investigating the cloud proprieties associated to cyclones in upper troposphere usually known as cut-off low (COL). The European area was identified as one of the regions where COLs are most common (Price and Vaughan, 1992; Kentarchos and Davies, 1998; Nieto et al., 2005) in particular during warm season. COL systems play a crucial role in driving the meteorological conditions over the whole area, sometimes related to severe weather, in particular over the Mediterranean regions (Porcú et al., 2003; Tripoli et al., 2005, Kotroni et al., 2006).

In this chapter the cloud pattern related to COLs development are analysed in terms of size, optical thickness and temperature of the top. The cloud distribution patterns around the COL centre, the dependence on the COL structure and season are considered. Finally the influence of the North Atlantic Oscillation (NAO) index on cloudiness associated to COLs systems is assessed.

5.1 The cut-off low systems

COLs are synoptic scale low pressure systems formed as a result of meridional shifts of the jet streams in upper troposphere. They are middle and upper troposphere cyclonically closed eddies and are isolated from the main western stream. In isobaric maps (absolute topography maps), cut-off lows are easily detected as close geopotential contours with a cold core, usually due to the fact that the air within the low has its origin at higher latitudes. These lows do not need to have a corresponding low in the lower levels of the troposphere, however, sometimes a COL may start as an upper-level trough extending to the surface once it has developed, although its intensity is higher in the upper troposphere and decreasing downward (Palmén and Newton, 1969).

As a general rule, the troposphere below COLs is unstable and convective severe events can occur, depending on surface conditions. COLs are associated with many substantial forecasting problems, mainly due to the different characteristics of the terrain and to the presence/absence of a warm ocean that permits/inhibits convection (Nieto et al., 2005). Thus, the precipitation distribution associated with COLs is a challenge to predict, especially when the precipitation is due to convection over a warm sea. COLs can bring moderate to heavy rainfall over large areas. In particular, they are among the most important weather systems that affect southern Europe and northern Africa and are responsible for some of the most catastrophic weather events

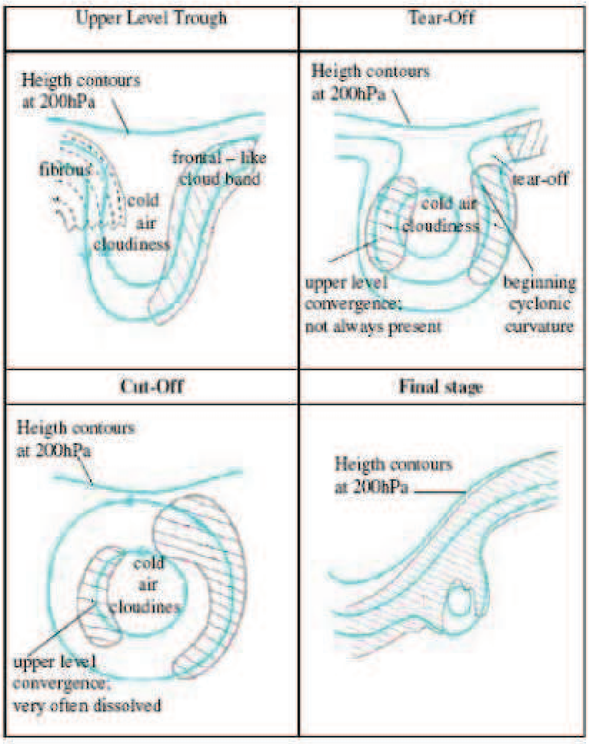

Figure 5.1: Diagram of the typical synoptic situation of a cut-off low showing: the different stages of its life cycle using the geopotential field and analysing satellite images (which results are shown in the overlapped shaded areas) (from Nieto et al., 2005).

in term of precipitation rate and effects at the ground (García-Herrera et al., 2001; Tripoli et al., 2005; Kotroni et al., 2006). Furthermore, cut-off lows are also important mechanism or stratosphere-troposphere exchange (Holton, 1983).

The typical process of the life cycle of a cut-off low can be separated into four stages (Nieto et al., 2005):

1. **The upper-level trough**: The development of a cut-off low requires unstable potential waves within the upper layer of the troposphere. The temperature field is characterized by the temperature wave situated

behind the geopotential wave. During this stage of development the geopotential and temperature wave increase in amplitude.

2. **The tear-off**: the increase in the amplitude of the waves continues, the trough deepens, and it starts to detach from the zonal stream. The cold air from the north streaming into southern regions is cut off from the general polar flow and a cold upper level low pressure system is formed.

3. **Cut off**: this process started when the tear off process is finished and the upper-level low is pronounced. The wind field at the uppermost tropospheric level (500 to 200 hPa) shows a well developed closed circulation, often completely cut-off from the general zonal flow.

4. **Final stage**: The upper-level low usually merges with a large upper trough in the main zonal flow.

5.1.1 Clouds studies associated to cyclonic systems

Several cloud cover analysis of cyclonic systems have been carried out with different approaches. Lau and Crane (1994) studied cloud proprieties linked to the mid-latitude baroclinic cyclones in wintertime over Atlantic and the summertime synoptic-scale disturbances occurring over western Pacific, and they found that the mid-latitude cloud patterns are linked to the vertical circulation induced by the advection of temperature and vorticity in developing baroclinic waves. Chen and Roeckner (2002) confirmed the same pattern of clouds associated with mid-latitude circulation systems using a General Circulation Model: both studies assessed an eastward displacement of the upper tropospheric clouds relative to the centre of largest upward motion at 500 hPa. Delagado et al. (2006) analysed cloud cover associated to COLs systems over Europe using a cloud classification algorithm applied to

Meteosat imagery on a database of 5 years with 35 occurrences and analysed the clouds evolving during the COL life cycle. They found that a higher percentage of cloud cover is always present in the frontal zone. Mid and low clouds contributed (about 35.2 %) to the total cloudiness more than high and deep convective clouds (about 16.7 %) although deep clouds best characterize the COLs life cycle.

5.1.2 NAO index impact on COLs

The NAO is one of the most prominent teleconnection patterns in Europe in all seasons (Barnston and Livezey, 1987), it consists of a north-south dipole of sea level pressure anomalies, with one centre located over Greenland and the other centre of opposite sign spanning the central latitudes of the North Atlantic between 35N and 40N. The positive phase of the NAO reflects below-normal heights and pressure across the high latitudes of the North Atlantic and above-normal heights and pressure over the central North Atlantic, the eastern United States and western Europe (Hurrel, 1995). The negative phase reflects an opposite pattern of height and pressure anomalies over these regions.

The links between the NAO and cyclone activity, temperature and precipitation patterns have been discussed in the literature (Marshall et al., 2001). Pinto et al. (2008) studied the analysis of NAO related to extreme North Atlantic Cyclones during 1958-1998, they found that the strong negative phase ($NAO > -1.5$) influences cyclone occurrences more than (7.6% vs 5.8%) NAO strong positive phase ($NAO > 1.5$). Nieto et al. (2007) analysed the influence of the major telecconections modes (i.e. El Niño-Southern Oscillation(ENSO), Quasi-Biennal Oscillation(QBO)), among these the NAO has the highest influence in COL occurrence: they found that the positive phase of NAO favouring autumn and spring development, while during summer no significant influence was found.

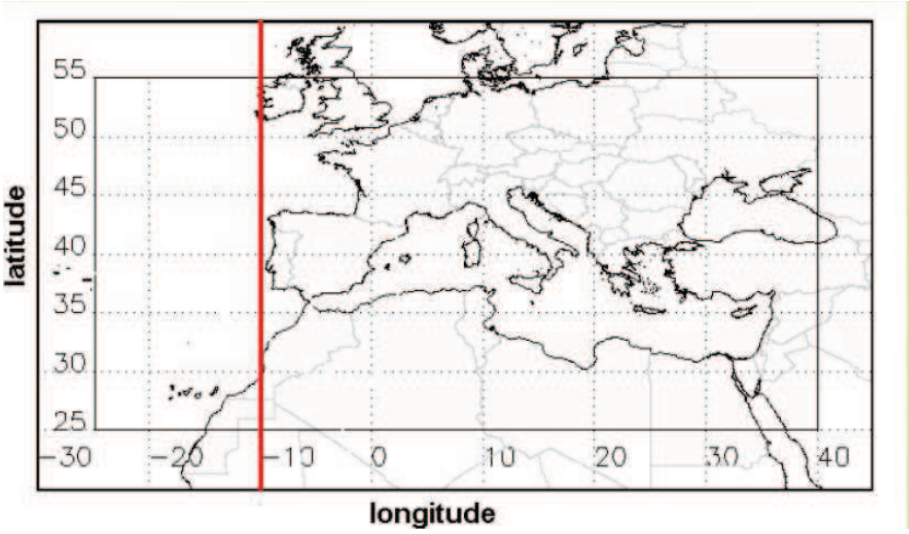

Figure 5.2: Area of interest: Atlantic area is in the left part (before the line), and the Mediterranean area is in right part (after the line)

5.2 Data and algorithm

The area considered for this study is centred on Mediterranean basin, includes North Africa and continental Europe limited between 30°W-45°E, 20°N-60°N as is shown in fig 5.2. This area is divided in two parts for further analysis: from 30°W to 10°W, referred as Atlantic area, and from 10°W to 40°E, referred as Mediterranean area.

Ten years (1992-2001) of warm season (April to September) data are considered in this work. From ERA-40 reanalysis, available freely on ECMWF website ($http : //data - portal.ecmwf.int/data/d/era40\_daily/$) every six hours on 2.5°x2.5° grid, a database of cut-off low occurrence in the selected area is extracted by means of a semi-automatic algorithm (see Porcú et al., 2007 for details). The ERA-40 data are at 23 pressure levels (plus surface) for the period 1957-2001 (Uppala et al., 2004), the algorithm used the following parameters: geopotential height (at the pressure levels: 200, 250, 300 and 1000 hPa), temperature and zonal wind at 200 hPa.

A total of 273 COLs is found by the algorithm, with 1358 occurrences, during the selected period. Considering the COL life-time, all detected COLs lasting less then 12hrs (observed only for one synoptic time) were not included. For the same period and area, an independent surface cyclone (LOWs) database was constructed by means of an automatic procedure based on pressure minimum and gradient analysis (Trigo et al., 1999).

In order to classify COL vertical structure, we considered the classification proposed by Porcú et al. (2007): the COLs were classified accordingly to the vertical geopotential structure below the COL and the presence of a simultaneous LOW at the ground. Starting from the original classification in 5 classes (Porcú et al., 2007), we simplified the approach considering if the COL is *deep* (i.e. the geopotential disturbance propagates throughout the whole troposphere) or *shallow* (the geopotential disturbance is confined in the upper troposphere). Of the total of 273 COLs, for 171 COLs an upper signature of the geopotential disturbance involves whole the troposphere (deep COLs), while the remaining 102 events are shallow COLs.

The cloud cover data related to COL occurrence are extracted from the International Satellite Cloud Climatology Project (ISCCP) archive: DX data Rossow and Shiffer (1991), available every 3 hours with a nominal 30x30km^2 footprint at sub satellite point, are analysed to estimate cloud cover and characteristics related to the COL lifecycle. The ISCCP DX dataset includes pixel level cloud information that is primarily based on the information of the cloud mask (CM), and on relevant information of cloud top temperature(CTT) and cloud optical thickness (τ). In this work the time resolution used is the lowest among the two dataset, ISCCP and ERA-40, (i.e. 6 hours).

Finally monthly mean of NAO index were freely downloaded from the NOAA website (http://www.cpc.ncep.noaa.gov/data/teledoc/nao.shtml) to evaluate the impact of this index on COL systems related cloudiness. Data used in this work are summarized in tab. 5.1, where the principle characteristics and applications of each dataset are described.

Dataset	**Temporal resolution**	**Spatial resolution**	**Application field**	**Parameters**
ISCCP-DX	3-hourly	30x30km^2	Cloud analysis	cloud mask; cloud top temperature; cloud optical thickness;
ERA-40	6-hourly	2.5°x2.5°	COL detection	geopotential height; temperature; zonal wind;
NCEP	monthly means	2.5°x2.5°	NAO-index	Sea level pressure.

Table 5.1: Summery of the data analysed

5.2.1 Assigning cloud cover to COL occurrences

The ISCCP-DX files are processed to extract the cloud cover assigned to a COL occurrences in order to evaluate cloud cover size and cloud proprieties of these systems. The algorithm detects the cloudy area searched in three steps:

1. Removal of isolated cloudy pixels: the cloudy pixels of the ISCCP-CM are analysed in order to separate large cloud patterns connected only by thin "bridges" composed by only few pixels (fig. 5.3-a). Pixel with less than 2 connected pixels are screened out from the original DX map.

2. Box analysis around the COL centre: this is the main part of the algorithm where the cloud shield is associated to a COL starting from its centre. At first the COL centre coordinate at the ERA-40 resolution is placed onto ISCCP grid. Considering the CM a 11x11 ISCCP pixel box around the centre of COL is searched and all the cloudy pixels

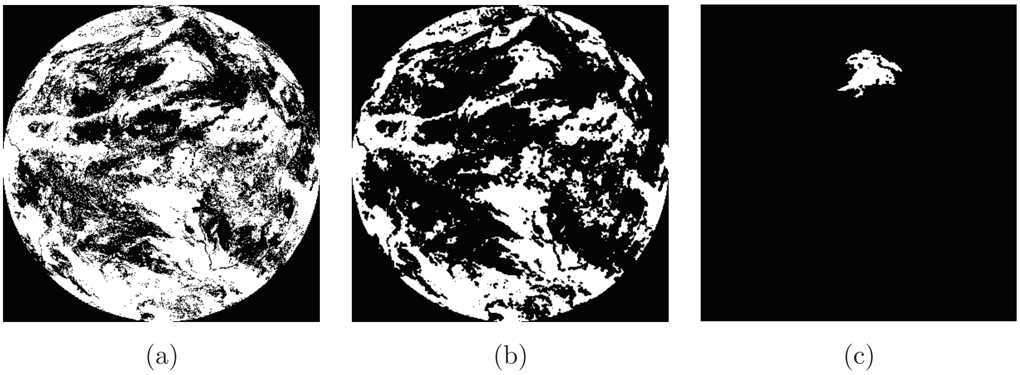
(a) (b) (c)

Figure 5.3: (a) ISCCP CM for the 25-04-1992 at 12:00 (white pixel = cloudy); (b) the CM after the step1 of the cloud detection algorithm (c)clouds associated to COL (step 2).

inside the box are classified as belonging to the given COL. For each cloudy pixels into the box, by a region growing algorithm, a spatially continuous cloud shield is associated to the COL (fig. 5.3-c).

3. Temperature threshold: a further screening is applied to the images based on the CTT in order to minimize very warm cloud top (fog and haze) and partially cover pixels, characterized by relatively high temperature as well. The cloudy pixels having a CTT above 283 K are screened out (this temperature is chosen consider a standard mid-latitude summer profile, and corresponds to a cloud height top of about 2 km).

In order to refine the automatic cloud shield definition and assignment, a posteriori test is made: if cloud shield size is too much wide to be analysed from the METEOSAT point of view (i.e. it touches the earth border in the satellite view) the COL occurrence is screened out. If half of the occurrences in a COL event are screened out the whole COL event is rejected. 205 (74 %) of the 273 COL events passed this test and a new dataset to analyse cloud proprieties is created. Finally the algorithm converts the pixel area associated at each COL centre into km^2 area considering the latitude and longitude of each pixels.

5.3 Data analysis and results

In this section the dataset of COL related to cloud cover (obtained by the algorithm described in section 5.2.1) is analysed: cloud cover size, cloud top temperature, and cloud optical thickness are the cloud parameters considered in order to identify the characteristics of clouds associated to the COLs systems and the relation between positive potential vorticity (PV) values in presence of a COL is assessed. Finally the NAO index section describes how occurrences and the associated cloud cover are affected by NAO.

5.3.1 Cloud cover size

The size of cloud shield associated to a COL occurrence varies over wide range: from zero to more than one million of km^2. Three classes of size are then identified in order to classified the cloud cover dataset and to extract cloud information for each COL system:

- *Small*: $0 - 10^5\ km^2$;
- *Medium*: $10^5 - 10^6\ km^2$;
- *Wide*: $> 10^6 km^2$.

For each occurrence is identified the cloud shield size class and for each event the average of these sizes is computed. The number of occurrences and events of COL, distributed in the size classes, are reported in tab. 5.2. Note that class small includes also the cloud-free occurrences, which are more of one third of the class small population.

	Small (cloud free)	*Medium*	*Wide*
COL occurrences	315 (130)	285	395
COL events	48	66	91

Table 5.2: COL occurrences and COL events distributed in the 3 size classes

At first, the seasonal sensitivity of cloud size distribution is assessed. In fig. 5.4 the histogram shows the occurrences percentage during the 6 months of the studied period: the Spring season (April, May, June) is characterized by large cloud cover occurrences while in Summer season the majority of the occurrences belongs to classes small and medium. A possible explanation is that Spring systems are more related to surface larger scales low pressure while in Summer are more frequent convective cloudiness, usually taking place at lower scales (Porcú et al., 2007). A further comment has to be made considering the warmer surface in Summer month: this can lead to an underestimation of cloud cover by the ISSCP DX given the large pixel, as it will be discussed later.

The different vertical structure of COLs can also affects the cloud cover size and proprieties: deep COLs are characterized by wide cloud shields and shallow COLs by small and medium as is shown in the histogram (fig. 5.5). The majority of deep COLs have a corresponding, dynamically related, depression at the ground: a surface cyclonic system often develops in the surface field, starting before or after the COL development (Porcú et al., 2007). In these cases diabatic heat transport into the deep cold air mass takes place from the ground, the atmospheric stability becomes weak so that deep convective cloud, shower and thunderstorm form (Kurz, 1988). On the other side, shallow COLs do not have a well structured depression at the ground, and are sometimes able to induce smaller scale instability, producing small cloud shields (or no cloud at all).

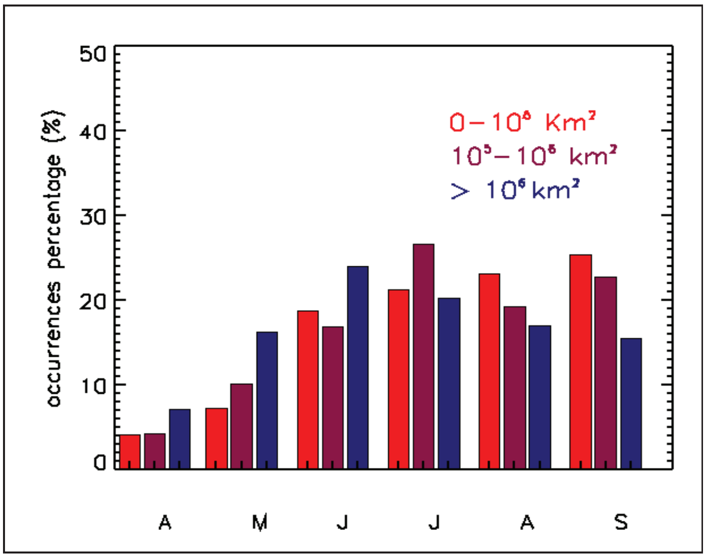

Figure 5.4: Monthly distribution of cloud size distribution considering the percentage of occurrences.

5.3.2 PV anomalies and cloudiness

In this section an investigation into the relation between the high positive PV values close in presence of a COL and the cloud cover associated to it is proposed.

PV is widely used as a parameter to dynamically characterize the lower atmosphere owing to its conservation for adiabatic, frictionless motions. PV is defined as follow:

$$PV = -g\left[f + \left(\frac{\delta v}{\delta x} - \frac{\delta u}{\delta y}\right)_p\right]\frac{\delta\theta}{\delta p} \tag{5.1}$$

where g is the gravitational acceleration, f is the Coriolis parameter, p is the pressure, θ is the potential temperature, u, v are respectively the zonal and meridional component of the wind velocity and the terms $\left(\frac{\delta v}{\delta x} - \frac{\delta u}{\delta y}\right)_p$ express the relative isoentropic vorticity. The units commonly used for the presentation of PV are $10^{-6}m^2s^{-1}Kkg^{-1}$, which Hoskins et al. (1985) suggested should be designated a PV unit (PVU). PV values less than 1.5 PVU

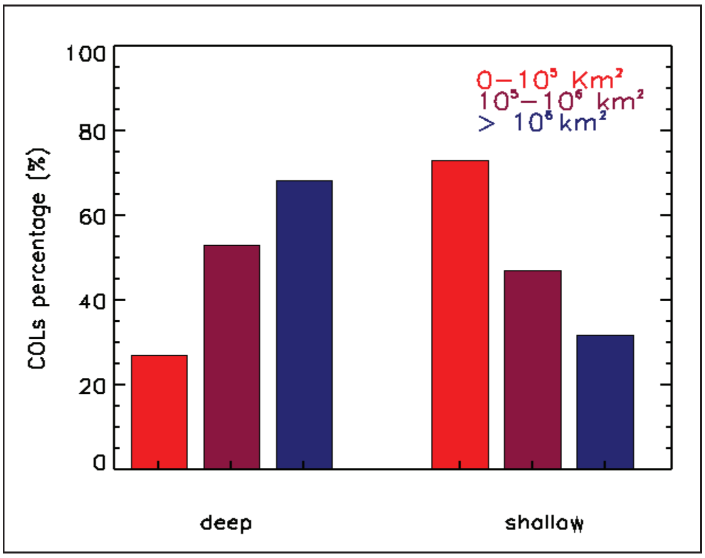

Figure 5.5: Deep and shallow COL s distribution in the three cloud size classes.

represent tropospheric air, and a value of more than 4.0 PVU indicates stratospheric air (Georgiev, 1999).

Positive PV anomalies in the upper troposphere level, commonly due to intrusion of stratospheric air, can be considered as indicators of deep cyclones (Hoskins et al., 1985) and often to severe systems (Porcú et al., 2003). Furthermore high positive PV values, stratospheric air is also characterized by low water vapour (WV) content. An operational method used to detect and monitor the air with a high positive PV is the WV geostationary satellite observations (Georgiev, 1999; Knippertz and Martin, 2007). A close relation between the dry regions on the WV images and high PV values at the rear of a developing cyclone (Demirtas and Thorpe, 1999).

To asses the relation between high PV values and cloud cover the dynamic tropopause was considered defined as the 1.5 PVU isosurface. The percentage of events with averaged size of cloud cover, distributed among the 3 size classes (described in previous section) are shown in fig. 5.6 as a function of the lowest level reached by the dynamic tropopause.

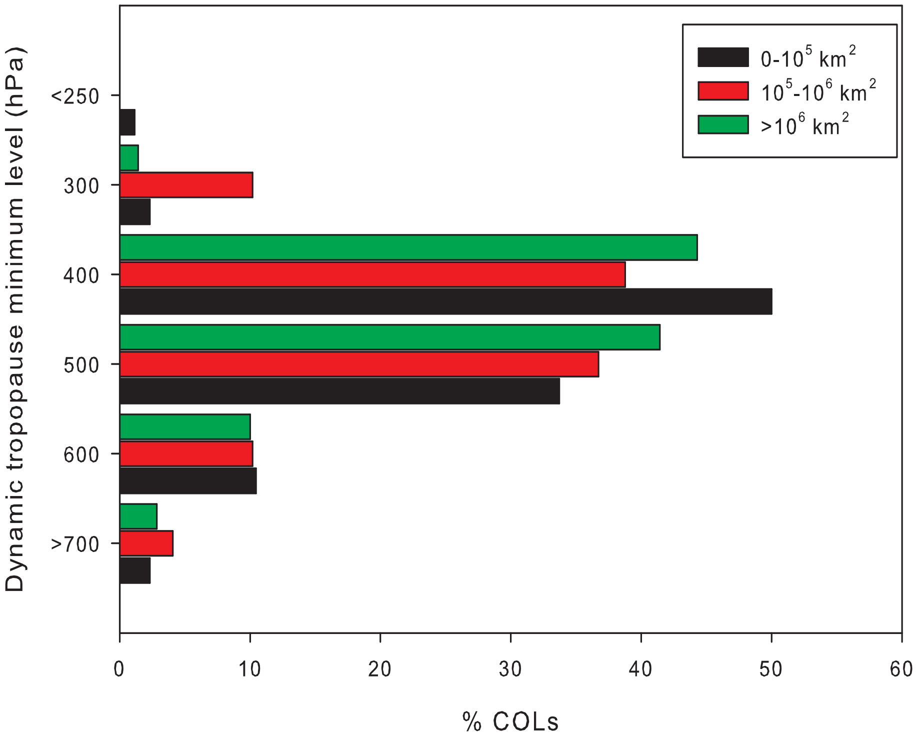

Figure 5.6: Percentage of the distribution of event averaged size cloudiness as a function of the lowest level of the dynamic tropopause during the COL life-time.

The level at 400hPa is the most populates, with the class small slightly prevailing, while at 500 hPa the occurrence of small cloud covers decreases, and the class large becomes the more populated one. For very few events, the stratospheric air reaches lower levels, with no clear impact on cloud cover size.

5.3.3 Cloud top temperature analysis

For each occurrences, excluding the cloud free ones (130), the minimum and the mean of CTT (CTT_{min} and CTT_{mean}, respectively), among the cloud shield, is computed, and plotted in fig. 5.7. The distribution of CTT_{mean}

shows a peak around 260K, while the CTT_{min} distribution have a peak around 220K. To describe the thermal properties of the cloud shields two thresholds are considered: 220K and 240K (two green vertical line).

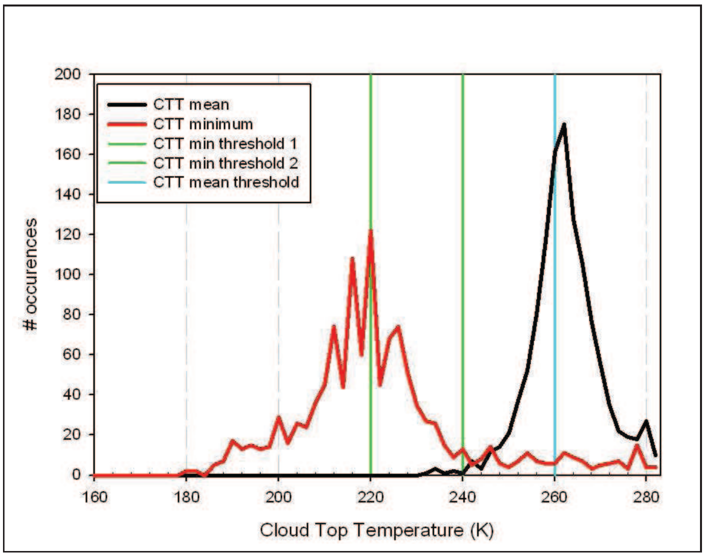

Figure 5.7: Distributions of CTT minimum and CTT mean. The two green lines are the CTT minimum thresholds and the light blue one is the CTT mean threshold.

For the minimum of CTT three ranges are established by the defined thresholds as follows:

- CTT_{min} cold: $< 220K$;
- CTT_{min} intermediate: $220 - 240K$;
- CTT_{min} warm: $> 240K$.

The season distribution of the CTT_{min} in the three ranges is showed in fig. 5.8. Clouds associated to COLs systems have different behaviour in the two parts of the considered seasons: Spring (AMJ) is characterized by wide ($> 10^6 km^2$) and cold ($< 220K$) cloud cover while Summer (JAS) cloud systems extend typically below the million of km^2 and for the most of the cases the temperature is above $220K$ (fig.5.4 and fig. 5.8), probably because in summer the cloudy pixel are affected by warmer background contribution than in spring confirming the previous explanation about seasonal distribution.

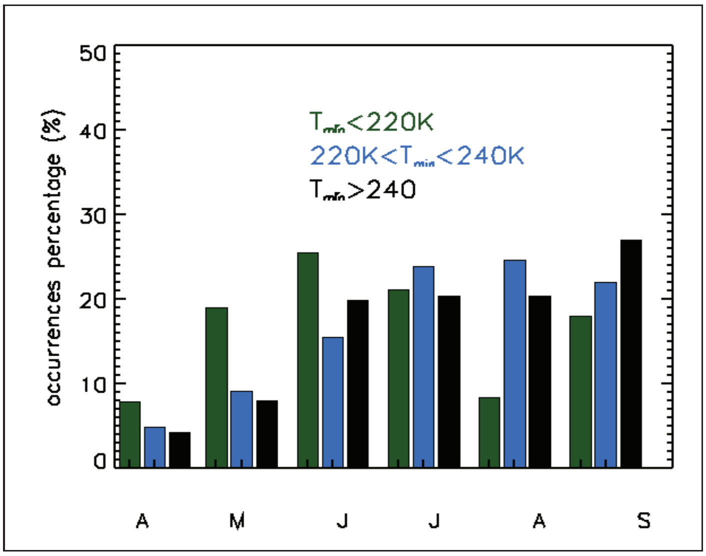

Figure 5.8: Monthly distribution of the three CTT minimum ranges

Figure 5.9 shows the normalized (with the total of cloudy pixels) surface distribution of cloud occurrences relative to COLs centre. The cloudy pixels associated to each occurrence are distributed among 3 classes on the basis of CTT previously defined thresholds labelled as follows: cold clouds ($< 220K$), intermediate clouds ($220 - 240K$) and warm clouds ($> 240K$). This analysis is carried out on 205 COL (with 795 occurrences) found with the cloud cover detection algorithm. Furthermore, the cloud occurrence is plotted only for the pixels having a counting more than 2.

Warm top clouds are more frequently found on the west side of the cloud shield (see fig. 5.9-a), while colder cloud tops are present on the eastern side (fig. 5.9-b). The highest occurrence of the coldest tops is on the north eastern sector of the cloud structure (fig. 5.9-c). Following the COL conceptual

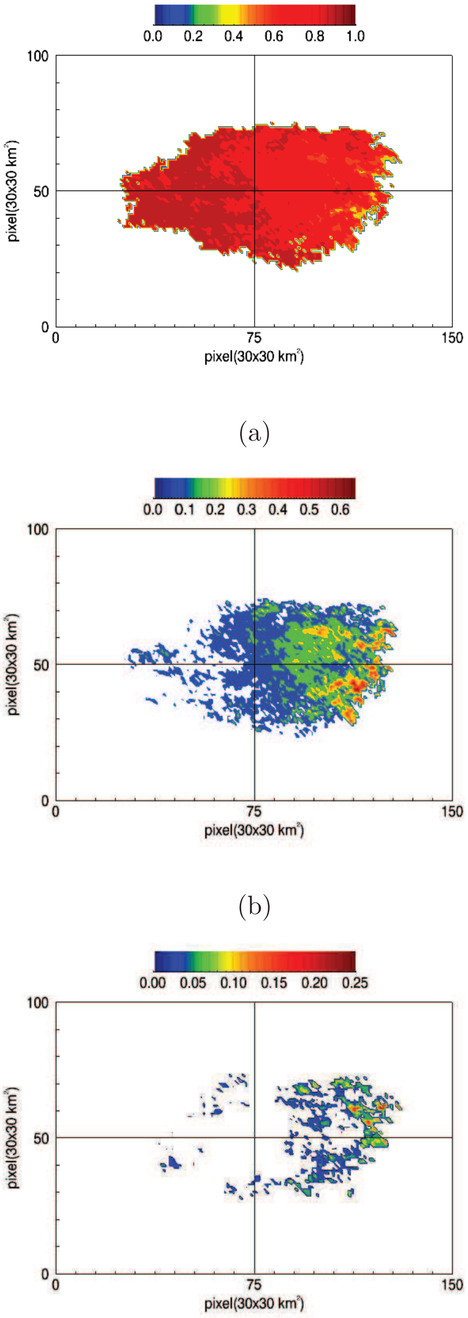

(a)

(b)

(c)

Figure 5.9: Normalized surfaces distribution of cloud occurrences associated to all COLs centre. (a)$CTT > 240K$; (b)$240 < CTT < 220K$; (c)$CTT < 220K$.

model, the more intense cloud growth occurs where a ridge of air thickness is expected (see fig.5.9-b). To complete this picture, a similar analysis of cloud optical depth is presented in the next section.

5.3.4 Cloud optical thickness analysis

In order to look into the proprieties of clouds associated to the COLs systems, the cloud optical thickness is analysed from ISCCP files. Clouds are classified by cloud optical thickness in thin ($0.0 < \tau < 3.6$), middle ($3.6 < \tau < 23.0$) and thick ($\tau > 23.0$) following the ISCCP studies (Rossow and Garder, 1993).

The distribution of the clouds optical thickness for all COLs relative to their centre is built up (fig.5.10) using the three τ classes. The majority of thin clouds are distributed in the North-West part, with respect to the centre, while the middle are located around the centre with a maximum in the South-West sector, finally, thick clouds density is higher in the North-East sector. The increasing of the clouds optical thickness has and eastward displacement respect to the centre of the COLs. This completes the analysis of the previous section, confirming the presence of thick and cold top clouds in the north east sector where the main convergence area is located.

Thick clouds are also found in southern sector, with CTT decreasing from West to East: this is probably due to the frontal development in the warm sector in case of well developed cyclonic structure at the surface, as it is expected for deep COLs. Finally, it has to be noted that the space of figures (figs. 5.9 and 5.10) is not isotropic, since the nominal pixel size and shape (30x30 km^2 squared area) at the sub satellite point (ssp) changes moving to the north: the pixel shape is stretched along S-N direction of about 50% of SSP size, and symmetric stretching is also expected along E-W direction, but to lesser extent.

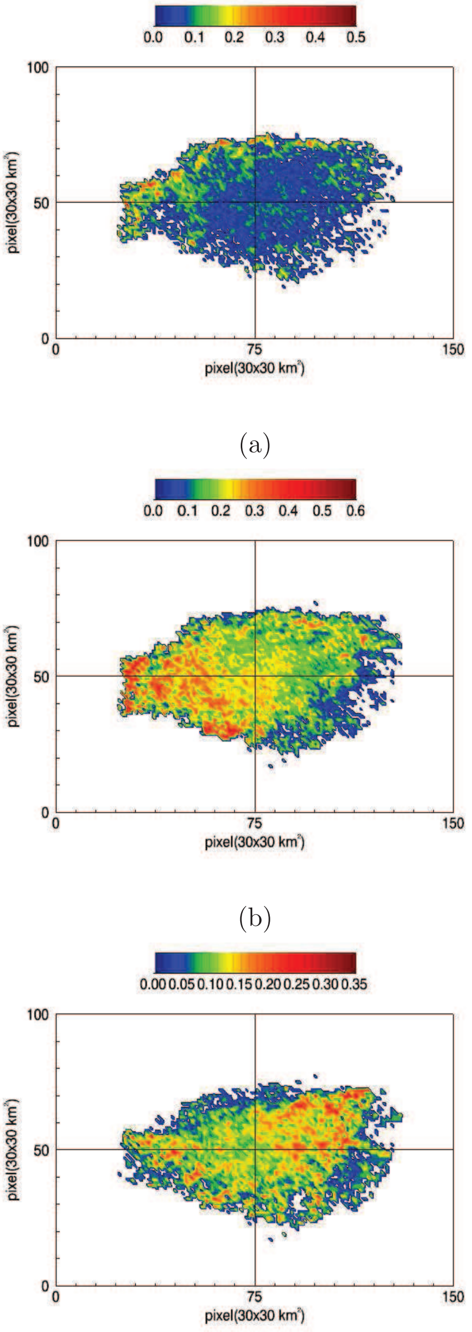

(a)

(b)

(c)

Figure 5.10: The distribution of the clouds optical thickness amount for all the COLs associated to clouds: (a) thin clouds,(b) middle clouds, (c) thick clouds.

5.3.5 NAO index and clouds associated to COLs

NAO monthly mean time series for the considered decade is plotted in fig. 5.11. Considering that stronger influence is expected for higher absolute values of NAO index, only months with the NAO index greater than 1 and lower than -1 are considered in this analysis. For this reason, the database reduces to 66 events, with 341 occurrences.

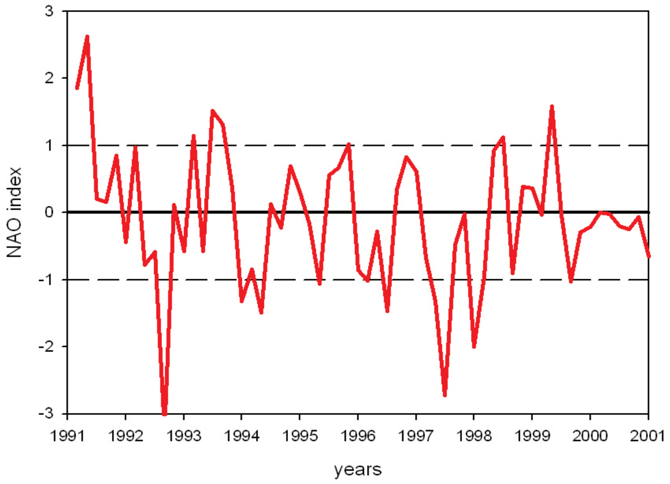

Figure 5.11: Monthly mean distribution of NAO index in the period studied

The seasonal analysis of NAO influence on the number of COL events is shown in table 5.3: it reports the number of COLs in Summer and Spring distributed between positive and negative NAO phases. More than 65% of events are in Spring and most of them are in positive NAO phase (according to Nieto et al., 2007).

In order to identify NAO influence on COLs systems, the analysis of vertical structure and clouds size associated to COLs are carried on. Furthermore this study is led considering the region of interest divided in two subregions (see fig. 5.2): Mediterranean and Atlantic area. The word “Mediterranean” has to be intended in a wide sense, i.e. the area centred on the Mediterranean

	$NAO > 1$	$NAO < -1$
Spring	25	18
Summer	7	16

Table 5.3: Numbers of COLs in summer and spring for the two NAO phases

sea, keeping in mind that COL occurrence is mostly confined between 35-45 N (Nieto et al., 2005).

NAO index affects in opposite way COLs structures into the two areas (fig. 5.12). The majority of deep COLs occurs during positive NAO phase in the Atlantic area, while in the Mediterranean area NAO negative phase induces more deep COLs. Shallow COLs dominate negative NAO phase in the Atlantic area while the opposite is true in the Mediterranean area.

Cloud cover size distribution associated to COLs in Mediterranean and Atlantic areas is also affected by NAO as shown in fig. 5.13. The two NAO phases have different behaviour in the two areas:

- in Mediterranean area: small and medium size classes are dominant in positive phase, while wide class dominates with negative NAO;
- in Atlantic area: medium and wide size classes are the most populated during NAO positive phase, while small size class is more frequent during negative NAO.

The NAO influence on European meteorology has been mainly assessed for cold months. This study confirms the role of positive NAO in hindering the development of deep COLs with larger cloud shields in the Mediterranean area also during the warm season. The opposite is true for negative NAO.

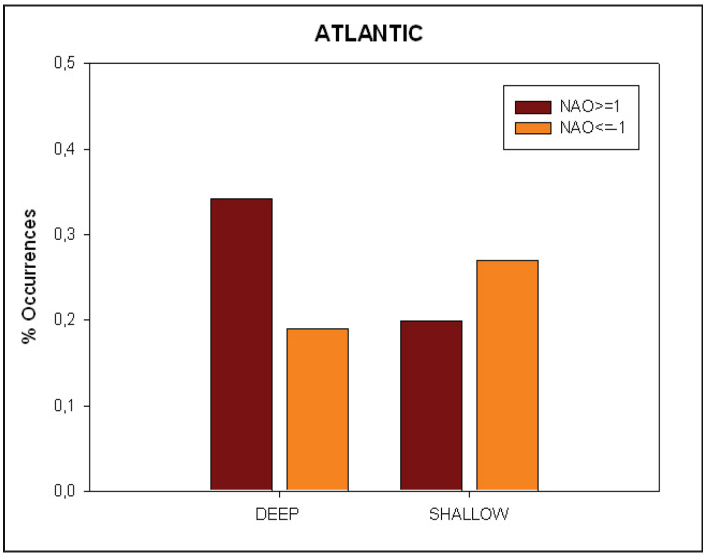

(a)

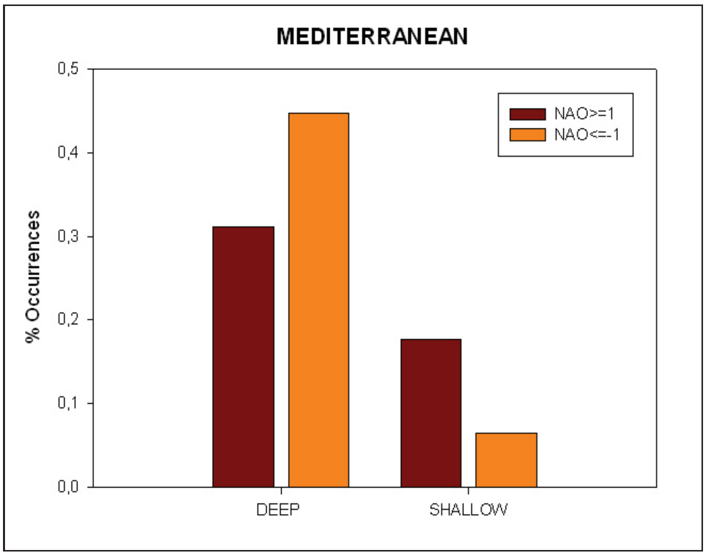

(b)

Figure 5.12: Percentage of occurrences in deep and shallow classes during positive and negative NAO phases: (a) in Atlantic area (b) in Mediterranean area.

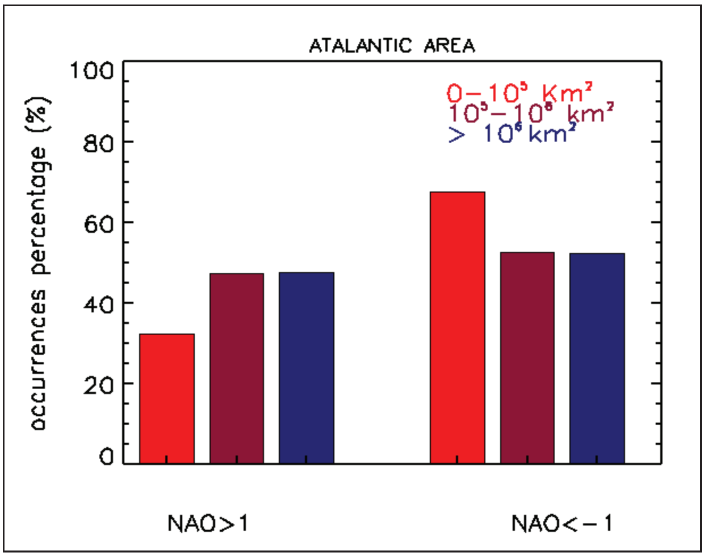

(a)

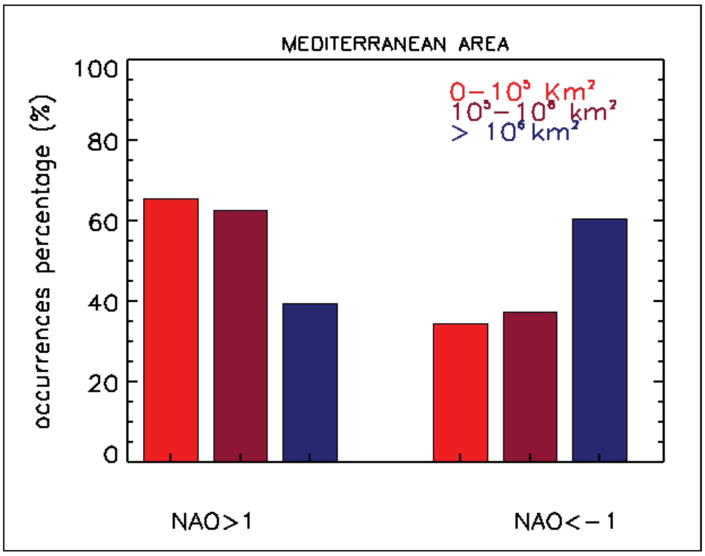

(b)

Figure 5.13: Percentage of occurrences in the three size classes for positive and negative NAO phases (a) in Atlantic (b) in Mediterranean area.

Conclusions

In this thesis different aspects of the use of satellite data products have been addressed with the aim to set up a set of tools to analyse the main characteristics of cloud systems at different spatial and temporal scales. Along the path to the final goal some byproducts of the research are derived, especially oriented to the use of satellites data for weather monitoring and cloud climatology.

First, a set of cloud products at high temporal and spatial resolution has been produced by two algorithms that use SEVIRI data. After a series of sensitivity tests to verify the temporal variation of the brightness temperature at window infrared spectral bands, a temporal statistical cloud mask algorithm has been implemented using the 10.8 μm brightness temperature. The comparison with the operational products MODIS cloud mask has demonstrated the good performance of the cloud mask for the most of the cases analysed and has suggested some improvements to detects low clouds especially during the daytime. Remarking upon the results of comparison some disagreements are due to the differences between polar-orbiter and geostationary data.

In addition to cloud mask others parameters at high resolution are retrieved by using SEVIRI: cloud optical thickness and cloud particle effective radius. The retrieval is based on look-up tables obtained by radiative transfer simulations carried on by means of SBDART code. The SEVIRI cloud parameters at high resolution have allowed the analysis following meteorological events at different stages of lifetime. The temporal development of two convective systems has been followed using cloud optical thickness, effective radius and cloud top temperature. For the first system the development of two separate cells have been analysed: the increase of optical thickness and the cooling of the cloudy area typically occurs at early stage when the updraft columns reach the tropopause, then a warmer and thinner area grows. During the development the increment of the area with effective radius $> 14\mu m$ suggests a probability precipitation at the ground. The second convective system analysed is a cluster of cells that develop with different life span, despite of this a trend of the development of the cluster is identified.

The analysis of wide scale cloud systems at synoptic/sub-synoptic scale involved in climatological studies has been carried out by using cloud parameter at lower resolution derived by ISCCP database. The main characteristics of the cloud covers associated to Cut-off Low systems detected from 1992 to 2001 during the warm seasons in European/Mediterranean areas have been described. The analysis based on the vertical structure demonstrates that the most of shallow COLs have a cloud cover associated to them less than $10^5 km^2$. Moreover, they are affected by the strong NAO index in negative phase when they occur in Atlantic area while by the strong NAO index in positive phase when occur in Mediterranean area. Besides, most of cloud cover associated deep COLs have a wide ($> 10^6 km^2$) size and the NAO index affects the presence of these COLs with the opposite behaviour than shallow ones. The NAO index also affect the cloud cover associated to COLs in according to the results for the vertical structure and cloud cover associated to them. The cloud top temperature and optical thickness analysis reveals that the most cooler ($< 220K$) and thicker clouds (> 23) are detected at North-East respect to the centre of the COL.

The tools for cloud observation introduced by this work can play an active part in the validation and evaluation of clouds in numerical models at all scales and as input in models for geophysical parameters that works in cloud free conditions (such as aerosols). In addition the description of cloudy systems as cyclones can give a contribution to cloud climatology analysis.

Acronyms list

AIRS	Atmospheric InfraRed Sounder
ADEOS	Advanced Earth Observing Satellite
AMSU	Advanced Microwave Sounding Unit
AMSR-E	Advanced Microwave Scanning Radiometer - Earth Observing System
AVHRR	Advanced Very High Resolution Radiometer
CNA	China Meteorological Administration
CNES	Centre National d'Etudes Spatiales
COL	Cut-Off Low
CPR	Cloud Profiling Radar
CRF	Ccloud Radiative Forcing
DISORT	DIScrete ORdinate Radiative Transfer
e.m.	electromagnetic
EOS	Earth Observing System
ERBE	Earth Radiation Budget Experiment

EUMETSAT	European Organization for the Exploitation of Meteorological Satellites
ESA	European Spacial Agency
FOV	Field Of View
FY	FengYun
GEO	Geostationary Earth Orbit
GOES	Geostationary Operational Environmental Satellite
HIRS	High-Resolution Infrared Sounder
IASI	Infrared Atmospheric Sounding Interferometer
ISCCP	International Satellite Cloud Climatology Project
INSAT	Indian National SATellite system
IR	InfraRed
ISRO	Indian Space Research Organisation
IVSSR	Improved multispectral visible and infrared scan radiometer
JMA	Japan Meteorological Agency
KF	Kain-Fritsch
LEO	Low Earth Orbit
LOWTRAN	LOW-resolution atmospheric TRANsmition models
LTE	Local Thermodymamic Equilibrium
LWC	Liquid Water Content

MCS	Mesoscale Convective Systems
MERIS	Medium-spectral Resolution Imaging Spectrometer
MetOp-X	MetOp Satellite Series
MISR	Multi-angle Imaging SpectroRadiometer
MODIS	MODerate resolution Imaging Spectroradiometer
MSG	Meteosat Second Generation:
MTSAT	Multi-functional Transport Satellite
MW	MicroWave
NASA	National Aeronautics and Space Administration
NAO	North Atlantic Oscillation
NCAR	National Center for Atmospheric Research
NCEP	National Centers for Environmental Prediction
NIR	Near InfraRed
NOAA	National Oceanographic and Atmospheric Administration
NXX	NOOA Satellite Series
NWP	Numerical Weather Prediction
POLDER	Polarization and Directionality of the Earth's Reflectances
POES	Polar-orbiting Operational Environmental Satellite
PV	Potential Vorticity
RTE	Radiative Transfere Equation

SBDART	Santa Barbara DISORT Atmospheric Radiative Transfer
SEVIRI	Spinning Enhanced Visible and Infrared Imager
VAS	VISSR(Visible and Infrared Spin Scan Radiometer) Atmospheric Sounder
VHRSR	Very High Resolution Scanning Radiometer
VHRR	Very High Resolution Radiometer
VIRR	Visible and InfraRed Radiometer
VIS	VISible
WMO	Word Meteorological Organization

Bibliography

S.A. Ackerman and S.K. Cox. Comparison of satellite and all-sky camera estimates of cloud cover during GATE. *J.App.Met.*, 103:141–157, 1998.

S.A. Ackerman, K.I. Strabala, W.P. Menzel, R.A. Frey, and C.C. Moeller. Discriminating clear sky from clouds with MODIS. *J. Geophys. Res.*, 20: 581–587, 1998.

R.F. Adler, H.-Y.M. Yeh, N. Prasad, W.-K. Tao, and J. Simpson. Microwave simulations of tropical rainfall system with three-dimentional cloud model. *J. Appl. Meteor.*, 30:924–953, 1991.

P. Albert, R. Bennartz, and J. Fisher. Remote sensing of atmospheric water vapor from backscattered sunlight in cloudy atmospheres. *J. Atm. Ocean. Tech.*, 18:865–874, 2001.

A Arakawa. Modelling clouds and cloud processes for use in climate model. The physical basis of climate and climate modelling, GARP. *WMO Publication Series*, 16:183–197, 1975.

A. Arakawa. Rewiev article: The cumulus parameterization problem: Past, present, and future. *J. Clim.*, 17(13):2493–2525, 2004.

A. Arakawa and W.H. Schubert. Interaction of a cumulus clouds ensemble with the large-scale environment, part I. *J. Atmos. Sci*, 31:674–701, 1974.

Bibliography

A. Arking. Latitudinal distribution of cloud cover from TIROS III photographs. *Science*, 143:569–572, 1964.

A. Arking and J. D. Childs. Retrieval of cloud cover parameters from multispectral satellite images. *J. Climate Appl. Meteor*, 24:322–333, 1985.

B. Atlas. *Radar In Meteorology*. Lancaster Press, Lancaster, PA, 1990.

R. L. Bankert. Cloud classification of AVHRR imagery in maritime regions using a probabilistic neural network. *J. Appl. Meteor.*, 33:909–918, 1994.

G. Barnston and R. E. Livezey. Classification, seasonality and low-frequency atmospheric circulation patterns. *Mon. Wea. Rev.*, 115:1083–1126, 1987.

E.C. Barrett and D.W. Martin. *The Use of Satellite Data in Rainfall Monitoring*. Number 340 pp. Academic Press, London edition, 1981.

B. Baum, V. Tovinkere, J. Titlow, and R. M. Welch. Automated cloud classification of global AVHRR data using a fuzzy logic approach. *J. Appl. Meteor.*, 36:1519–1540, 1997.

S. Bony, Y. Sud, K. M. Lau, J. Susskind, and S. Saha. Comparison and satellite assessment of NASA/DAO and NCEPNCAR reanalyses over tropical ocean: Atmospheric hydrology and radiation. *J. Clim.*, 10:1441–1462, 1997.

F.-M. Breon and Colzy S. Cloud detection from the spaceborne POLDER instrument and validation against surface synoptic observations. *J. Appl. Meteor.*, 38:777–785, 1998.

K. A. Browing. A family outbreak of severe local storms. A comprehensive study of the storms in Oklahoma on 26 May 1963, part I. *Special Rept. AFCRL 65*, 695(23):346, 1965.

P. R. Brown, A. J. Illingworth, A. J. Heymsfield, G. M. McFarquhar, K. A. Browning, and M. Gosset. The role of spaceborne millimeter-wave radar in the global monitoring of ice cloud. *J. Appl. Meteor.*, 34:2346–2366, 1995.

K. A. Browning and F. F. Hill. Structure and evolution of mesoscale convective system near the British Isles. *Quart. J. Roy. Meteor. Soc.*, 110: 897–913, 1984.

J.C. Buriez and Coauthors. Cloud detection and derivation of cloud properties from POLDER. *Int. J. Remote Sens.*, 18:2785–2813, 1997.

D. Capacci, A. Battaglia, S. Mantovani, F. Porcú, B. Conway, and F. Prodi. On the sensitivity of modis visible/1.6 micron channels to radar-measured ground precipita- tion. *Proc of 14th International Conference on Clouds and Precipitation*, pages 1048–1051, 2004.

G. Cappelluti, Morea A., Notarnicola C., and Posa F. Automatic detection of local cloud systems from MODIS data. *J. Appl. Meteor. Clim.*, 45 issu 8:1056–1072, 2005.

M. Celano. *Cloud microphysical characterisation using polarimetric radar and satellite data.* PhD thesis, University of Ferrara, 2007.

F.L. Chang and Z. Li. Estimating the vertical variation of cloud droplet effective radius using multispectral near-infrared satellite measurements. *J. Geophys. Res.*, 107:no D15,4257, 2002.

C.-T. Chen and E. Roeckner. The characteristics of cloud fields associated with midlatitude circulation systems in a general circulation model. *Mon. Wea. Rev*, 130:570–589, 2002.

T. Chen, B. R. Rossow, and Y. Zhang. Radiative effects of cloud-type variations. *J. Climate*, 13:264–286, 1999.

E. E. Clothiaux, M.A. Miller, B.A. Albrecht, T.P. Ackerman, J. Verlinde, D.M. Babb, R.M. Peters, and W.J. Syrett. An evaluation of a 94-GHz radar for remote sensing of cloud properties. *J. Atmos. Oceanic. Technol*, 12:201–229, 1995.

R. J. Curran and M. L. C. Wu. Skylab near-infrared observations of clouds indicating supercooled liquid water droplets. *J. Atmos. Sci.*, 39:635–647, 1982.

A. Dahalback and Stamnes. A new spherical model for computing the radiation field available for photolysis and heating at twilight. *Planet. Space Sci.*, 39:671–683, 1991.

A. Dalla Libera. Elaborazione di dati da satellite per una climatologia delle nubi alla piccola scala. Master's thesis, University of Ferrara, 2002.

G. Delagado, A. Reda no, J. Lorente, R. Nieto, L. Gimeno, P. Ribera, D. Barriopedro, R. Garcìa-Herrera, and A. Serrano. Cloud cover analysis associated to cut-off low-pressure systems over Europe using Meteosat imagery. *Meteorol. Atmos. Phys.*, (96):141–157, 2006.

M. Demirtas and A.J. Thorpe. Sensitivity of short-range weather forecasts to local potential vorticity modifications. *Mon. Wea. Rev*, 129:922–939, 1999.

M. Derrien and H. Le Gleau. MSG/SEVIRI cloud mask and type from SAFNWC. *Int. J. Rem. Sens.*, 26:47074732, 2005.

M. Desbois, G. Seze, and G.Szejwach. Automatic classification of clouds on METEOSAT imagery: Application to high-level cloud. *J. Appl. Meteor.*, 21:401412, 1982.

P.-Y. Deschamps, F.-M. Breon ., M. Leroy, A. Podaire, A. Bricaud, J.-C. Buriez, and Seze G. The POLDER mission: instrument characteristics and scientific objectives. *IEEE Trans. Geosci. Remote Sens.*, 32,issue3: 598–615, 1994.

D.J. Diner, J.C. Beckert, T.H. Reilly, C.J. Bruegge, J.E. Conel, R. Kahn, J.V. Martonchik, T.P. Ackerman, R. Davies, S.A.W. Gerstl, H.R. Gordon, J-P. Muller, R. Myneni, R.J. Sellers, B. Pinty, and M.M. Verstraete. Multi-angle Imaging SpectroRadiometer (MISR) description and experiment overview. *IEEE Trans. Geosci. Rem. Sens.*, 36(4):1072–1087, 1998.

R. J. Doviak and D. S. Zrnic. *Doppler Radar and Weather Observations.* Academic Press, San Diego, Calif., 1993.

D. C. Dowell, F. Zhang, L. J. Wicker, C. Snyder, and N. A. Crook. Wind and temperature retrievals in the 17 May supercell: Ensemble Kalman filter experiments. 1981 Arcadia, Oklahoma. *Mon. Wea. Rev.*, 132:1982–2005, 2004.

P. A. Durkee. Observations of aerosol-cloud interactions in satellite detected visible and near-infrared radiance. *Proc. Symp.on the Role of Clouds in Atmospheric Chemistry and Global Climate, Amer. Meteor. Soc., Anaheim*, pages 157–160, 1989.

E Ebert. A pattern recognition technique for distinguishing surface and cloud types in the polar regions. *J. Clim. Appl. Meteorol.*, 26:14121427, 1987.

K. A. Emanuel. A scheme for representing cumulus convection in large-scale models. *J. Atmos. Sci.*, 48:2313–2335, 1991.

EUMETSAT. Cloud detection for MSG - algorithm theoretical basis document. Technical Report Doc.No.:EUM/MET/REP/07/0132, EUMETSAT, 2007.

N. I. Fox and A. J. Illingworth. The retrieval of stratocumulus cloud properties by ground-based cloud radar. *J. Appl. Meteorol*, 36(5):485–492, 1997.

L. Garand. Automated recognition of oceanic cloud patterns. part I: Methodology and application to cloud climatology. *J. Clim.*, 1:2039, 1987.

R. García-Herrera, D. G. Puyol, E. H. Martín, L. G. Presa, and P. R. Rodrígue. Influence of the North Atlantic Oscillation on the Canary Islands precipitation. *J. Climate*, 14:38893903, 2001.

C.G. Georgiev. Quantitative relationship between meteosat WV data and positive potential vorticity anomalies: a case study over the mediterranean. *Meteorol. Appl.*, 6:97–109, 1999.

P. J. Gleckler and Coauthors. Cloud-radiative effects on implied oceanic energy transports as simulated by atmospheric general circulation models. *Geophys. Res. Lett.*, 22:791794, 1995.

J. E. Hansen and J. B. Pollack. Near-infrared light scattering by terrestrial clouds. *J. Atmos. Sci.*, 21:265–281, 1970.

J. E. Hansen and L. D. Travis. Light scattering in planetary atmospheres. *Space Sci. Rev*, 16:527–610, 1974.

E.F. Harrison, R. Barkstrom, V. Ramanathan, R.D. Cess, and G. Gibson. Seasonal variation of cloud radiative forcing derived from Earth Radiation Budget Experiment. *J. Geophys. Res.*, 95:18687–18703, 1990.

D.L. Hartmann. *Global Physical Climatology.* Accademic Press, 1994.

D.L. Hartmann and D. Doelling. On the net radiative effectiveness of clouds. *J. Geophys. Res.*, 96:869–891, 1991.

A Henderson-Sellers. Continental cloudiness changes this century. *J. Geophys. Res.*, 273:255–262, 1992.

A. Henderson-Sellers, G. Sèze, F. Drake, and M. Desbois. Surface-observed and satellite-retrieved cloudiness compared for the 1983 ISCCP special study area in Europe. *J. Geophys. Res.*, 92:4019–4033, 1987.

G.M. Heymsfield and R.H. Blackmer. Satellite-observed characteristics of Midwest severe thunderstorm anvils. *Mon. Wea. Rev*, 116:2200–2224, 1988.

J.R Holton. *An Introduction to Dynamic Meterology*, volume 23. International Geophysics Series, second edition, 1983.

B. J. Hoskins, M. E. Mcintyre, and A. L. W. Robertson. On the use and significance of isentropic potential vorticity maps. *Quart. J. R. Meteor. Soc.*, 111:877–946, 1985.

J. R. A. Houze, James C. N., and Medina S. Radar observations of precipitation and airflow on the Mediterranean side of the Alps: Autumn 1998 and 1999. *Q. J. R. Meteorol. Soc.*, 127:25372558, 2001.

J.W. Hurrel. Decadal trends in the North Atlantic Oscillation: Regional temperatures and precipitation. *Science*, 269:676–679, 1995.

Y. Jin, W.B. Rossow, and D.P. Wylie. Comparison of the climatologies of high-level clouds from HIRS and ISCCP. *Journal of Climate*, 9 Issue 11: 2850–2879, 1996.

J.S. Kain and J.M. Fritsch. Convective parameterization for mesoscale models: The Kain-Fritsch scheme. the representation of cumulus convection in numerical models. *Amer. Meteor. Soc.*, 24:165–170, 1993.

D. P. Kaiser. Decreasing cloudiness over China: An updated analysis examining additional variables. *Geophys. Res. Lett.*, 27:2193–2196, 2000.

D. P. Kaiser. Analysis of total cloud amount over China. *Geophys. Res. Lett.*, 25:3599–3602, 1998.

T. R. Karl, P. D. Knight, G. Kukla, N. Plummer, V. Razuvayev, K. P. Gallo, J. Lindseay, R.J. Charlson, and T.C. Peterson. A new perspective on recent global warming: Asymmetric trends of daily maximum and minimum temperature. *Bull. Am. Met. Soc.*, 74:1007–1023, 1993.

T.R. Karl and P. M. Streurer. Increased cloudness in the United States during the first half of this century: fact or fiction? *Geophys. Res. Lett.*, 25:3599–3602, 1998.

K.-G. Karlsson. Development of an operational cloud classification model. *Int. J. Remote. Sensing*, 10:687–693, 1989.

A.S Kentarchos and T.D. Davies. A climatology of cut-off lows at 200 hPa in the Northern Hemisphere, 1990-1994. *Int. J. Climatol.*, 18:379–390, 1998.

S. Q. Kidder and T.H. Vonder-Haar. *Satellite Meteorology an introduction.* Accademic Press, 1995.

S.Q. Kidder and H.-T.Wu. Dramatic contrast beween low clouds and snow cover in daytime 3.7 μm imagery. *Mon. Wea. Rev.*, 112:2345–2346, 1984.

M. D King. Determination of the scaled optical thickness of clouds from reflected solar radiation measurements. *J. Atmos. Sci*, 44:1734–1751, 1987.

M. D. King, S.-C. Tsay, S. E. Platnick, M. Wang, and K.-N. Liou. Cloud retrieval algorithms for MODIS: Optical thickness, effective particle radius, and thermodynamic phase. *MODIS Algorithm Theoretical Basis Document*, (ATBD-MOD-05 MOD06):79 pp, 1997.

P Knippertz and J.E. Martin. The role of dynamic and diabati processes in the generation of cut-off lows over Northwest Africa. *Meteor. Atmos. Phys.*, 96(1-2):4–19, 2007.

V. Kotroni, K. Lagouvardos, E. Defer, S. Dietrich, F. Porcú, and C.M. Medaglia amd M. Demirtas. The Antalya 5 December 2002 storm: observations and model analysis. *J. Appl. Meteor. Clim.*, 45:576–590, 2006.

M. Kurz. *Synoptic Meteorology.* Deutscher Wetterdienst, second, completely revised edition edition, 1988.

N.C. Lau and W.C. Crane. A satellite view of the synoptic-scale organization of cloud properties in midlatitude and tropical circulation systems. *Mon. Wea. Rev.*, 123:1984–2006, 1994.

V. Levizzani. Satellite rainfall estimations: new perspectives for meteorology and climate from the EURAINSAT project. *Annals of Geophysics*, 46:363–372, 2003.

R.M. Lhermitte. Cloud and precipitation remote sensing at 94 GHz. *Geoscience and remote sensing*, 26:207–216, 1988.

K. N. Liou. *An introduction to atmospheric radiation*, volume 84 of *International geophysics series.* Academic Press, second edition, 2002.

R. A. Maddox. Mesoscale convective complexes. *Bull. Amer. Meteor. Soc.*, 61:1374–1387, 1980.

J. Marshall, Y. Kushnir, D. Battisti, P. Chang, A. Czaja, R. Dickson, J. Hurrell, M. McCartney, R. Saravanan, and M. Visbeck. North Atlantic climate variability: phenomena, impacts and mechanisms. *Int. J. Climatol.*, 21: 18631898, 2001.

J. D. Marwitz. The structure and motion of severe hailstorms. Part I: supercell storms. *J. Appl. Meteor.*, 11:166–179, 1972.

P. Menzel and K. Strabala. MODIS: Cloud top properties and cloud phase. *MODIS Algorithm Theoretical Basis Document ATBD-04*, page 55 pp, 1997.

P. W Menzel. Cloud tracking with satellite imagery: From the pioneering work of Ted Fujita to the present. *Bull. Amer. Meteor. Soc.*, 82:3347, 2001.

W. P. Menzel. Remote sensing applications with meteorological satellites. NOAA Satellite and Information Service, University of Wisconsin Madison, WI, February 2006.

C. J. Merchant, A. R. Harris, E. Maturi, and S. Maccallum. Probabilistically physically based cloud operational sea surface temperature retrieval. *Q. J. R. Meteor. Soc.*, 131:27352755, 2005.

K.I. Mohr, J.S. Famiglietti, and E.J. Zipser. The contribution to tropical rainfall with respect to convective system type, size, and intensity estimated from the 85-GHz ice-scattering signature. *J. Appl. Meteor.*, 38: 596–606, 1998.

C. Morel and S. Senesi. A climatology of mesoscale convective systems over Europe using satellite infrared imagery. part I: Methodology. *Q. J. R. Meteorol. Soc.*, 128:1953–1971, 2002.

C. Moroney, R. Davies, and J.-P. Muller. Operational retrieval of cloud-top heights using MISR data. *IEEE Trans. Geosci. Remote Sens.*, 40:1532–1540, 2002.

A. Mugnai and E. A. Smith. *Passive microwave radiation transfer in an evolving cloud medium.*, volume IRS'84 of *Current problems in atmospheric radiation.* A.Deepak, 1984.

A. Mugnai and E. A. Smith. Radiative transfer to space through a precipitating cloud at multiple microwave frequencies. part I: Model description. *J. Appl. Meteor.*, 27:1055–1073, 1988a.

A. Mugnai and E. A. Smith. Radiative transfer to space through a precipitating cloud at multiple microwave frequencies. part II: Results and analysis. *J. Appl. Meteor.*, 27:1074–1091, 1988b.

T. Nakajima and M.D. King. Determination of the optical thickness and effective particle radius of clouds from reflected solar radiation measurements, part I: Theory. *J. of Atm. Sci.*, 47:1878–1893, 1990.

T. Y. Nakajima and T. Nakajima. Wide-area determination of cloud microphysical properties from NOAA AVHRR measurements for FIRE and ASTEX regions. *J. Atmos. Sci.*, 52:4043–4059, 1995.

A. J. Negri. Cloud-top structure of tornado storms on 10 April 1979 from rapid scan and stereo satellite observations. *Bull. Am. Met. Soc.*, 63(10): 1151–1859, 1982.

R. Nieto, L. Gimeno, L. De la Torre, P. Ribera, D. Gallego, R. Garcìa-Herrera, J.A. Garcìa, M. Nunez, A. Redano, and J.Lorente. Climatology features of cut-off low systems in the Northern Hemisphere. *J. Climate*, 18(16):3085–3103, 2005.

R. Nieto, L. Gimeno, L. De la Torre, P.Ribera, R. Barropedro, A. Serrano, A. Gordillo, R. Garcìa-Herrera, A. Redano, and J.Lorente. Interannual variability of cut off low systems over the European sector: The role of blocking and Northern Hemisphere circulation modes. *Meteorol. Atmos. Phys.*, 96:121140, 2007.

E. Palmén and C.W. Newton. *Atmospheric circulation systems: Their structure and physical interpretation.* Academic Press, 1969.

Meischner P.F., V.N. Bringi, D. Heimann, and H. Höller. A squall line in Southern Germany: Kinematics and precipitation formation as deduced by advanced polarimetric and doppler radar measurements. *Mon. Wea. Rev*, 119:678–701, 1991.

J.H Pierluissi and G.-S. Peng. New molecular transission band models for LOWTRAN. *Opt. Eng.*, 24(3):541–547, 1985.

J.G. Pinto, S. Zacharias, A.H. Fink, G.C. Leckebusch, and U. Ulbrich. Factors contributing to the development of extreme North Atlantic cyclones and their relationship with NAO. *Clim. Dyn.*, 32:711–737, 2008.

S. Platnick and S. Twomey. Determining the susceptibility of cloud albedo to changes in droplet concentrations with the Advanced Very High Resolution Radiometer. *J. Appl. Meteorol.*, 33:334–347, 1994.

S. Platnick and F. P. J. Valero. A validation study of a satellite cloud retrieval during ASTEX. *J. Atmos. Sci.*, 52:2985–3001, 1995.

S. Platnick, M. D. King, S. A. Ackerman, W. P. Menzel, B. A. Baum, J. C. Riédi, and R.A. Frey. The MODIS cloud products: Algorithms and examples from Terra, IEEE. *Trans. Geosci. Remote Sens.*, 41:459–473, 2003.

F. Porcú and V. Levizzani. Cloud classification using METEOSAT VIS-IR imagery. *J. Rem. Sens.*, 13:893–909, 1992.

F. Porcú, C. Caracciolo, and F. Prodi. Cloud systems leading to flood events in Europe: an overview and classification. *Met. Appl.*, 10:217–228, 2003.

F. Porcú, A. Carrassi, C.M. Medaglia, A. Mugnai, and F. Prodi. A study on cut-off low vertical structure and precipitation in the Mediterranean region. *Meteorol. Atmos. Phys.*, 96:121–140, 2007.

J.D. Price and G. Vaughan. Statistical studies of cut-off low systems. *Ann. Geophys.*, 10:96–102, 1992.

F. Prodi. Combined photo and radar observations of storms in the Po Valley. *Riv. It. di Geofisica*, XXIII:82–88, 1974.

F. Prodi and E. Wirth. Mesoscale and microphysical investigation of an isolated hailstorm. *Riv. It. di Geofisica*, XXII:165–185, 1973.

H.R. Pruppacher and J.D. Klett. *Microphysics of Clouds and Precipitation.* Kluver Academic, Dordrecht edition, 1997.

J. Pudykiewicz, R. Benoit, and J. Mailhot. Inclusion and verification of a predictive cloud-water scheme in a regional numerical weather prediction model. *Mon. Wea. Rev.*, 120:612–626, 1991.

J. F. W. Purdom. *Subjective Interpretation of Geostationary Satellite Data for Nowcasting*, volume Nowcasting of *149-166.* Academic Press, 1982.

V. Ramanathan, R. D. Cess, E. F. Harrison, B. R. Barkstrom P. Minnis, E. Ahmad, and D. Hartmann. Cloud-radiative forcing and climate:results from the Earth Radiation Budget Experiment. *Science*, 243:57–63, 1989.

W. R. Reynolds and T. M. Smith. Improved global sea surface temperature analyses using optimum interpolation. *J. Climate*, 7:929–948, 1994.

P. Ricchiazzi and C. Guatier. Investigation of the effect of surface heterogeneity and topography on the radiation environment of Palmer Station, Antartica, with a hybrid 3D radiative transfer model. *J. Geophys. Res.*, 103:6161–6176, 1998.

E. Ricciardelli, F. Romano, and V. Cuomo. Physical and statistical approaches for cloud identification using Meteosat Second Generation-Spinning Enhanced Visible and Infrared imager data. *Remote Sensing of Environment*, 112:2741–2760, 2008.

N. Roberto, M. Celano, D. Capacci, F. Porc, P.P. Alberoni, and F. Prodi. Using SEVIRI derived cloud microphysical proprieties to infer cloud structure and ground precipitation. In *Proceeding of EUMETSAT Meteorological Satellite Conference Helsinki*, 2006.

R. R. Rogers. *A Short Course in Cloud Physics*. Number 227 pp. Pergamon, 1977.

D. Rosenfeld and G. Gutman. Retrieving microphysical proprieties near the tops of potential rain clouds by multispectral analysis of AVHRR data. *J. Atmos. Res.*, 34:259–283, 1994.

D. Rosenfeld and I.M. Lensky. Satellite-based insights into precipitation formation processes in continental and maritime convective clouds. *Bull. Am. Meteor. Soc.*, 79:2457–2476, 1998.

W. B. Rossow and B. Cairns. Monitoring changes of clouds. *Climatic Change*, 31:305347, 1995.

W. B. Rossow and L.C. Garder. Cloud detection using satellite measurements of infrared and visible radiances for ISCCP. *J. Climate*, 6:2341–2369, 1993.

W. B. Rossow and R. A. Shiffer. ISCCP cloud data products. *Bull. Am. Meteorol. Soc.*, 71:2–220, 1991.

W. B. Rossow and R. A. Shiffer. Advances in understanding clouds from ISCCP. *Bull. Am. Meteorol. Soc.*, 80:2261–2288, 1999.

R. W. Saunders and K. T. Kriebel. An improved method for detecting clear sky and cloudy radiances from AVHRR data. *Int. J. Rem. Sens.*, 9:123150, 1987.

R. A. Schiffer and W. B. Rossow. The international satellite cloud climatology project (ISCCP). the first project of the World Climate Research Programme. *Amer. Meteor. Soc. Bull*, 64:779–784., 1983.

M. Schroder, R. Bennartz, L. Schullerand R. Preusker, P. Albert, and J. Fischer. Generating cloudmasks in spatial high-resolution observations of clouds using texture and radiance information. *Int. J. Rem. Sens.*, 23: 42474261, 2002.

TRMM staff. Tropical Rainfall Measurements Mission 2007: Senior review proposal, 2007.

K Stamnes, S.-C. Tsay, W. Wiscombe, and K. Jayaweera. Numerically stable algorithm for discrete-ordinate-method radiative transfer in multiple scattering and emitting layered media. *Appl. Opt.*, 27:2502–2509, 1988.

G. L. Stephens and T. J. Greenwald. Observations of the earth's radiation budget in relation to atmospheric hydrology. Part I: Clear sky greenhouse effect and water vapor feedback. *J. Geophys. Res.*, 96(15):311–324, 1991.

G.L. Stephens. *Remote sensing of lower atmosphere. An introduction.* Oxford University Press, 1994.

G.L. Stephens, D.G. Vane, R.J. Boain, G.G. Mace, K. Sassen, Z. Wang, A.J. Illingworth, E.J. Oconnor, W.B. Rossow, S.L. Durden, S.D. Miller, R.T. Austin, A. Benedetti, C. Mitrescu, and The Cloudsat Science Team. The CloudSat mission and the A-Train: a new dimension of space observations of clouds and precipitation. *Bull. Amer. Meteor. Soc.*, 83:1771–1790, 2002.

K. I. Strabala, S. A. Ackerman, and W. P. Menzel. Cloud properties inferred from 8-12 micron data. *J. Appl. Meteor.*, 33(2):212–229, 1994.

A.N. Straniforth and J. Mailhot. An operational model for regional weather forecasting. *Comput. Math. Applic.*, 16(1/2):1–22, 1988.

B. Sun and P. Y. Groisman. Cloudiness variations over the former Soviet-Union. *Int. J. Climatol.*, 20:1097–1111, 2000.

H. Sundquist. Atmospheric condensation and modelling its non-convective regime. *ECMWF-Seminar Proc.*, pages 91–159, 1977.

H. Sundquist and M.E Schlesinger. Parameterization of condensation and associated clouds in models for weather prediction and general circulation simulation. *Physically-based Modelling and Simulation of Climate and Climatic Change*, pages 433–461, 1988.

I. Trigo, T. D.Davies, and G. R. Bigg. Objective climatology of cyclones in the Mediterranean region. *J. Climate*, 12:1685169, 1999.

G.J. Tripoli, C.M. Medaglia, S.M. Dietrich, A. Mugnai, G. Panegrossi, S. Pinor E., and A. Smith. The 9-10 November 2001 Algerian flood: a numerical study. *Bull. Amer. Meteo. Soc.*, 86:1229–1235, 2005.

S. Uppala, P. K'allberg, A. Hernandez, S. Saarinen, M. Fiorino, X. Liand K. Onogi, K. Sokka, U. Andrae, and V. Da Costa Bechtold. ERA-40: ECMWF 45-year reanalysis of the global atmosphere and surface conditions 19572002. *ECMWF Newsletter*, 101:221, 2004.

P. K. Wang. The thermodynamic structure atop a penetrating convective thunderstorm. *Atm. Res.*, 83:254–262, 2007.

J. A. Wienman and Harshvardhan. Solar reflection from regular array of horizontally finite clouds. *App. Optics*, 21:2940–2944, 1982.

E. L. A Wolters, A. R. Robert, and A. J. Feijt. Evaluation of cloud-phase retrieval methods for SEVIRI on METEOSAT-8 using ground-based lidar and cloud radar data. *J. Appl. Met. Clim.*, 47:1723–1728, 2007.

J. Wurman and S. Gill. Finescale radar observations of the Dimmitt, Texas (2 June 1995), tornado. *Mon. Wea. Rev*, 128:2135–2164, 2000.

D.P. Wylie and W.P. Menzel. Eight years of high cloud statistics using HIRS. *J. Climate*, 12:170–184, 1999.

D.P. Wylie, W.P. Menzel, H.M. Woolf, and K.I. Strabala. Four years of global cirrus cloud statistics using HIRS. *J. of Climate*, 7:1972–1986, 1994.

T. Yamanouchi, K. Suzuki, and S. Kawaguchi. Detection of clouds in antarctica from infrared multispectral data of AVHRR. *J. Meteor. Soc. Japan*, 65:949962, 1987.

Acknowledgement

Special thanks go to my referees Professor Kostas Lagouvardos and Professor Francesco Posa for their precious suggestions and corrections to my PhD work.
Un ringraziamento particolare va al mio tutore Dott. Federico Porcú il quale con tanta pazienza, estrema competenza e disponibilitá mi ha indirizzato nel lavoro seguendomi con attenzione e partecipazione durante questi anni di lavoro e di studio. Vorrei inoltre ringraziare il Prof. Franco Prodi che durante tutto il percorso di studi mi ha elargito tramite i suoi consigli tutta la sua esperienza e professionalitá.
Un caloroso ringraziamento va all'Universitá di Ferrara e al Coordinatore del Corso di Dottorato in Fisica per avermi dato l'opportunitá di compiere questo percorso di studi fornendomi tutti gli strumenti necessari per raggiungere questo traguardo.
Un grazie di cuore a tutti i miei colleghi dell'Universitá con i quali nel corso di questi anni ho condiviso lavoro e amicizia, in particolare alle mie fedelissime amiche Melissa e Francesca e al mio mentore giá papá Davide Capacci. Inoltre grazie a tutti i miei amici (per l'elenco rimando alla mia cartella amici di Facebook) che mi hanno allietato le serate e le giornate, in particolare devo ringraziare Micol, Tatiana, Claudia, Leila e Leo.
Se non ci fossero stati loro sicuramente ora non mi troverei qui, per cui un grazie di cuore ai miei genitori che mi hanno sostenuto e incoraggiato sempre e ai miei fratelli (Amedeo, Giancarlo e Paolo) e a mia sorella (Marianna) che

mi hanno sopportato anche nelle giornate piú nere.
Infine, ma non per importanza, un grazie immenso va a Marco per avermi incoraggiata a pensare sempre positivo, per avermi sopportata e “accudita” in questi ultimi mesi e ti ringrazio per ogni giorno che mi sei stato e mi sarai accanto.